BACTERIOPHAGE IMAGING IMMUNOASSAY FOR POINT OF CARE DIAGNOSTICS

A Dissertation

Presented to

the Faculty of the Department of Chemical & Biomolecular Engineering

University of Houston

In Partial Fulfillment

of the Requirements for the Degree

Doctor of Philosophy

in Chemical Engineering

by

Jinsu Kim

August 2016

BACTERIOPHAGE IMAGING IMMUNOASSAY FOR POINT OF CARE

DIAGNOSTICS

_____

Jinsu Kim

Approved:

_____

Chair of the Committee
Jacinta C. Conrad, Assistant Professor,
Chemical & Biomolecular Engineering

_____

Co-chair of the Committee
Richard C. Willson, Professor,
Chemical & Biomolecular Engineering

Committee Members:

_____

Peter Vekilov, Professor,
Chemical & Biomolecular Engineering

_____

Navin Varadarajan, Assistant Professor,
Chemical & Biomolecular Engineering

_____

Wei-Chuan Shih, Associate Professor,
Electrical & Computer Engineering

_____

Hadi Ghasemi, Assistant Professor,
Mechanical Engineering

_____

Suresh K. Khator, Associate Dean,
Cullen College of Engineering

_____

Michael P. Harold, Professor and Chair,
Chemical & Biomolecular Engineering

Acknowledgements

I would like to express my deepest gratitude to my supervisor Prof. Dr. Jacinta C. Conrad, for her valuable instructions and support throughout my graduate life. The knowledge and experience I learned from her have built up solid backgrounds towards my future works. I would like to thank her for always being readily available for instructive discussions and funding to make my PhD experience productive and stimulating.

I want to thank Prof. Dr. Richard C. Willson as my PhD co-advisor who provided me incredible help and advice on the biomolecular diagnostics and sensors. I hold his valuable advice, his scientific guidance, and the inspiring discussions in high regard. Also, many thanks for the pleasant working atmosphere in the group.

I am thankful for the generous device support of the sCMOS camera which Dr. Peter Vekilov provided. I would like to thank Dr. Katerina Kourentzi for your introduction to various experimental skills during my projects. I also truly wish to thank Dr. Peter Vekilov, Dr. Navin Varadarajan, Dr. Wei-Chuan Shih and Dr. Hadi Ghasemi for serving on my committee and for their constructive comments and recommendations on my research projects.

I want to thank all my former colleagues in Willson's and Conrad's group for the outstanding working climate. Particularly, I want to mention Wen-Hsiang Chen, Meenu Adhikari , Anna Hagström , Sagar Dhamane, and Rahul Pandey. Thanks for your support, for your friendship, and for the good times we spent together.

Appreciation is given to my fellow lab mates and collaborators: Guozhen Yang, Ujwal Patil, Hui Chen, Binh Vu, João R. C. Trabuco, Maria J. C. Jacinto, Ahmad Nazem,

Gavin Garvey, Andrew Paterson, Vivek Yadav, Heather Goux, Mary Crum, and Andrea Jaimes for the nice time in our lab and for the outstanding assistance whenever I needed help.

Outside the university, special thanks go to Yang Li and Prof. Dr. Lee Jitae.

Finally, I am sincerely grateful to my family: my father, my mother, my brothers and all the other family members for their love, understanding, encouragement, and always supporting me throughout the past years.

BACTERIOPHAGE IMAGING IMMUNOASSAY FOR POINT OF CARE DIAGNOSTICS

An Abstract

of

A Dissertation

Presented to

the Faculty of the Department of Chemical & Biomolecular Engineering

University of Houston

In Partial Fulfillment

of the Requirements for the Degree

Doctor of Philosophy

in Chemical Engineering

by

Jinsu Kim

August 2016

Abstract

Point-of-care (PoC) devices are used for medical testing at or near the site of patient care. Due to its low cost, simple assay operation, and ease of mass production, the lateral flow immunoassay (LFA) is one of the most widely used and commercially available PoC tests. Nevertheless, traditional LFAs remain limited by two main issues: lack of sensitivity and difficulties in quantification. To develop sensitive and quantitative LFAs, we can consider three strategies (1) new LFA reaction membranes, (2) new reporter materials, and/or (3) new read-out methods.

Here, we developed functionalized phage nanoparticles as a new sensitive reporter for LFAs. The use of phage as a scaffold for attachment of multiple bio-recognition and read-out-signal molecules constitutes a novel and innovative approach in LFAs. We first developed fluorescently labeled M13 phage that also are functionalized with anti-analyte antibodies. Individual phage bound to the target analyte (here MS2 virus as a model) and captured on an LFA membrane strip were imaged using epi-fluorescence microscopy. Using automated image processing, we counted the number of bound phage in micrographs as a function of target concentration. The resultant assay was more sensitive than enzyme-linked immunosorbent assays and traditional colloidal-gold nanoparticle LFAs for direct detection of viruses.

Next, to understand the high sensitivity, we characterized the binding modes of the phage reporter to targets in the fibrous glass LFA membrane using microscopy and image analysis. We found that the elongated shape of M13 phage coupled with the complex flow promotes reorientation and facilitates the binding.

The binding efficiency was also influenced by other assay parameters, such as the length of the phage and their flux through the LFA membrane. The number of bound phage increased as the phage length increased; similarly the number of bound phage increased with the flux [within a particular flow regime]. These results suggested that the increased length and flux of phage increased the chance that phage encountered fibers, thereby enhancing binding efficiency.

Next, as a first step towards practical phage LFAs we characterized the stability and durability of phage at elevated temperatures. To reveal the mechanism of temperature-tolerant mutant stability, we characterized the mutant genomes using next-generation sequencing technology. Three potential mechanisms were suggested for the apparent increase in temperature tolerance: gene replication enhancement (due to mutations in gp2); formation of miniphage; and mutations in the p7 coat protein.

Finally, as a first step towards a user-friendly and handheld system compatible with PoC use, we incorporated two photon detectors, a multi-pixel photon counter (MPPC) and a photomultiplier tube (PMT), into a smartphone accessory. The sensitivities of those detectors were compared by determining a low level of 1,5-anhydroglucitol (AHG) as a model test reaction in a chemiluminescence assay. The assay sensitivity depended on the detector performance; the PMT detector exhibited ten-fold better sensitivity than the MPPC. These results raise the promising possibility that the developed detectors could be applied to our phage LFA by inserting the appropriate light source and optical filters.

Table of Contents

List of Figures

List of Tables

Chapter 1 Introduction

1.1 Lateral Flow Assays (LFAs) as Point of Care Diagnostics

Point-of-care (PoC) brings diagnostics closer to the patient for rapid and timely testing. PoC diagnostics have the enormous potential to dramatically speed up diagnosis, enabling quicker initiation of appropriate disease management and thus improving human health.[1] The benefits are maximized in emergencies and in areas with limited laboratory infrastructure, including on ships, at home, in a physician's offices, ambulances, fields, or in hospitals. The results of care provide the promise of improving outcomes with reducing costs through increased access to and use of diagnostic and self-monitoring solutions.[2, 3] As also outlined in the World Health Organization's *ASSURED* criteria, the ideal PoC testing should be: Affordable, Sensitive, Specific, User-friendly, Rapid and Robust, Equipment-free and Deliverable to end-users.[4]

Lateral flow assays (LFAs) are one of the dominant PoC diagnostics in the market holding a multi-billion dollar value over the last three decades; the pregnancy test for human chorionic gonadotropin is the model example.[5] LFAs provide prompt diagnostic results in short times for qualitative and semi-quantitative analysis without the need for elaborate sample preparation or capital investment. In conventional LFAs gold, dyed latex, or carbon nanoparticles bearing antibodies to the target are used as the reporter, which is analyte-bridged to a capture antibody immobilized onto the surface of a nitrocellulose strip. A line of captured reporter particles indicates a positive result, and a downstream control line demonstrates that the test has been performed correctly. The classic LFA is a brilliant approach to delivering immunoassays in a rapid and easy-to-use format. LFAs have been used to detect a wide range of biomolecules, including nucleic

acids, proteins, toxins, and hormones, as well as bacterial and viral pathogens.[6, 7, 8]

1.2 Principle of LFA

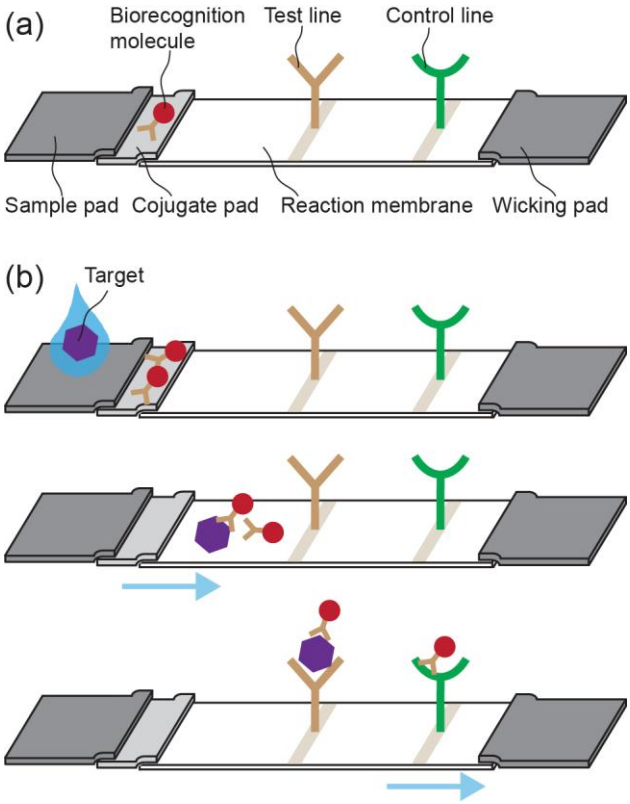

Figure 1.1 Lateral flow assay. (a) Structure of assay (b) Principle of assay

A typical lateral flow strip consists of four main components, including sample pad, conjugate pad, reaction membrane and wicking (or adsorbent) pad, as shown in Figure 1.1a. The sample pad is made of cellulose or glass fibers and it is where the sample is applied to start the assay. The sample pad is designed to hold an excess of sample fluid acting like a sponge, and to transport the sample smoothly and continuously. Once the sample is released from the sample pad, the fluid migrates to the conjugate pad which is made of glass fibers where biorecognition molecules bound on reporter molecules (usually gold nanoparticles or latex microspheres modified with antibodies specific to the analyte) are dispensed. On the conjugate pad, the analyte, if present on the

sample, will be linked to the biorecognition molecules on the reporter conjugates, and migrate further through the next capillary bed of the reaction membrane. The reaction membrane is made of nitrocellulose or glass fibers on which anti-target analyte antibodies are immobilized in a line that acts as a capture zone or test line. The control line is also present, containing antibodies specific for the conjugate antibodies. Further, the wicking pad draws the sample across the reaction membrane by capillary action, maintaining the flow rate and keeping the liquid from back flow. The schematic of the LFA principle is shown in Figure 1.1b.

1.3 Challenge of Traditional LFAs

Even though the classic LFA is an elegant approach to delivering immunoassays in a rapid and easy-to-use format, its limits of detection (LoD) lag behind more complex laboratory methods[9] used for proteins (e.g. ELISA) and viruses (e.g. plaque assays or PCR[10, 11]). For example, colloidal gold LFAs for Japanese encephalitis virus in swine are reported to detect 2.5×10^{6} pfu ml^{-1} and for filamentous *Escherichia coli* M13 phage was able to detect 5×10^{7} pfu ml^{-1}.[12, 13] Better LoDs might well expand the range of LFA applications, including pathogen monitoring in food and in biopharmaceutical manufacturing.[14, 15]

Striving to overcome the LoD limitations that currently limit the wider use of LFAs, one common strategy is to develop new reporters and/or readouts that enable quantitative measuring of the analyte concentration. Alternative reporters such as Eu-III nanoparticles[16] and up-converting phosphors[17] have shown improved limits of detection compared to gold nanoparticles, but require specialized instrumentation. Signal amplification strategies utilizing “carriers” loaded with reporters have been already

applied to immunoassays (e.g. ELISA[18, 19], immuno-PCR[20, 21], microarrays[22]) with significant success. In the arena of LFAs, gold nanoparticles loaded with antibodies and enzyme reporters were used to detect a model protein, human IgG; up to one order of magnitude increased sensitivity was observable by the naked eye.[23] A sensitive LFA has also been reported for cholera toxin[24], using ganglioside-incorporated liposomes bearing a visible red dye. Polylysine loaded with fluorophors and antibodies has also been reported[25] as a highly analytically-sensitive detection conjugate, albeit its fluorescent output requires a specialized reader.

1.4 Viral Nano-particles As New LFA Reporters

Despite the various research efforts, there still remains an unmet need of more-sensitive reporter technologies that can be adapted in LFA without compromising the LFA's attractive inherent features, such as ease of use and minimal equipment requirements. Functionalized nano-particles were reported to be suitable as affinity reagents in immunoassays[26, 27] and engineered viral nanoparticles are increasingly used as building blocks to generate sophisticated structures for diagnostics.[28] Bacteriophage (phage) nanoparticles present mono-disperse yet versatile scaffolds that exhibit high colloidal stability and storage stability. The use of phage as a scaffold for attachment of multiple bio-recognition and read-out-signal molecules constitutes a novel and innovative approach in lateral flow assays. The result will be a universal reporter that requires no phage display selection or antibody cloning, is easily adaptable to any system for which high affinity recognition elements exist, and eases the most serious limitation of LFAs: the lack of adequate analytical sensitivity for more widespread clinical utility, and thus will have an immediate impact in all areas of point-of-care analyte detection. We further

believe that these reporters can be easily integrated with the latest technical innovations, such as analyte pre-concentration/enrichment[13, 29 ,30] and paper microfluidics,[31] in an effort to build the most clinically-useful LFAs.

1.5 Objectives of Thesis

1. Develop Ultra-Sensitive Phage LFAs Using Novel Reporters and Readouts.

A novel reporter and readout format was developed for use in LFAs. M13 phage surfaces were genetically engineered to display a biotinylatable AviTag peptide that was fused on the five p3 coat proteins. Subsequently, a biotinylated anti-MS2 antibody was specifically conjugated on p3 coat proteins through biotin-neutravidin interaction. Finally, M13 phage were functionalized with Alexa555 Fluor on the p8 major coat proteins for fluorescence imaging. The fluorescently labeled M13 phage were image using optical microscopy as diffraction-limited objects, enabling single-phage-counting as a novel LFA readout. We implemented a single-phage-counting assay for detection of model viruses, dramatically increasing detection resolution at the level of single analyte detection. The resultant assay was 1000-fold more sensitive than enzyme-linked immunosorbent assays (ELISA) and traditional colloidal-gold nanoparticle LFAs for direct detection of viruses.

2. Identify Binding Modes of Phage Reporter in LFA Membranes.

Phage transport and binding in LFA membranes were investigated using high-speed fluorescence imaging. By manipulating fluid properties to slow the translocation of phage and match the index of refraction of the glass, we visualized the binding of individual phage over time as they transported through the LFA membrane. We identified four binding modes by which phage were captured onto the functionalized membranes.

Anisotropic phage shape which was coupled with the complex flow promoted phage reorientation and facilitated binding.

3. Determine Effect of Phage Morphology on Local Binding Efficiency in Model LFAs.

Binding efficiency over time in a simplified LFA was studied as a function of the length of filamentous phage reporters. Phage bound in increased numbers as their length increased or their flux increased, consistent with the idea that mechanisms enhancing the likelihood that phage encountered the membrane increased the capture rate. By correlating the location of bound phage within the membrane to the local flow profile, we found that phage preferentially bound in the regions of faster local flow, independent of the local flow direction.

4. Identify the Mechanism of Temperature-tolerance of Mutant M13 Phage.

Six mutants of M13 phage that survive in extreme temperature environments were isolated, and their genomes were sequenced using next-generation sequencing. The five mutants showed mutations in nucleotides at gp2 and M13ori, one mutant showed mutation at gp7. We also found deletion mutants in a sample whose gene is shorter than wild-type. This sequencing result suggests three potential mechanisms for the apparent increase in temperature tolerance: gene replication enhancement (due to mutations in gp2); existence of miniphage; and mutations in the p7 coat protein.

5. Develop Sensitive A Light Detector For PoC Applications.

A sensitive detector was developed for use in a chemiluminescence point-of-care (PoC) assay. Ultrasensitive detection of light is frequently required in PoC applications, including our LFAs that use light as a visual read-out; these applications demand light detectors that are sensitive yet also portable, simple, and cheap. We demonstrated a

chemiluminescence assay for determining low levels of 1,5-anhydroglucitol (AHG) as a model analyte in a simple handheld format, using two photon sensors, a multi-pixel photon counter (MPPC) and a photomultiplier tube (PMT). We evaluated the detector sensitivities, and demonstrated that this system was able to detect AHG at a sensitivity of 5 mg l^{-1} and 0.5 mg l^{-1} LoD in a 10 μl sample using MPPC and PMT, respectively.

1.6 Overview of Thesis

In the following chapters, the dissertation is organized as follows. Chapter 2 discusses the functionalization of the phage reporter and the single-phage-counting assay. Chapter 3 discusses the binding modes of the phage reporter in the glass fiber membrane. Chapter 4 discusses the binding efficiency of the phage reporter with various morphologies and local flow regimes. Chapter 5 discusses the mechanism of temperature-tolerance of mutant M13 phage. Chapter 6 discusses the sensitive portable light detector. Finally, Chapter 7 provides a summary and conclusions of this research. An outlook of the challenges and future work is also discussed.

Chapter 2 Detection of Viruses By Counting Single Fluorescent Genetically Biotinylated Reporter Immunophage Using a Lateral Flow Assay

Abstract

We demonstrated a lateral flow immunoassay (LFA) for detection of viruses using fluorescently-labeled M13 bacteriophage as reporters and single-reporter counting as the readout. AviTag-biotinylated M13 phage were functionalized with antibodies using avidin-biotin conjugation and fluorescently labeled with AlexaFluor 555. Individual phage bound to target viruses (here MS2 as a model) captured on an LFA membrane strip were imaged using epi-fluorescence microscopy. Using automated image processing, we counted the number of bound phage in micrographs as a function of target concentration. The resultant assay was more sensitive than enzyme-linked immunosorbent assays and traditional colloidal-gold nanoparticle LFAs for direct detection of viruses.

2.1 Introduction

Reducing infection and mortality rates from viral pathogens, such as dengue[32] and Ebola viruses,[33] requires rapid and early diagnosis. This need poses a special challenge in economically challenged areas with limited laboratory infrastructure where these viruses are often endemic. Early diagnosis under these conditions is aided by point-of-care (PoC) diagnostics[1] that are able to detect viruses at low concentrations and without involved sample preparation. Traditional techniques for detecting viruses, including plaque assays and polymerase chain reaction (PCR),[10, 11] often require complex laboratory equipment and trained personnel and are therefore poorly suited for early diagnosis in these settings.

Lateral flow assays (LFAs) are a rapid, cheap, and simple option for PoC diagnosis.[7] In a typical LFA format, a biological sample containing an analyte is

dispensed onto the sample pad of a porous membrane strip and transported through it by capillary action; antibodies bound to the membrane capture the analytes as they flow through the strip. Reporter particles also transported by the flow are then analyte-bridged and arrested by antibodies at the test line to produce an easily discernible line on the strip as a positive result. LFAs using gold, dyed latex, or carbon nanoparticles as reporters require minimal sample preparation and hence are routinely used in research and clinical applications.[34] Traditional nanoparticle-based LFAs, [7−35] however, typically cannot detect viral antigens at concentrations in clinically useful ranges (e.g., 10^3–10^6 viral particles per mL for HIV-1,[36] 10^1–10^6 plaque forming units (pfu) per mL for Ebola,[37] and 10^1–10^4 plaque forming units per mL for dengue[38]) due to limited readout; for example, colloidal gold LFAs for Japanese encephalitis virus can detect viruses at a concentration of 2.5×10^6 pfu/mL[12] and filamentous *Escherichia coli* M13 bacteriophage (phage) at a concentration of 5×10^7 pfu/mL.[13] By contrast, complex laboratory methods such as plaque counting and polymerase chain reaction have much lower limits of detection.[10,11] For LFAs to be most useful as early diagnostics for viral diseases, new reporter technologies are needed with increased sensitivity and decreased limits of detection.

An intriguing alternative to the nanoparticles conventionally used as LFA reporters are viral nanoparticles, such as bacteriophage. Phage surfaces can be genetically and chemically engineered to display a wide range of functional groups, including antibodies, aptamers, lectins, peptides, proteins, and enzymes,[39, 40] enabling recognition and readout. This property allows engineered phage to serve as universal biodetection reporters in diagnostic assays,[28, 41, 42, 43] including enzyme-linked immunosorbent assays (ELISAs)[27, 26, 44, 45] and colorimetric LFAs.[46] In addition, phage bearing fluorescent

moieties have been employed in a variety of biodetection assays that use flow cytometry[47, 48, 49, 50, 22] or fluorescence microscopy[49, 51, 52] as readouts. Such fluorescently labeled phage are of particular interest for use in LFAs, as many phage (e.g., M13, T7) are large enough to be imaged using optical microscopy as diffraction-limited objects when labeled with fluorescent dyes[53, 54] and hence can be singly counted using automated image-processing routines.[55] We therefore posited that the combination of coat protein engineering and fluorescence could enable a new LFA readout, in which phage reporters bound to analytes are singly counted, that may increase LFA sensitivity.

Here, we report a lateral-flow immunoassay based on enumerating individual fluorescently labeled bacteriophage reporters. We first developed a protocol to fluorescently label the p8 major coat proteins of M13, and then functionalized the p3 tail protein displaying a biotinylatable AviTag peptide with antibodies to MS2, a widely used model for viral pathogens. At each step in the protocol, we confirmed that reporters were successfully modified using ELISA, 4′-hydroxyazobenzene-2-carboxylic acid (HABA) assay, and a magnetic particle counting assay. In the LFA, Fusion 5 membranes were functionalized with test and control lines that contain antibodies to MS2 and to the M13 reporter, respectively, as shown in Figure 2.1 [Anti-M13 and anti-MS2 antibodies were hand-spotted on Fusion 5 strips to generate test and control lines, respectively. The MS2 viruses were dispensed onto distal end of strips that were then washed in buffer. The FluorM13 reporters were spotted on the strips to sandwich MS2 viruses at the test line. Fluorescence micrographs were acquired at the test line, transition, and control line and analyzed using automated-image-processing routines to count the FluorM13 reporters]. Defined numbers of MS2 phage were flowed through the LFA matrix and captured at the

test line, which contained anti-MS2 antibodies. Fluorescent M13 reporters functionalized with anti-MS2 antibodies subsequently flowed through the strip were captured by the MS2 on the test line and by anti-M13 antibodies on the control line. We acquired fluorescence micrographs at the test, transition, and control lines and used automated image-processing algorithms to count the number of reporter phage at each location at the single-label level. The limit of detection (LoD) of this assay, determined from the 95% confidence intervals on the number of counted M13 reporters, is 10^2 plaque-forming units in a 10 μL sample deposited onto the sample pad at the end of the LFA strip, lower than that reported for colloidal-gold LFAs for viruses[12,13] or an ELISA for MS2 virus.[56] We anticipate that the imaging assay developed here can be integrated with inexpensive detection technologies, including paper microfluidics[8, 57] and smartphone-based fluorescence imaging,[58, 59] to enable point-of-care rapid diagnostics for viruses in resource-limited settings.

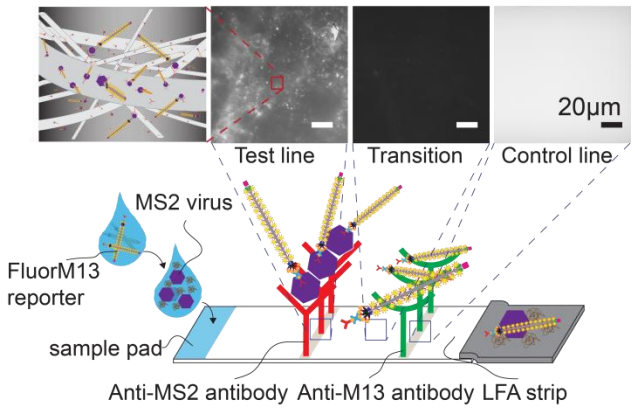

Figure 2.1 Imaging lateral flow assay with FluorM13 reporters.

2.2 Materials and Methods

Culture and Titration of MS2 Viruses and M13 Phage. MS2 virus (ATCC, #15597-B1) and its E. coli host strain (ATCC, #15597) were obtained from the American

Type Culture Collection (Manassas, VA). AviTag-displaying M13 phage (AviTag-M13) were a gift from Prof. Brian Kay at the University of Illinois at Chicago. The culturing and titering of MS2 and M13 phage were performed as described in Reference 21.

AlexaFluor 555 Labeling of AviTag-M13. AviTag-M13 were modified with AlexaFluor 555 Carboxylic Acid (Succinimidyl Ester, Life Technologies #A-20009) as illustrated in Figure 2.2 [(a) AviTag-M13 was modified with AlexaFluor 555 on the p8 major coat proteins. (b) AviTag peptides of AviTag-FluorM13 were biotinylated on the p3 tail protein *in vitro* using biotin ligase. (c) Neutravidin was conjugated onto biotin of Biotin-FluorM13 phage. (d) Biotinylated anti-MS2 antibody was attached to Neutravidin-FluorM13 through biotin-avidin conjugation]. This amine aminereactive AlexaFluor 555 was conjugated to the primary amines of the p8 major coat proteins of AviTag-M13.

PEG precipitation of AviTag-M13 was performed to replace the buffer in the stock solution with 0.2M sodium bicarbonate at pH 8.3, as the optimum reaction buffer for fluorescent labeling. For PEG precipitation, 100 μL of 10^{12} pfu/mL AviTag-M13 was mixed with 20 μL of PEG/NaCl (20% w/v PEG 8000/2.5 M NaCl), and incubated on ice for 1 h. The PEG solution was then centrifuged at 11,000g for 20 min at room temperature and the AviTag-M13 pellet was resuspended in 100 μL of 0.2 M sodium bicarbonate buffer, pH 8.3.

Next, 5 μL of 10 mg/mL AlexaFluor 555 was added to the AviTag-M13 solution, and the solution was incubated overnight at 4 ℃ on a shaker in the dark. To terminate the labeling reaction, 10 μL of 1.5 M hydroxylamine at pH 8.5 was added to the AviTag-M13 solution and incubated for 1 h at room temperature.

To remove free Alexa molecules, PEG precipitation and 7 kDa molecular weight

cutoff Zeba spin desalting columns (Thermo Scientific #89877) were used. 100 µL of 10^{12}/mL AviTag-FluorM13 were stored in the dark at 4 ℃ until used.

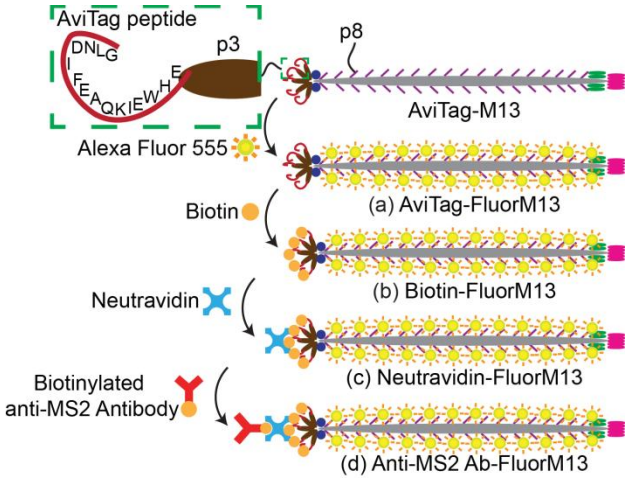

Figure 2.2 Modification of AviTag-M13.

Biotinylation of AviTag-FluorM13. AviTag-M13 phage display a peptide on the p3 tail protein which can serve as a substrate for *E. coli* biotin ligase and is inherently biotinylated at greater than 50% efficiency when grown in an E. coli host that contains the pBirA plasmid.[60]

We completed the biotinylation in vitro using E. coli biotin ligase (*birA*), according to the manufacturer's instructions (Avidity AviTag Technology) or using biotin ligase produced in-house. After incubation for 1 h at room temperature in the dark, excess biotinylation reagents were removed from the biotinylated FluorM13 (Biotin-FluorM13) solution via PEG precipitation and a 7K MWCO Zeba spin desalting column.

Neutravidin Conjugation of Biotin-FluorM13. 100 µL of a 10^{12} pfu/mL Biotin-FluorM13 solution was mixed with 10 µL of 0.1 mg/ mL neutravidin (Thermo Fisher Scientific #31000), and the resulting solution was incubated for 1 h at room temperature in the dark. To remove excess neutravidin, the solution was dialyzed for 20 h against 1L

of PBS using a Float-A-Lyzer 100 K MWCO dialysis device (Spectra/Por #G235035) with five complete buffer changes during the dialysis.

Biotinylation of Anti-MS2 Antibodies. Rabbit Anti-MS2 antibodies (Tetracore, #TC-7004−002) were biotinylated using EZLink Sulfo-NHS-LC Biotin (Thermo Scientific #21335) following the manufacturer's protocol. In brief, 10 μL of 2.8 mg/mL anti-MS2 antibody solution was mixed with 20 μL of 0.1 mg/mL EZ-Link Sulfo-NHS-LC Biotin and 90 μL of PBS. The solution was then incubated for 30 min at room temperature. A 7K MWCO Zeba spin desalting column was used to remove excess biotin.

Functionalization of FluorM13 with Anti-MS2 Antibodies through Biotin−Avidin Conjugation. Ten μL of 0.23 mg/mL biotinylated anti-MS2 antibodies were mixed with 990 μL of 1.1×10^{11} pfu/mL neutravidin-functionalized FluorM13 in PBS and incubated for 1 h at room temperature in the dark. Excess biotinylated anti-MS2 antibody was removed using a Float-A-Lyzer 300 K MWCO dialysis device with five complete buffer changes during the dialysis.

Estimation of the Biotin/Antibody Ratio of Biotinylated Anti-MS2 Antibodies Using the HABA Assay. A HABA (4´-hydroxyazobenzene-2-carboxylic acid) assay (Thermo Scientific, #28005) assay (Thermo Scientific, #28005) was used to estimate the biotin/antibody ratio of biotinylated anti-MS2 antibody.

A HABA/avidin mixture was prepared by mixing 20 μL of 10 mg/mL neutravidin, 12 μL of 10 mM HABA solution, and 368 μL of PBS. The absorbance of the 180 μL HABA/avidin mixture was measured at 500 nm. Subsequently, 20 μL of 0.23 mg/mL biotinylated anti-MS2 antibody was added to the HABA/avidin solution and the absorbance of the HABA/avidin/biotinylated-anti-MS2 antibody mixture was also

measured at 500 nm.

From the difference of the two absorbance measurements, a ratio of biotin to anti-MS2 antibody of 3.1 was estimated using the analytical formula provided by the manufacturer in Equation 2.1,

$$\frac{\text{mmol biotin/mL}}{\text{mmol protein/mL}} = \frac{\Delta A_{500}/(34{,}000b)}{\text{mmol protein/mL}}, \quad (2.1)$$

where ΔA500 is the absorbance difference between HABA/avidin and HABA/avidin/biotinylated-anti-MS2 antibody mixture at 500 nm and *b* is the light path length (in cm), typically 0.5 in the microplate used for these measurements. For HABA/avidin samples at 500 nm, at pH 7.0 the extinction coefficient is equal to 34,000 $M^{-1}cm^{-1}$.

Comparison of the Degree of Biotinylation of Biotin-FluorM13 Using ELISA. The degrees of biotinylation of AviTag-FluorM13 and Biotin-FluorM13 were compared using TMB (3,3',5,5'-Tetramethylbenzidine)-ELISA. 100 μL of AviTag-FluorM13 or 100 μL of Biotin-FluorM13 at concentrations of 0, 10^5, 10^6, 10^7, 10^8, 10^9, and 10^{10} pfu/mL in 2% (w/v) BSA were added to neutravidin-coated 96-well plates (Pierce Reacti-bind 96-well plates, Thermo Scientific #15128). After a 2 h incubation at room temperature, the plate was washed and rinsed four times each with PBST (PBS containing 0.05% (v/v) Tween 20) and PBS, respectively.

Next, bound AviTag-FluorM13 or Biotin-FluorM13 were allowed to react with 100 μL of horseradish peroxidase (HRP)-conjugated anti-M13 antibody (1:5,000 dilution) for 1 h at room temperature, followed by washing and rinsing. 50 μL of TMB was added to the plate to develop the color for 10 min and the reaction was terminated by adding 50

μL of 2 N H_2SO_4. Absorbance was measured at 450 nm in an ELISA reader (Tecan, Infinite M200 PRO).

Assessment of Anti-MS2 Antibody-Functionalized FluorM13 Using ELISA. We assessed the conjugation of rabbit anti-MS2 antibodies onto FluorM13 using ELISA. The ELISA plate was coated with 100 μL of 5 μg/mL antirabbit IgG antibody (Sigma-Aldrich, #R4880) and incubated overnight at 4 ℃. The plate wells were washed and rinsed four times each with PBST and PBS, respectively, and blocked with 300 μL of 2% (w/v) BSA in PBS for 2 h at room temperature.

100 μL of rabbit anti-MS2 antibody-functionalized FluorM13 at concentrations of 0, 10^8, 10^9, and 10^{10} pfu/mL were added to the wells and incubated for 1 h at room temperature; for the negative control experiment, AviTag-FluorM13 with no antibody was added to the wells. Bound antibody-functionalized FluorM13 were allowed to react with 100 μL of HRP-conjugated anti-M13 antibody (1:5000 dilution in 2% (w/v) BSA in PBS) for 1 h at room temperature, followed by washing and rinsing. To develop the color, 50 μL of TMB was added to the plate for 10 min, after which the reaction was terminated by addition of 50 μL of 2 N H_2SO_4. Absorbance was measured at 450 nm in the ELISA reader.

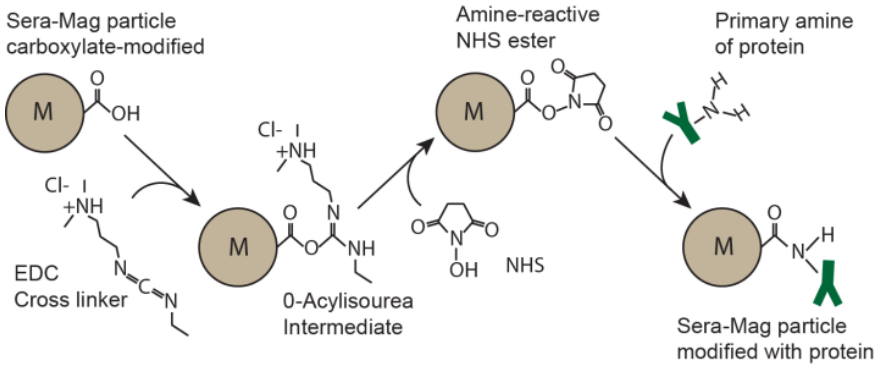

Figure 2.3 Modification of magnetic particles with proteins.

Modification of Magnetic Particles with Proteins. Carboxylated magnetic particles (1 μm diameter, Thermo Scientific, #4515−2105−050350) were coated with anti-M13 antibody, neutravidin, biotinylated-BSA, or antirabbit antibody using standard 1-Ethyl-3-(3-(dimethylamino)propyl)carbodiimide·HCl−N-Hydroxylsuccinimide (EDC-NHS) coupling, as shown in Figure 2.3.

To preactivate magnetic particles for protein coupling, we mixed 200 μL of a 5% (w/v) solution of magnetic particles with 230 μL of 50 mg/mL NHS and 230 μL of 42 mg/mL EDC in 50 mM of MES buffer at pH 6 and diluted to 1 mL by adding 340 μL of 50 mM MES buffer. The mixture was incubated for 30 min on a rotator at room temperature. The particles were washed using a magnetic stand with 50 mM of MES buffer once and PBS twice and briefly sonicated after each wash. The magnetic particles were then resuspended in 1 mL of PBS.

100 μL of 1% EDC-NHS preactivated magnetic particles were mixed with 100 μL of one of the protein solutions (0.56 mg/mL anti-MS2 antibody, 1.5 mg/mL neutravidin, 1.5 mg/mL biotinylated-BSA, or 0.5 mg/mL antirabbit antibody). After 1 h incubation on a rotator at room temperature, magnetic particles were washed with PBS three times and briefly sonicated after each wash.

For the first quenching step, magnetic particles were resuspended in 200 μL of 0.1 M hydroxylamine in PBS, and incubated for 1 h on a rotator at room temperature. Magnetic particles were washed with PBS three times and resuspended in 200 μL of 2% (w/v) BSA in PBS for the second quenching step. After overnight incubation, magnetic particles were washed and then resuspended with 200 μL of 0.1% (w/v) BSA in PBS and 0.005% ProClin300 preservative (SUPELCO, #48126).

Magnetic particle assays for characterization of functionalized FluorM13. Carboxylated magnetic particles of diameter 1 μm were coated with anti-M13 antibody, neutravidin, biotinylated-BSA, or anti-rabbit antibody using standard EDC-NHS coupling (See previous *Modification of Magnetic Particles with Proteins* section). 10 μL of a solution of protein-functionalized magnetic particles at a concentration of 1.36×10^8 particles / mL; equal to 0.01% (w/v) solution of particles was mixed with 50 μL of a solution of the functionalized FluorM13 with biotin, neutravidin, or anti-MS2 antibody at a concentration of 10^{11} pfu / mL in 2% BSA. The mixture was incubated on a slow shaker for 1 h at room temperature in the dark and then washed six times with 0.1% (v/v) Tween 20 in PBS using magnetic separation. The particles were then resuspended with 30 μL PBS.

The particle solution was pipetted into a well chamber that was formed by placing a silicon isolator (Grace Bio-Laboratories, Bend, OR; size: 4.5 mm diameter ×1.7 mm depth) on the coverslip as shown in Figure 2.4. A magnet was put under the coverslip for 10 s to pull the particles down to the coverslip surface. A light microscope (Leica, DMI 3000B) equipped with a 100× oil immersion objective lens (NA 1.4) was used to image particles in both fluorescence and brightfield modes. To detect AlexaFluor 555 using fluorescence microscopy, samples were illuminated with a 120 W mercury lamp through a filter cube consisting of an excitation filter (BP 515−560 nm), a dichromatic mirror (580 nm), and a suppression filter (LP 590 nm). A backthinned frame transfer CCD camera (Hamamatsu, C9100−12) was used to capture images with a 0.3 s shutter speed.

We acquired 20 pairs of brightfield and fluorescence micrographs of magnetic particles at the same focal area. Using an automated counting program (See below

Automated-particle-counting program section), we counted all particles in the brightfield micrographs and the bright particles that bore bound FluorM13 in the fluorescence micrographs. We examined ~5000 particles across each set of 20 images and calculated the fraction of bright particles by dividing the number of bright particles by the total number of particles.

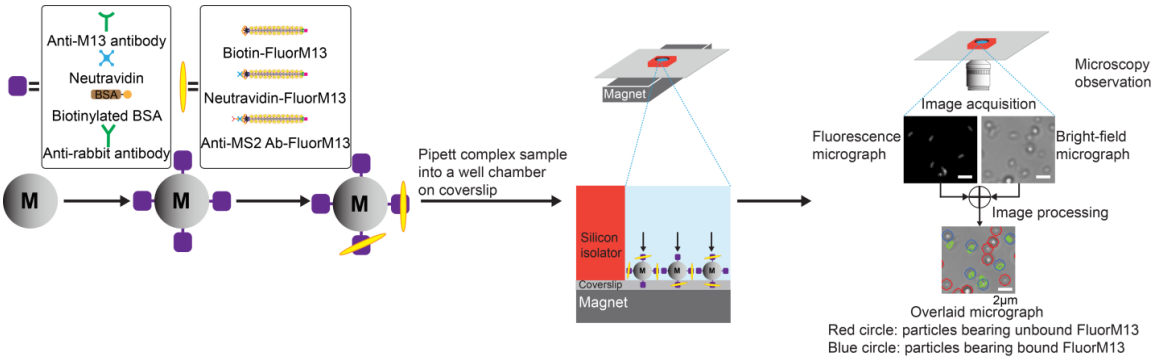

Figure 2.4 Schematic of magnetic particle assays.

Automated-particle-counting program. To quantify the extent of binding of phage to magnetic particles, we developed an automated image-processing program, briefly summarized here. We acquired brightfield and fluorescence micrographs acquired at the same focal area. Next, we processed the brightfield micrographs to locate the magnetic particles, indicated by red circles. FluorM13 phage in the fluorescence micrographs were located by identifying their silhouettes. Finally, we counted the number of bright magnetic particles by comparing the centroid positions of magnetic particles in the brightfield micrographs with the silhouettes of the Fluor M13 from the fluorescence micrographs. A flow diagram of the automated-particle-counting program is shown in Figure 2.5.

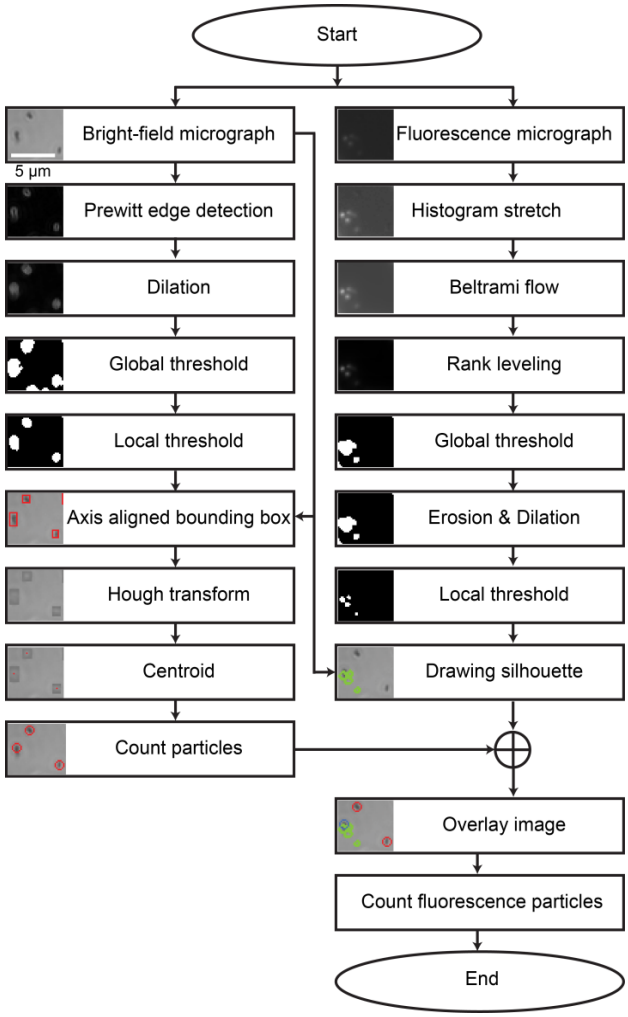

Figure 2.5 Flow diagram of automated-particle-counting program.

Image processing for brightfield micrographs. Images of magnetic particles in brightfield micrographs showed concentric rings due to diffraction.[61] To locate the particle centroids with subpixel resolution, we first calculated the centroids from the local intensity. For the x position,

$$x_c = \frac{\sum_{ij} x(i,j) I(i,j)}{\sum_{ij} I(i,j)}, \tag{2.2}$$

where (i,j) are the pixel indices; the Y position was computed analogously. To refine the centroid positions and eliminate bias due to the diffraction rings, we used a circular

Hough transform algorithm to find local peaks. The gradient field of intensity in imaged spherical particles was radially symmetric about its center. Thus, a line drawn parallel to the gradient pointed toward and intersected other such lines at the center of particles. The most likely point of intersection was a candidate for the local intensity maximum. We performed the circular Hough transform with an algorithm proposed by Peng *et al*.[61] Briefly, we first chose a local region of the axis-aligned bounding box and calculated the gradient vector of image intensity at each pixel point using the backward difference equation. Second, we created an empty two-dimensional array filled with zeros that was the same size as the axis-aligned bounding box. A line was drawn at each point with corresponding line angle $\varphi = \tan^{-1}\left(\frac{\partial I}{\partial y} / \frac{\partial I}{\partial x}\right)$ on the empty array. The length of line segment was chosen as six pixels, which was the estimated diameter of the magnetic particles in the brightfield images. The intensity of line segment was weighted by $w = \left[\left(\frac{\partial I}{\partial x}\right)^2 + \left(\frac{\partial I}{\partial y}\right)^2\right]^{1/2}$. The value of intensity was then summed and accumulated at all points where line segments overlapped. For those regions of axis-aligned bounding box that contained multiple particles, we applied a Laplacian of Gaussian filter (LOG) to the line accumulation array. Third, the image of accumulation array was thresholded with a value defined as 30-40% of maximum intensity in accumulation array, creating a binary image. Pixels of value 1 in the thresholded image corresponded to candidate particle locations for the local intensity maximum. With the particle diameter and local maxima, the centroid calculation was performed. The located particles were counted and indicated by red circles.

The local areas of axis-aligned bounding boxes for the circular Hough transform algorithm were chosen using a combination of image processing techniques. The brightfield micrographs contained the images of magnetic particles as well as artifacts that were caused by dirt on the objective lens and the camera. To differentiate magnetic particles from the artifacts on background, we used the Prewitt algorithm to enhance the edges of features. The underlying principle of edge detection is to find points where intensity changes rapidly.[62] The Prewitt operator calculates eight directions of gradient at each pixel point in an image; subsequently the pixel value at each point is replaced by the maximum value of the eight gradient magnitudes. In brightfield micrographs, the magnetic particles exhibited sharp transitions in intensity near their edges, whereas unfocused dirt and background exhibited relatively smooth changes in intensity. Therefore, after the Prewitt operation the micrograph showed a large gradient in intensity at the edges of magnetic particles and a relatively small gradient in intensity for dirt and other background features. The combination of the edge-enhancing algorithm and the pattern of concentric diffraction rings, however, led to a hole in which pixel values were lower at the particle center than at its edge. Pixels within this hole were filled with a maximal pixel value of its neighbor pixels using the dilation operation)[63].

To segment particles from background in the dilated image, global thresholding was performed to create a binary image, in which 1 and 0 corresponded to particle and background images, respectively. A single threshold value for the global thresholding was determined by $k_1\mu$, where k_1 is a tuning parameter and μ is the mean intensity value of the whole image. Because the image was unevenly illumination, a single threshold value could not be used to completely separate the particles from the background. A

lower threshold falsely identified background pixels in regions of high local average intensity as particles and also merged neighboring particles; conversely, a higher threshold reduced the feature area. We therefore used a local threshold to remove non-feature background and small isthmuses between particles, and hence recover lost foreground pixels. To determine local regions to which local threshold were applied, each connected feature resulting from the globally thresholded image was labeled using the connected-component-labeling algorithm (CCL)[63]. The labeled regions in the globally thresholded image were replaced with corresponding pixels in the dilated image, and thresholded with threshold value $k_2\mu_i$, where k_2 is a second tuning parameter and μ_i (i = 1,2,3 …) is the mean intensity value of the labeled region i in the dilated image. We again labeled the locally thresholded features using CCL. The minimal and maximal pixel (x,y) indices of the labeled feature were used to draw axis-aligned bounding box on the each feature.

FluorM13 silhouette drawing in fluorescence micrograph. Silhouette drawing of FluorM13 in fluorescence micrographs was based on binary image segmentation. To identify FluorM13 features, a combination of image processing techniques was used, including contrast enhancement, background smoothing, correction of uneven illumination, and image segmentation[55]. In our experiment, fluorescence micrographs of FluorM13 (512×512 pixel^2 at depth of 14-bit greyscale) had a narrow range of the possible grey levels, resulting in low contrast above the background. We thus first used histogram equalization to enhance contrast. The histogram equalization is defined as

$$H(i,j)=\frac{K-1}{\max\{I(i,j)\}-\min\{I(i,j)\}}\left[I(i,j)-\min_{n\times m}\{I(i,j)\}\right], \tag{2.3}$$

where $K = 2^{14}-1$ is the maximum value of the intensity in the histogram-equalized micrograph, and the maximum ($\max\{I(i,j)\}$) and minimum ($\min\{I(i,j)\}$) pixel values are the grey levels where the histogram curve of the original image falls to below (1% + offset) and (1% - offset) of the number of pixels at the maximum point of the histogram on both sides of the peak, respectively.

Histogram equalization allowed FluorM13 to be clearly seen by eye, but also produced deleterious high contrast noise in the background that decreased the signal-to-noise ratio. To reduce and smooth background noise and increase the signal-to-noise ratio while still preserving the shape of FluorM13, we used the Beltrami flow algorithm of non-linear partial differential equation, defined as

$$\frac{\partial H(i,j)}{\partial t} = (\cos\beta)\cdot\nabla h\cdot\nabla H(i,j) + (\sin\beta)\cdot h\cdot\nabla^2 H(i,j), \tag{2.4}$$

where $h = 1/\left\{1+(\partial H/\partial x)^2+(\partial H/\partial y)^2\right\}$, $H(i,j)$ is the histogram equalized image and β is a controllable parameter that determined the relative weight of edge enhancement (first term of Equation (5)) and smoothing (second term of Equation (5))[64]. The derivative was implemented using the forward and backward difference equation of the form $\partial H/\partial x = (H_{x+1}-H_x)/\Delta x$ and $\partial^2 H/\partial x^2 = \left((\partial H/\partial x)_x - (\partial H/\partial x)_{x-1}\right)/\Delta x^2$. A smoothed image after Beltrami flow equation is shown in Figure 2.5, where the number of time steps is 200, size of time step is 0.1, β = 80˚, and Δx, Δy = 1.

After these processing steps, the resultant image still showed some degree of uneven illumination and in particular was darker at the corners than at the center due to the vignetting effect.[65] The uneven illumination unfavorably affected the next step, thresholding segmentation, making it difficult to choose a single threshold value for the

whole image and producing marginal noise along the corners. To remove the uneven illumination, we used the rank-leveling algorithm[55], which is an adaptive filtering process; briefly, rank-leveling subtracts the uneven background from the image while retaining FluorM13 shape. The first step of rank leveling was to produce a background image by repeatedly replacing the intensity at each pixel with the minimum grey level in a 7 × 7 neighborhood until the FluorM13 shape disappeared from the image. The second step was to subtract the produced background from the original image. We used one iteration of rank-leveling for background generation.

To segment FluorM13 from the background, we created a binary image, where pixel values of 1 and 0 corresponded to FluorM13 and background image, respectively. For this image, global and local thresholding were used. After global thresholding, the image often contained high noise small structures and small holes within the features. To remove those artifacts, we used two morphological image processing algorithms, erosion and dilation)[63]; erosion thins objects in the binary image and is mathematically defined as $A \ominus B = \{z | (B)_z \cap A^c = \phi\}$, where A is a circular structuring element and B is the binary image, whereas dilation thickens objects in a binary image and is defined mathematically as $A \oplus B = \{z | (B)_z \cap A \neq \phi\}$. The combination of opening operation $A \oplus \{A \ominus B\}$ removed small noisy objects. Similarly, the closing operation $A \ominus \{A \oplus B\}$ reduced noisy holes in the features.

To draw the silhouette of FluorM13, we used the labeled pixels that resulted from the local threshold and seeded region growing.[66] The pixels labeled in the local-thresholded image were re-assigned to 2 and their neighbors were assigned to 1, and the background pixels remained at 0. Pixels of value 1 were then the silhouette of FluorM13.

The silhouette-drawing image was overlaid over the brightfield image. If the magnetic particles and FluorM13 silhouette overlapped, the particles were indicated by blue circles and counted as a successful binding event.

The software for automated-particle-counting program was developed in Labview 8.6 vision and motion, and graphics and sound library on a core i-7 PC (3.4 GHz CPU and 16 GB RAM). Processing of a single image took about 15 sec.

Lateral Flow Assay. Fusion 5 strips (1 mm × 50 mm × 110 μm, GE Healthcare & Life Sciences #8151−9915) were modified with 1 μL of 0.43 mg/mL rabbit anti-M13 antibody and 1 μL of 0.56 mg/mL rabbit anti-MS2 antibody in 50 mM acetate buffer at pH 3.6 by hand spotting at control and test lines, respectively.

MS2 virus samples were prepared with six time-serial dilutions in LFA buffer (10% BSA and 30% glycerol in PBS) at concentrations of 10^7, 10^6, 10^5, 10^4, 10^3, 10^2, and 0 pfu/mL. In the first step of the assay, 10 μL of each MS2 virus sample was dispensed onto the sample pad at one end of an LFA strip. Each strip was washed with 200 μL of washing buffer (0.1% Tween-20, 0.1% Triton X-100 in PBS). Next, 10 μL of 10^8 pfu/mL anti-MS2 antibody-functionalized FluorM13 in LFA buffer was dispensed onto the sample pad. Each strip was washed and rinsed with 200 μL of washing buffer and 100 μL of PBS, respectively, to remove nonspecifically bound M13 reporters.

After drying in air for 1 h, the strips were immersed with pure glycerol to match the refractive index of the Fusion 5 membrane. FluorM13 reporters bound to strips were imaged using a Leica DMI 3000B fluorescence microscope equipped with a 63× oil immersion objective lens (NA 1.4). Micrographs were acquired at the test, transition, and control lines using a back-thinned frame transfer CCD camera (Hamamatsu, C9100−12)

and analyzed using automated image-processing routines.

2.3 Results and Discussion

Characterization of FluorM13 Reporter Phage. To implement an imaging-based LFA format we developed novel reporter agents, fluorescent antibody-functionalized bacteriophage that were able to specifically bind to an analyte virus and were readily imaged at the single-reporter level using fluorescence microscopy. M13 bacteriophage modified to express the AviTag peptide were first fluorescently labeled with AlexaFluor 555 and subsequently conjugated with antibodies to MS2, as shown in Figure 2.2 Individual fluorescently conjugated phage were readily imaged using fluorescence microscopy (Figure 2.6a). Subsequently, we enzymatically biotinylated the AviTag peptide and confirmed biotinylation using a TMB-ELISA assay. The absorbance of biotin-conjugated FluorM13 on a neutravidin-coated plate was higher than that of the AviTag FluorM13 prior to conjugation, confirming that the FluorM13 phage were successfully biotinylated (Figure 2.6b). We prepared anti-MS2 antibodies with a ratio of 3.1 biotins per antibody and confirmed that the anti-MS2 antibodies were retained on the FluorM13 phage by ELISA (Figure 2.6c).

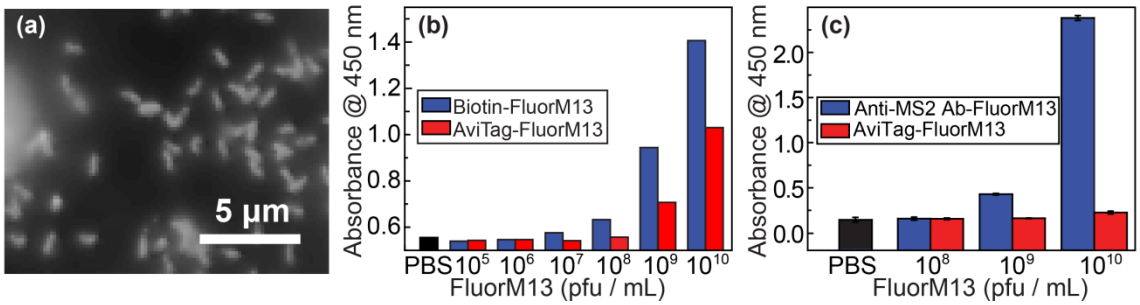

Figure 2.6 Characterization of modified FluorM13 reporters.

To further verify each of the FluorM13 functionalization steps, we employed a magnetic bead assay (Figure 2.4). We mixed magnetic particles functionalized with a variety of proteins with FluorM13 phage bearing biotin, neutravidin, or antibodies to the model virus MS2 and counted the fraction of magnetic particles that were fluorescent, signifying binding of the phage (See magnetic particle assays for characterization of functionalized FluorM13 in Method section).

Table 2.1 Experimental data from the magnetic particle assay.

Type of mgnetic particles	Type of FluorM13	Number of magnetic particles in 10 µL	Number of FluorM13 in 50 µL	Nmber of magnetic particles per micrograph (expected number= 581)	Fraction of bright magnetic particles (%)	Total number of bright particles / total number of unbright and bright particles in 20 images
Anti-M13 Ab- magnetic particle	Biotin-FluorM13	1.36×10^{6}	5×10^{9}	321 ± 32	84.0 ± 3.5	5392 / 6422
	Neutravidin-FluorM13	1.36×10^{6}	5×10^{9}	303 ± 55	81.6 ± 6.3	4921 / 6065
	Anti-MS2 Ab-FluorM13	1.36×10^{6}	5×10^{9}	257 ± 39	85.3 ± 4.0	4398 / 5148
Neutravidin-magnetic particle	Biotin-FluorM13	1.36×10^{6}	5×10^{9}	264 ± 30	98.5 ± 1.3	5469 / 5549
	Neutravidin-FluorM13	1.36×10^{6}	5×10^{9}	385 ± 68	1.9 ± 2.8	122 / 7692
	Anti-MS2 Ab-FluorM13	1.36×10^{6}	5×10^{9}	318 ± 34	74.5 ± 5.1	4699 / 6366
Biotin-magnetic particle	Biotin-FluorM13	1.36×10^{6}	5×10^{9}	429 ± 42	0.0 ± 0.1	3 / 8580
	Neutravidin-FluorM13	1.36×10^{6}	5×10^{9}	95 ± 23	89.2 ± 5.8	1696 / 1916
	Anti-MS2 Ab-FluorM13	1.36×10^{6}	5×10^{9}	503 ± 31	10.5 ± 3.1	1055 / 9009
Anti-Rabbit Ab- magnetic particle	Biotin-FluorM13	1.36×10^{6}	5×10^{9}	1223 ± 169	5.0 ± 1.2	1163 / 23250
	Neutravidin-FluorM13	1.36×10^{6}	5×10^{9}	798 ± 62	0.1 ± 0.1	18 / 15173
	Anti-MS2 Ab-FluorM13	1.36×10^{6}	5×10^{9}	556 ± 53	39.7 ± 6.7	4396 / 11124

The bottom area of the silicon chamber in this assay was 15.9 mm^2. The area of a single micrograph was 6.8×10^{-3} mm^2. 2338 images could be acquired from the bottom of the silicon chamber. Thus, because we offered 1.36×10^6 magnetic particle per chamber, we expected to observe 581 particles per micrograph. In general, because some

magnetic particles were lost during the washing step, the number of the measured magnetic particles per micrograph was slightly less than, but not significantly different from, the expected number of 581. We examined more than 5,000 magnetic particles for each sample using high-throughput automated-particle-counting program. Table 1 shows the experimental data from the magnetic particle assay. We offered FluorM13 at a number concentration that was three orders of magnitude larger than that of the magnetic particles to ensure that the fraction of bright particle would approach 100%. The fraction of bright magnetic particles per micrograph was defined as

$$\text{Fraction of bright magnetic particles} = \frac{\text{Number of bright magnetic particles}}{\text{Total number of magnetic particles}} \times 100(\%). \quad (2.5)$$

For each pair of particle and phage surface chemistries, the fluorescence signal was consistent with that expected from the surface chemistries. In pairs in which specific binding was expected (e.g., between a magnetic particle functionalized with antibodies to M13 and any of the FluorM13 phage, Figure 2.7a−c) a large fraction of magnetic particles were fluorescent, confirming good binding between phage and particles. Conversely, in those cases in which specific binding was not expected (e.g., between biotin-functionalized particles and biotin-conjugated FluorM13 phage, Figure 2.7g) few magnetic particles were fluorescent, confirming that the phage did not bind nonspecifically to the particles. We attributed the affinity of the anti-MS2 Ab FluorM13 phage for neutravidin-coated magnetic particles (Figure 2.7f) to the presence of excess biotins on the anti-MS2 antibody, which may bind to the neutravidin on the particles.

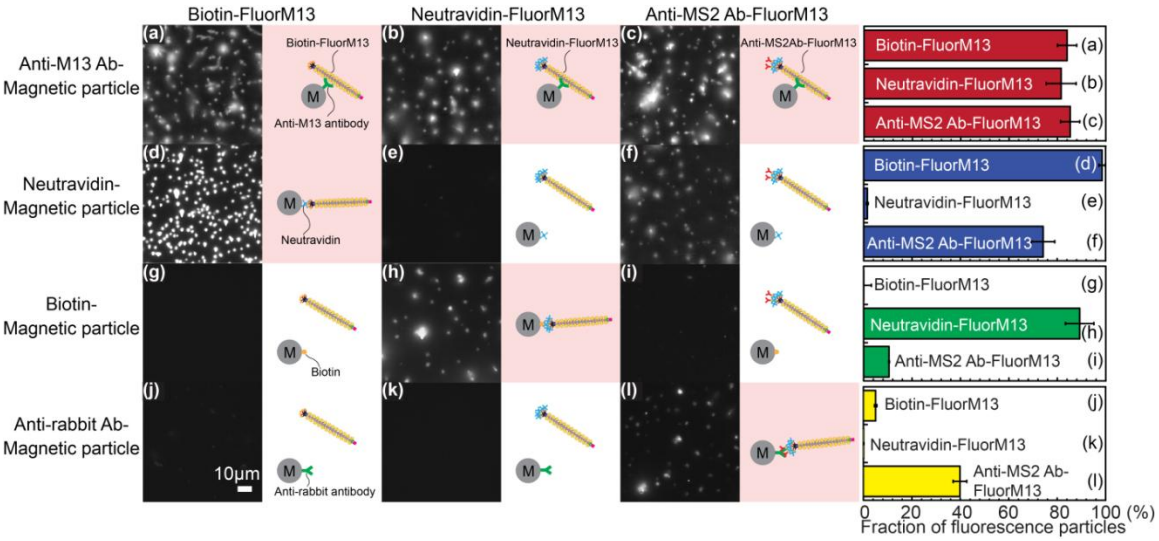

Figure 2.7 Characterization of modified FluorM13 reporters using magnetic particles.

Characterization of the antibody-conjugated Fusion5 LFA matrix. To confirm that the LFA test matrix could be successfully conjugated with antibodies both to the reporter phage M13 and to the model virus MS2, anti-rabbit IgG antibodies conjugated with HRP were applied to Fusion 5 strips spotted with rabbit anti-M13 and rabbit anti-MS2 antibodies. The intensity of the color generated increased with the anti-M13 or anti-MS2 antibody concentration (Figure 2.8 [HRP-conjugated-anti-rabbit antibody was spotted on a Fusion 5 membrane to detect rabbit anti-M13 antibodies (top line) and rabbit anti-MS2 antibodies (bottom line) immobilized on the strips at various concentrations. The color intensities from the TMB reaction confirmed that more antibodies were retained on the strips as the antibody concentration increased]), indicating that the number of HRP-conjugated antibodies retained on the strips was proportional to the concentration spotted on the strips.

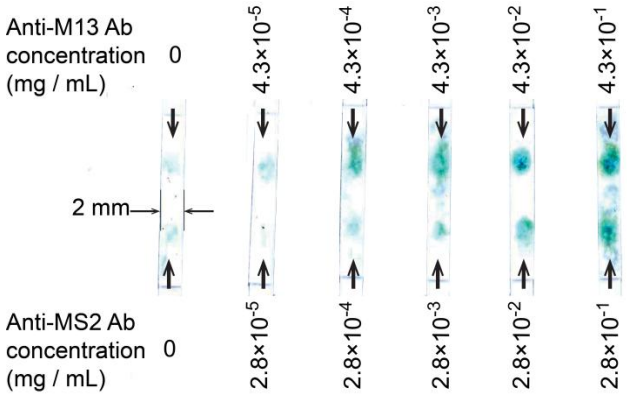

Figure 2.8 Confirmation of anti-MS2 and anti-M13 antibody attachment to Fusion 5 membranes.

Automated Image Processing to Count Individual Phage in LFA Membrane. To efficiently quantify the number of reporter phage bound to the LFA strip, we developed and employed an automated algorithm that locates and counts the number of the fluorescent phage in fluorescence micrographs (Figure 2.9 [(a) A fluorescence micrograph was acquired at the LFA test line. (b) Histogram equalization[67] was used to enhance image contrast, allowing FluorM13 reporters to be clearly visible. (c) The Beltrami flow algorithm[68] was used to reduce and smooth background noise and increase the ratio of signal to noise, while preserving the shape of the FluorM13 reporters. (d) A rank-leveling algorithm[67] was used to remove uneven illumination. (e, f) Global and local thresholds[67] were used to segment FluorM13 reporters from the background. (g) Brightfield micrograph acquired at the same focal area as in (a) of the LFA test line. (h) A connected component labeling algorithm[69] was used to automatically count FluorM13 reporters. The segmented M13 phage reporters were overlaid onto the brightfield micrograph. (i) FluorM13 identified by the algorithm were indicated by axis-aligned bounding boxes. The scale bar for all images is 10 μm]). The software enhanced the image contrast and increased the ratio of signal-to-noise, allowing phage to be counted

even against a noisy or unevenly illuminated background. In addition, the image processing preserved the nonspherical shape of the FluorM13 phage, which helps to confirm their identity and allows their orientation when bound to the strip to be determined.

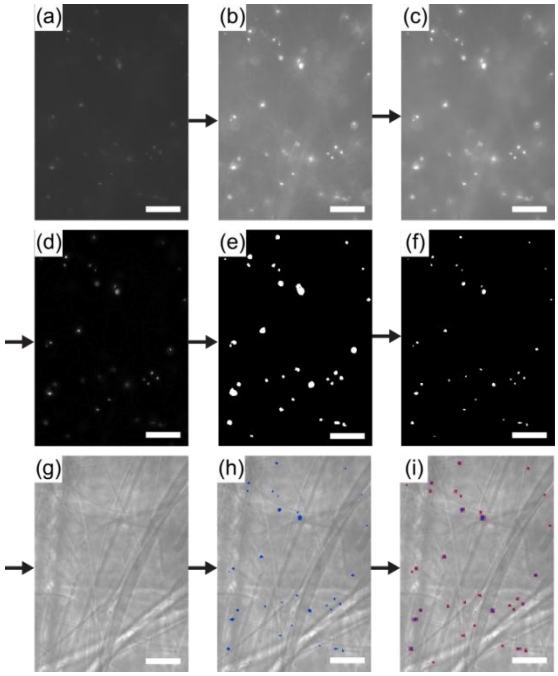

Figure 2.9 Automated counting of individual FluorM13 reporters.

Imaging-LFA Immunodetection of MS2 Virus. To demonstrate the efficacy of our assay we chose as the analyte MS2 virus, which often serves as a model for viral pathogens. We deposited 10 μL of a solution containing a known concentration of MS2 on a sample pad at one end of antibodyfunctionalized LFA strips. Capillary action transported the MS2 viruses through the strip to the test line, where anti-MS2 antibodies captured them. Anti-MS2 Ab Fluor M13 reporters subsequently transported through the strip were captured both by the MS2 viruses bound to the matrix at the test line in a sandwich and by anti-M13 antibodies at a downstream control line. The uniformly bright

micrographs acquired at the control line indicated that many M13 reporters were transported through the strip (Figure 2.10, top row).

Individual bright spots in micrographs acquired upstream at the test line (Figure 2.10, bottom row) or in a nonfunctionalized transition region between the test and control lines (Figure 2.10, middle row) corresponded to individual M13 reporters bound to the strip. Resolving individual reporters required matching the refractive index of the Fusion 5 strip ($n \approx 1.5$) to the solvent, here pure glycerol. Without index matching, scattering from the strip limited our ability to resolve single phage. The low number of bound phage in the transition area at each concentration compared to the test line indicated that nonspecific binding did not increase with increasing analyte concentration.

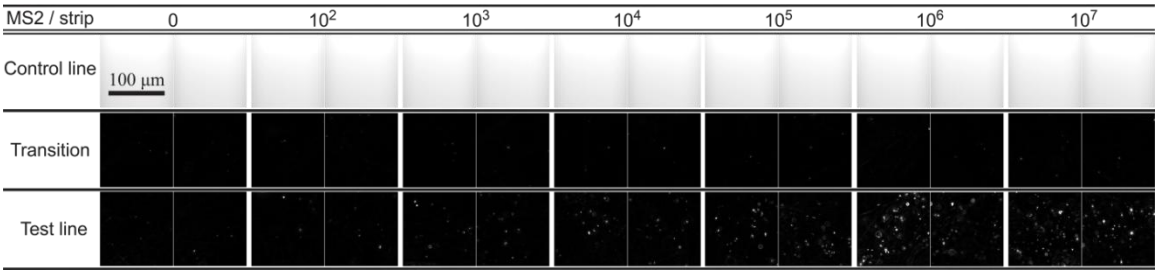

Figure 2.10 Representative micrographs from imaging LFAs for MS2 virus detection**.**

To determine the limit of detection of the imaging LFA, we quantified the number of reporters bound at the test line and in the transition region using the automated image-processing program summarized in Figure 2.9. The average number of bound reporters per micrograph acquired at the test line increased with increasing concentration of analyte MS2 viruses (Figure 2.11) but at a rate that was significantly less than linear: as the MS2 concentration was increased from 10^2 to 10^7 pfu per 10 μL, the number of bound phage increased by a factor of 5. The lack of proportionality between signal and offered analyte concentration, also observed in other assays with phage reporters,[43,46] likely arose from

steric hindrance and the great heterogeneity of the binding sites offered by the LFA matrix.

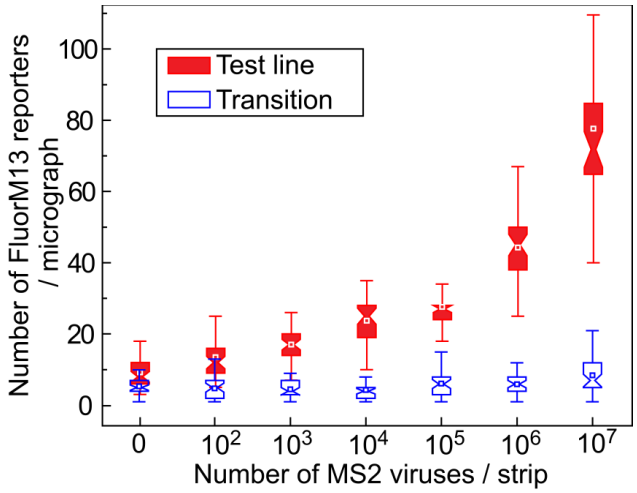

Figure 2.11 Limit of detection of LFA.

We compared the number of bound reporters at the test line to that in the transition region to determine whether sufficient signal above the background was achieved. Twenty pairs of brightfield and fluorescence micrographs were acquired at the test line and in the transition region. We set as the null hypothesis that there was no difference between the test line and the transition region and chose the level of significance as α=0.05. Then, the reject t-value of $t_{0.05/38}$ was 2.03 from the T-distribution table, where the number of degrees of freedom was 38 ($df=n_{tl}+n_{bkg}-2$, where n_{tl} and n_{bkg} are the number of micrographs acquired at the test line and the transition region, respectively). The t-test statistic t_s is defined as

$$t_s = \frac{\bar{x}_{tl} - \bar{x}_{bkg}}{\sqrt{\frac{s_p^2}{n_{tl}} + \frac{s_p^2}{n_{bkg}}}}, \tag{2.6}$$

where $s_p^2 = \frac{(n_{tl}-1)s_{tl}^2 + (n_{bkg}-1)s_{bkg}^2}{n_{tl}+n_{bkg}-2}$ is the pooled variance, $\bar{x}_{tl}$ is the averaged number of FluorM13 reporters per micrograph at the test line, $\bar{x}_{bkg}$ is the averaged number of FluorM13 reporters per micrograph at the transition region, s_{tl}^2 is the variance of number of M13 phage reporters per micrograph at the test line and s_{bkg}^2 is the variance of number of M13 phage reporters per micrograph at the transition region. If $t_s > t_{0.05/38}$, the null hypothesis was rejected, and we concluded that the test line was statistically distinct from the background area. As shown in Table 2.2, the average number of bound reporters at the two locations was different at a significance level of α=0.05, and the null hypothesis was rejected for all analyte concentrations. Thus, we concluded that the number of bound reporters at the test line was statistically different from that in the transition region for all analyte concentrations tested down to 10^2 pfu per 10 μL, corresponding to a titer of 10^4 pfu/mL. The false signal appeared at the negative control experiment (0 MS2 pfu per strip), showing a small amount of nonspecific binding there; the extent of false binding was constant for all analyte concentrations studied.

Table 2.2 T-test for the bound FluorM13 reporter between test line and background area in LFA strip

MS2 pfu per strip	**0**	**10^2**	**10^3**	**10^4**	**10^5**	**10^6**	**10^7**
$\bar{x}_{tl}$	8.7	13.2	17.1	23.0	26.7	44.8	78.4
s_{tl}^2	14.1	21.8	23.3	45.2	26.3	101.5	604.1
$\bar{x}_{bkg}$	5.4	4.7	4.4	4.3	6.4	6.0	8.7
s_{bkg}^2	7.1	8.0	4.5	7.6	12.6	7.9	34.3
s_p^2	10.6	14.9	14.1	26.4	19.4	54.7	319.2
t_s	4.5	9.7	15.0	16.3	20.6	23.4	17.4
$t_{0.05/38} = 2.03$	H_a	H_a	H_a	H_a	H_a	H_a	H_a

(continue Table 2.2)

$\bar{x}_{tl}$: Averaged number of FluorM13 reporters per micrograph at test line.
s_{tl}^2: Variance of number of FluorM13 reporters per micrograph at test line.
$\bar{x}_{bkg}$: Averaged number of FluorM13 reporters per micrograph at background area.
s_{bkg}^2: Variance of number FluorM13 reporters per micrograph at background area.
s_p^2: pooled variance
t_s: t-distribution
H_o: $\bar{x}_{tl} = \bar{x}_{bkg}$ (null hypothesis)
H_a: $\bar{x}_{tl} > \bar{x}_{bkg}$ (alternative hypothesis)

Additionally, the 95% confidence intervals for samples with nonzero MS2 concentration down to 10^2 pfu per 10 μL, indicated by the notches in Figure 2.11, did not overlap with that of the zero MS2 concentration at the test line. Using as the criterion for the limit of detection the lack of overlap in the 95% confidence intervals of the number of bound M13 reporters, these results suggested that this assay could be used to detect as few as 10^2 pfu per 10 μL. An independent replicate of the assay exhibited an identical limit of detection (Figure 2.12 [An independent replicate experiment of the assay exhibited an identical limit of detection by all metrics studied (p values, non-overlapping 95% interval notches, mean + 3 SD)]). We concluded that the limit of detection of this assay was $\sim 10^2$ pfu/strip. This LoD was approximately one-hundred-fold better than that reported for virus LFAs using gold nanoparticles as reporters[12],[13] and that reported for an ELISA[56] for MS2.

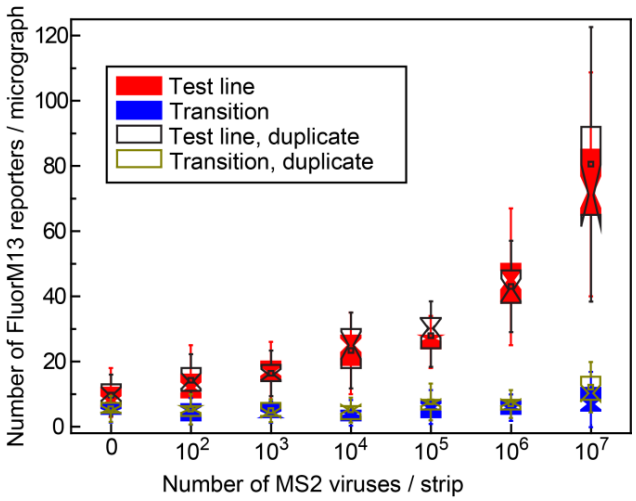

Figure 2.12 An independent repeat of the assay.

2.4 Conclusions

We report here a lateral flow immunoassay for viruses that employs fluorescently labeled M13 bacteriophage as reporters. This assay relies on the fact that individual filamentous phage can be resolved and hence counted using standard fluorescence microscopy. The limit of detection for our imaging LFA was significantly better than that of conventional LFAs using gold nanoparticles[12,13] and that of an ELISA for MS2,[56] due in part to the resolution attained by imaging individual reporters bound to single analyte viruses.

We expect that the LoD can be lowered further by reducing nonspecific binding of the reporters in the background region and by optimizing the deposition of the test line to maximally concentrate the antibodies there. Additionally, we anticipate that tuning the chemistry and geometry of the LFA strip may further improve the LoD. An ideal strip for this assay allows easy transport of the reporters to all antibody-functionalized sites and aids capture of the reporters; in future work, we therefore plan to vary the strip material as well as the size and arrangement of the pores therein. Finally, because reporters must

be readily transported throughout the strip, we surmise that the shape of the reporter phage may affect the LoD; to test this idea, we will test the efficacy of functionalized viral nanoparticles of varying morphologies as reporters in this assay.

We envision that the imaging-based LFA described here can be integrated with other advances in detection to generate a simple and inexpensive diagnostic for viruses that is suitable for point-of-care applications. Adapting our LFA into a paper microfluidics format has the potential to reduce the number of handling steps and decrease costs, and would thus be promising for use in areas with few trained medical workers.[70]

Fluorescence has already enabled multiplexed detection in a variety of modified LFAs[71] and multiplexed fluorescence imaging is easy to implement in our assay format. Similarly, combining our LFA with smartphone-based imaging methods, [59,72] which have already been used to image individual viruses,[38] would generate a portable diagnostic. Moreover, recent advances in 3-D printing have demonstrated smartphone-compatible imaging systems that can magnify at 1000× (the magnification used in this study), and cost less than a dollar for all materials[73] compatible with point-of-care diagnostics in resource-limited settings.

Chapter 3. Binding modes of reporters in a viral-nanoparticle lateral-flow assay

Abstract

Using microscopy and image analysis, we characterize binding of filamentous viral nanoparticles to a fibrous affinity matrix as models for reporter capture in a lateral flow assay (LFA). M13 bacteriophage (M13) displaying an *in vivo*- biotinylatable peptide (AviTag) genetically fused to the M13 tail protein p3 are functionalized with fluorescent labels. We functionalize glass fiber LFA membranes with antibodies to M13, which primarily capture M13 on the major p8 coat proteins, and with avidin, which captures M13 at the Biotinfunctionalized tail, and compare modes of reporter capture for the side- versus tip-binding recognition interactions. The number of captured M13 is greater for side-binding than for tip-binding, as expected from the number of recognition elements. Whereas two-thirds of side-bound M13 that are captured by an anti-M13 antibody bind immediately after colliding with the membrane, tip-bound M13 prominently exhibit three additional binding modes that require M13 to reorient to enable binding. These results are consistent with the idea that the elongated M13 shape couples with the complex flow field in an open and disordered fibrous LFA membrane to enhance capture.

3.1 Introduction

Lateral flow assays (LFAs) are a rapid, inexpensive, and simple format for point-of-care or point-of-use immunoassays.[74] Commonly employed for home use as the home pregnancy test (to detect human chorionic gonadotropin), LFAs have been demonstrated to detect antibodies,[75] viruses,[76] bacteria,[77] parasites,[78] nucleic acids,[79] proteins,[80] drugs,[81] and toxins.[82] In the commonly-employed sandwich lateral flow format, a porous

membrane and particulate reporters (traditionally colloidal gold nanoparticles) are functionalized with antibodies to the analyte of interest. Subsequently, a sample containing analytes is wicked into the membrane by capillary forces. The reporter particles bind to the analyte and are subsequently captured by the antibodies at the test line to generate a colorimetric visual signal. Sandwich LFAs require little or no sample preparation and generate a rapid and easily-read result, two significant advantages for a point-of-use diagnostic in resource-limited settings.[76c, 77b, 83] In most current implementations, however, LFAs are semi-quantitative and are insufficiently sensitive to detect analytes at extremely low concentrations – for example, to detect most viruses at clinically-relevant concentrations. Indeed, a wide range of applications requiring point-of-use monitoring, including biopharmaceutical manufacturing, food processing, environmental monitoring, and biodefense, and would benefit from new LFA formats with improved sensitivity.

One common strategy to increase the sensitivity of sandwich LFAs is to develop new reporters and/or readouts that enable quantitative measures of the analyte concentration. A wide variety of synthetic nanomaterials have been explored as alternatives to colloidal gold, including fluorescent[34] or luminescent[84] nanoparticles,[85] quantum dots[86], iron oxides,[87] and phosphors.[88] Similarly, alternate methods to modulate the flow of reporters through the strip have been proposed, including electrophoresis,[89] isotachophoresis,[90] and flow delay.[91] Finally, proposed ultrasensitive readouts include volumetric magnetization,[92] near-infrared detection,[93] surface-enhanced Raman spectroscopy,[94] fluorescence,[95] chemiluminescence,[79a, 96] phosphorescence[97], and thermal contrast.[98] In addition, much recent work has focused on smartphone-compatible

readouts[99] that are suitable for settings lacking sophisticated laboratory infrastructure or instrumentation. Despite these and other significant advances towards quantitative and ultrasensitive LFA formats, there remains a continuing need for flexible, inexpensive approaches that increase LFA sensitivity.

Towards increasing LFA sensitivity by increasing the signal-to-noise ratio at low analyte concentrations, reporters that exhibit low non-specific binding provide an intriguing route forward. Recently, we have employed M13 bacteriophage (M13) decorated with enzymes as viral-nanoparticle reporters in ultrasensitive LFAs.[100] Filamentous M13 is highly anisotropic, with length of approximately 900 nm (depending on genome size) and width of approximately 6.6 nm. These bacteriophage (phage) have been genetically or chemically engineered to display a wide range of functional groups for applications in bionanotechnology[101] and in nanomedicine.[102] Here, phage are appealing candidates as LFA reporters because they are historically under Darwinian selection to exhibit low non-specific binding; are readily coupled to recognition elements;[42, 103] are capturable, in principle, by a single analyte and/or recognition element; and are detectable at the single-reporter level. Remarkably, the viral-nanoparticle-based LFAs developed to date exhibit sensitivities for model analytes (viruses[100a-c] and proteins[100d]) that are one-hundredfold to one-thousandfold greater than traditional gold-nanoparticle-based LFAs. The mechanisms underlying the ultrasensitivity of viral-nanoparticle-based LFAs, however, remain poorly understood. We speculate that the enhanced sensitivity arises from the binding and capture properties of M13 viral nanoparticles in LFA membranes. Systematic investigations of phage transport and

binding at the pore scale are hence expected to generate insight into the origins of the improved sensitivity of viral-nanoparticle-based LFAs.

Here, we characterize the transport and binding properties of functionalized M13 phage as reporters in a model LFA designed to enable pore-scale imaging. We functionalize glass fiber LFA membranes with either antibodies to M13 phage, which are able to capture the phage on the (approximately 2,700) copies of the major p8 coat protein, or with NeutrAvidin, which captures the phage via biotin conjugated to one or more of the five p3 minor coat proteins on the phage tip. By manipulating fluid properties to slow the translocation of phage and match the index of refraction of the glass, we visualize the binding of individual phage over time as they transport through the LFA membrane. We identify four modes by which phage are captured onto the functionalized membranes. For phage that laterally (side-)bind through the anti-M13 antibody, most binding occurs immediately after phage collide with a fiber within the membrane. Three additional modes contribute significantly for phage that tip-bind (via NeutrAvidin) onto fibers, all of which involve the local flow re-orienting phage to align parallel to the fiber prior to binding. These experiments confirm that individual phage can be captured by a single recognition element (at the phage tip), and are consistent with the idea that the anisotropic phage shape coupled to the complex flow promotes reorientation to facilitate binding.

3.2 Materials and Methods

Culture and titration of M13 phage. AviTag-displaying M13 phage (AviTag-M13) are a gift from Prof. Brian Kay at the University of Illinois at Chicago. The culturing and titering of M13 phage are performed as described previously.[104] Briefly, for phage growth,

10 µl of 10^6 pfu ml^{-1} AviTag-M13 is pre-mixed with 100 µl of a fresh overnight *Escherichia coli* TG1 culture. After phage are allowed to adsorb to TG1 for 2 h at 37°C, the pre-mixture is transferred to 500 ml of 2×YT(2× Yeast extract and Tryptone) broth medium in a 2.8 l flask, and growth continues overnight at 37°C. Bacteria are removed from the lysate by centrifugation followed by filtration through a 0.45 µm filter (Corning, #430512), and the purified phage are concentrated in 1 ml of phosphate-buffered saline (PBS) using poly(ethylene glycol) (PEG) precipitation. For phage titration, 300 µl of a mid-log TG1 culture is mixed with 10 µl of the serially-diluted phage stock solutions. After adsorption for 15 min, a solution containing 40 µl of 40 mg ml^{-1} X-Gal (5-bromo-4-chloro-3-indolyl-β-D-galactopyranoside), 10 µl of 500 mM IPTG (Isopropyl β-D-1-thiogalactopyranoside), and 5 ml of 0.7% top agar is added and spread on a pre-warmed Luria-Bertani (LB) plate. After overnight growth, the blue plaques due to X-Gal and *β*-galactosidase encoded by the *lacZ* contained in the AviTag-M13 gene are counted to calculate the concentration of the phage stock solution.

Biotinylation of AviTag-M13. AviTag-M13 are partly biotinylated on the p3 tail protein during assembly in *E. coli*, then further biotinylated *in vitro* using *E. coli* biotin ligase (birA) either purchased or prepared in-house, following the manufacturer's instructions (Avidity AviTag Technology). After incubation for 1 h at room temperature, excess biotinylation reagents are removed from the biotinylated phage solution via PEG precipitation and a 7K molecular-weight cutoff (MWCO) Zeba spin desalting column.

AlexaFluor 555 labeling of biotinylated-M13. Biotinylated M13 (Biotin-M13) are modified with AlexaFluor 555 Carboxylic Acid (Succinimidyl Ester, Life Technologies #A-20009) as previously described[100c] and illustrated schematically in Figure 3.1a. Phage

in these experiments are capturable by either one of two recognition elements: by anti-M13 antibodies, which can capture phage on any of the 2,700 p8 coat proteins, or by NeutrAvidin, which can capture phage only through the biotin attached to one or more of the five p3 tail proteins (Figure 3.1b).

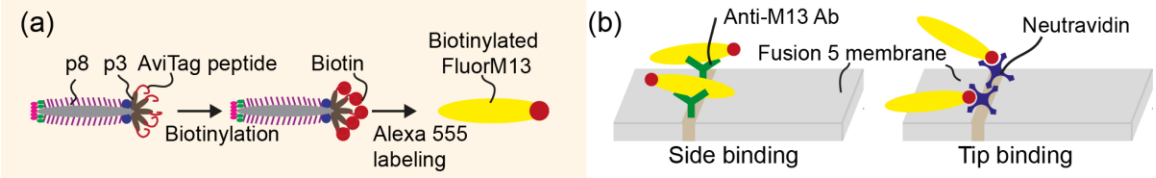

Figure 3.1 Schematic of phage modification and capture.

Comparison of the degree of biotinylation of Biotin-FluorM13 phage using enzyme-linked immunosorbent assay (ELISA). The degrees of biotinylation of AviTag-M13 and Biotin-FluorM13 are evaluated using TMB (3,3',5,5'-Tetramethylbenzidine)-ELISA. 100 µl of AviTag-M13 or 100 µl of Biotin-FluorM13 at concentrations of 0, 10^4, 10^5, 10^6, 10^7, 10^8 and 10^9 pfu/mL in 2% (w/v) BSA are added to neutravidin-coated 96-well plates (Pierce Reacti-bind 96-well plates, Thermo Scientific #15128). After a 2 h incubation at room temperature, the plate is washed and rinsed four times each with PBST (PBS containing 0.05% (v/v) Tween 20) and PBS, respectively. Next, bound AviTag-M13 or Biotin-FluorM13 are allowed to react with 100 µl of horseradish peroxidase (HRP)-conjugated anti-M13 antibody (1:5,000 dilution) for 1 h at room temperature, followed by washing and rinsing. 50 µl of TMB (3,3′,5,5′-Tetramethylbenzidine) is added to the plate to develop the color for 15 min, and the reaction is terminated by adding 50 µl of 2 N H_2SO_4. Absorbance is measured at 450 nm in an ELISA reader (Tecan, Infinite M200 PRO). As the control experiments, we perform

an ELISA test for wild type M13 (ATCC, #37468) and Biotin-FluorM13 on neutravidin- and BSA-coated 96-well microplates, respectively.

Flow experiments and image analysis. Fusion 5 LFA matrix strips (3 mm × 50 mm × 0.35 mm, GE Healthcare & Life Sciences #8151−9915, pore diameter 11 μm [reported by manufacturer], average fiber diameter D = 4.35 ± 1.90 μm [measured]) are modified with 3 μl of 1 mg ml^{-1} NeutrAvidin (Thermo Scientific, #3100) or 0.43 mg ml^{-1} polyclonal rabbit anti-M13 antibody (Novus Biologicals, #NB100-1633) in 50 mM acetate buffer at pH 3.6 by hand spotting at a fixed distance of 1 cm from the downstream end of the strip. After drying in air for 2 h at room temperature, each functionalized strip is placed on a large coverslip (48 × 65 mm, Gold Seal), covered with a second smaller coverslip (22 × 22 mm, Fisher Brand), and moved onto the stage of an epifluorescence microscope (Leica DMI 3000B) equipped with a 63× oil immersion objective lens (NA 1.4), as shown in Figure 3.2. For the model LFA experiments, Biotin-FluorM13 are suspended in a background solution containing 0.2 w/v % hydrolyzed polyacrylamide (HPAM, FLOPAAM 3330, SNF, weight-averaged molecular weight of 8 MDa) and 30% v/v glycerol in PBS. Subsequently, 25 μl of 10^7 pfu ml^{-1} Biotin-FluorM13 is dropped on the upstream end of the strip.

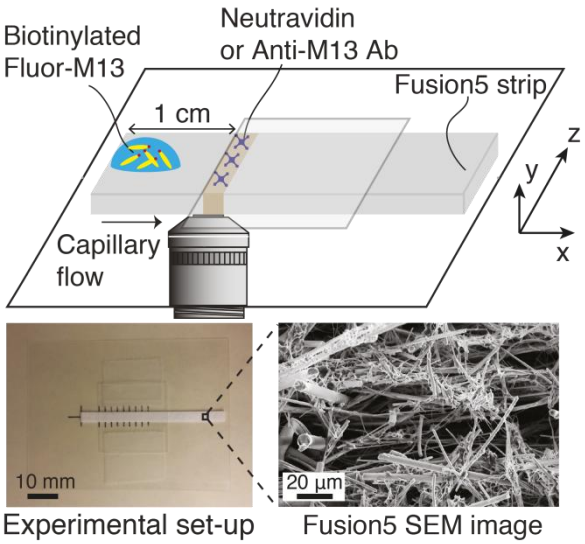

Figure 3.2 Schematic of experimental setup.

Biotin-FluorM13 are imaged in capillary-driven transport through the membrane using a sCMOS camera (pco.edge 4.2, 30 frame/sec, 20 μs exposure time, 208 μm × 213 μm image field of view). Recording begins immediately after liquid breakthrough in the field of view and ceases when the phage particles exhibit only Brownian (rather than advective) motion, typically nine minutes. Four movies are analyzed for anti-M13 functionalized membranes; fourteen movies are analyzed for the NeutrAvidin-functionalized membranes. The average number of bound Biotin-FluorM13 phage per movie for anti-M13 antibody, NeutrAvidin, and unfunctionalized (bare) strips is 89.0 ± 19.8, 7.2 ± 1.9, and 0.2 ± 0.4, respectively.

The centroids of individual Biotin-FluorM13 are located in two dimensions using the Hough transform algorithm.[105] Phage centroid positions are linked into trajectories and tracked over time using multiple hypothesis tracking (MHT) software downloaded from http://www.multiplehypothesis.com/. Analysis of the relative angles between the tracked phage and the capturing fibers is performed manually.

Fluid flow simulation. Fluid flow in a very simplified model membrane is simulated using a 3D laminar flow model in COMSOL Multiphysics 4.1. The simulation box has dimensions of 100 μm × 100 μm × 100 μm with two fibers of radius 2.5 μm spanning the size of the box. The inlet is specified to have a uniform velocity distribution normal to the *yz* plane at $x = 1$ with the outlet on the opposite face of the box at $x = 0$. One fiber is oriented along the (1,1,1) vector and makes a 45° angle to inlet flow when projected onto the *xy* and *xz* planes. The other fiber is oriented along the (1, -1, 1/3) vector and makes a 45° angle to the flow when projected onto the *xy* plane and approximately a 20° angle when projected onto the *xz* plane. The remaining external boundaries are open. The fiber surfaces are specified to have a no-slip boundary condition. The non-Newtonian fluid is modeled as a power law fluid with a viscosity $\eta = k\dot{\gamma}^{m-1}$ with $k = 0.62$, $m = 0.36$, and a zero-shear viscosity of 2.7 Pa s, consistent with previously reported rheology of a 0.1 wt% HPAM solution.[106]

3.3 Results and Discussion

Characterization of Biotin-FluorM13. After functionalizing M13 phage with biotin and AlexaFluor 555, we take representative fluorescence micrographs of the Biotin-FluorM13 which are shown in Figure 3.3a. To verify that Biotin-FluorM13 retains biotins, we conduct ELISA test on Neutravidin plate. Both the AviTag-FluorM13, which are inherently biotinylated by our *E. coli* host cells, and the *in vitro* Biotin-FluorM13 exhibit positive ELISA outputs (Figure 3.3b). The *in vitro* Biotin-FluorM13 show 130% greater biotinylation compared to AviTag-M13. The wild type and Biotin-FluorM13 do not give ELISA signals on the neutravidin- and BSA-coated plates, respectively, confirming that the Biotin-FluorM13 are specifically bound to neutravidin-coated plates.

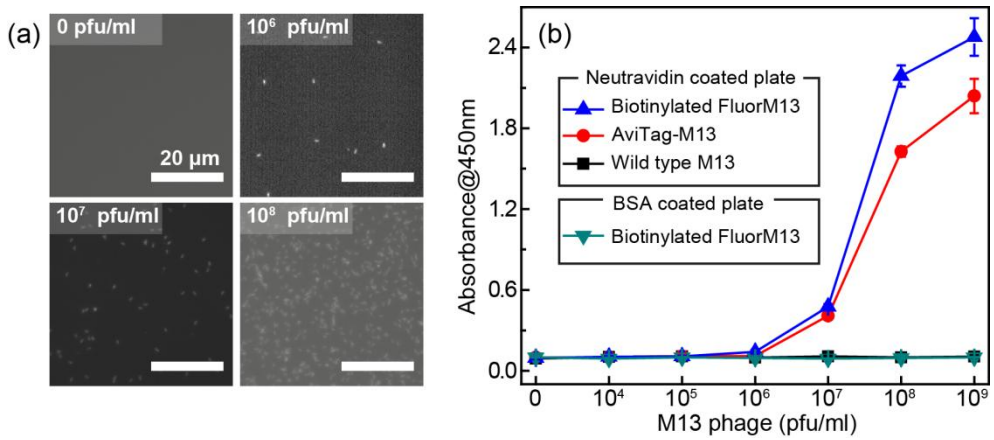

Figure 3.3 Characterization of biotinylated FluorM13.

Protocols for a binding-imaging assay in LFA membranes. In phage-nanoparticle LFAs, an aqueous PBS buffer solution rapidly travels through a membrane strip of 3 mm width and 5 cm length in several seconds, driven by capillary force; from the position of the liquid interface as a function of time, we estimate that the average velocity at which phage in PBS flow through the Fusion 5 membrane is 1.8 mm/s. Although in principle M13 phage moving at these velocities can be imaged using a fast camera, there remains a second limitation for imaging of binding at the pore scale: the refractive index mismatch between the PBS (index of refraction n = 1.33) and the glass Fusion5 membrane (n = 1.51) significantly increases scattering and hence limits the distance into which membranes can be imaged. Therefore, for single-phage imaging experiments we formulate a model viscous solvent that nearly matches the index of refraction of the Fusion 5 membrane to allow us to image up to 20 μm into the membrane from below, using an inverted microscope. We mix glycerol at 30% by volume with 0.2% by weight of partially-hydrolyzed poly(acrylamide) (HPAM) in PBS, and use this as the background solution for phage binding experiments. The viscosity of this solution, measured at a fixed shear rate of 42 s^{-1} using an Ubbelohde viscometer, is μ = 17.2 mPa-s; its density is

ρ = 1.08 g ml^{-1}; and its index of refraction is n = 1.39. Because the membrane is disordered, the resistance to flow can be described by an isotropic term on large length scales (i.e. we do not expect that the viscoelastic fluid will generate anisotropic transport).[107] We confirm via a control enzyme-linked immunosorbent assay (ELISA) on anti-M13 antibodies (for side-binding) or NeutrAvidin (for tip-binding) plate that the binding of the phage is minimally affected by the presence of the glycerol and the HPAM (Figure 3.4 [TMB-ELISA is performed to determine if the background solution used in the flow-imaging experiments (30 v/v % glycerol and 0.2 w/v % HPAM in PBS) affects the binding interaction between biotinylated Fluor-M13 and anti-M13 antibody or neutravidin. Here, the degree of binding for phage in flow solution is compared to that in PBS buffer. For side-binding, we add biotinylated Fluor-M13 at concentrations of 0, 10^6, 10^7 and 10^8 pfu/mL in the background solution or PBS to a 96-well microplate that is coated with anti-M13 antibody. For tip-binding, biotinylated Fluor-M13 are added to a neutravidin-coated plate. After washing the plates, we add (HRP)-conjugated anti-M13 antibody to both plates, followed by washing and rinsing. After adding TMB to the plates, we measure the absorbance at 450 nm. The side- and tip-binding of the biotinylated Fluor-M13 are not significantly affected by the background solution; the difference in absorbance between binding in flow solution and in PBS buffer is less than 10%.]) and hence use this solution for imaging experiments.

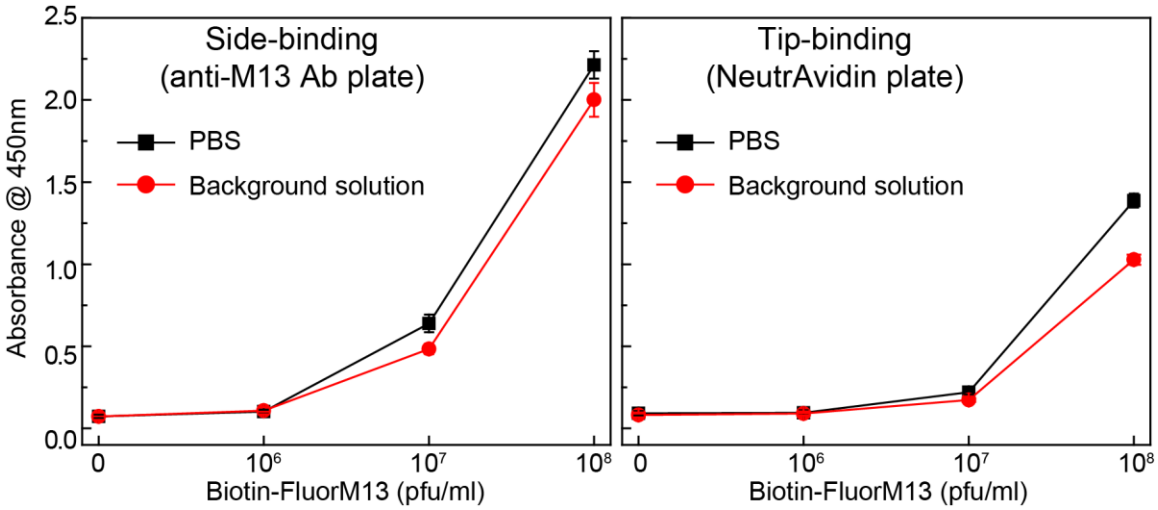

Figure 3.4 Difference of binding efficiency for Biotin-FluorM13 between in presence of the PBS or the glycerol and the partially-hydrolyzed poly(acrylamide) (HPAM).

The position of the solution interface x in the LFA membrane scales as the square root of time t, as expected from Washburn's equation[108] ($x^2 = \gamma dt/4\eta$, where γ is the surface tension of the liquid, d is a characteristic pore diameter, and η is the dynamic viscosity) and shown in Figure 3.5a. This result indicates that capillary pressure is sufficient to drive flow of the fluid through the membrane, as in a traditional LFA. Subsequently we image phage as they flow through the membrane at a fixed position (x = 1 cm, y = 10 μm, z = 1 mm) downstream from the imbibition pad and initially measure their local maximum velocity as a function of time. The local maximum velocity is highest at the very start of the experiment (immediately after fluid breakthrough) and first rapidly then slowly decreases with time, as shown in Figure 3.5b. Although the maximum velocity steadily decreases with time, the local flow profile can exhibit significant spatiotemporal variations (inset to Figure 3.5b).

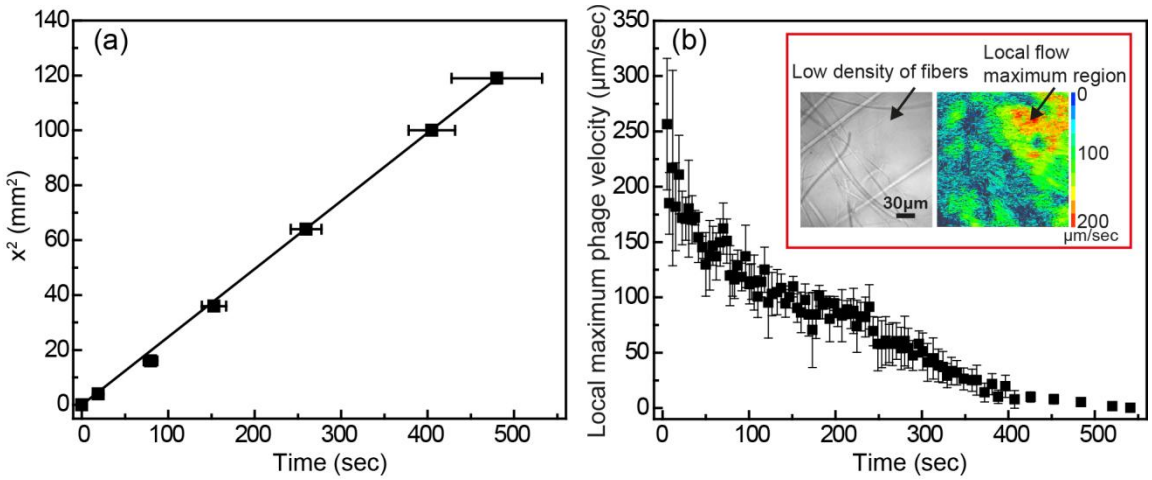

Figure 3.5 Flow characteristics of Biotin-FluorM13 solutions in Fusion 5 membranes.

The Fusion 5 membranes used in our model LFA have an open pore structure, and the local velocity of flow depends on the proximity and position of the fibers. Given the open pore network, we estimate the Reynolds number as $\mathrm{Re} = \rho DV/\mu$, where ρ is the background solution density, *D* is the average fiber diameter, *V* is the phage velocity, and μ is the solution viscosity. The maximum velocity of phages is 252 μm s^{-1} and hence the maximum Re is approximately 6.80×10^{-5}. Although the Reynolds number is low the complex fiber geometry generates curved streamlines, on which phage flow around the fibers. The maximum Péclet number of the flow, estimated from $\mathrm{Pe} = VD/D_p$, where D_p = 0.23 μm^2 s^{-1} is the measured translational diffusivity of the Biotin-FluorM13 (Figure 3.6 [We calculate the two-dimensional ensemble-averaged mean-squared displacement (MSD) of biotinylated Fluor-M13 in a quiescent background solution (30 v/v % glycerol and 0.2 w/v % HPAM in PBS). The Fusion 5 membrane is filled with 10^7 pfu/ml phage sample, covered with a coverslip, and sealed with ultraviolet-curing epoxy. Phage undergoing Brownian diffusion are tracked using the particle tracking algorithm. The translational diffusion coefficient (D_p =2.36 × 10^{-1} μm^2/sec) is calculated from the slope

of the linear relationship between MSD and lag time, i.e. $\langle \Delta r^2(\Delta t) \rangle = 4D_p \Delta t]$), is 4.8×10^3; advective transport dominates until the latest stages of imbibition.

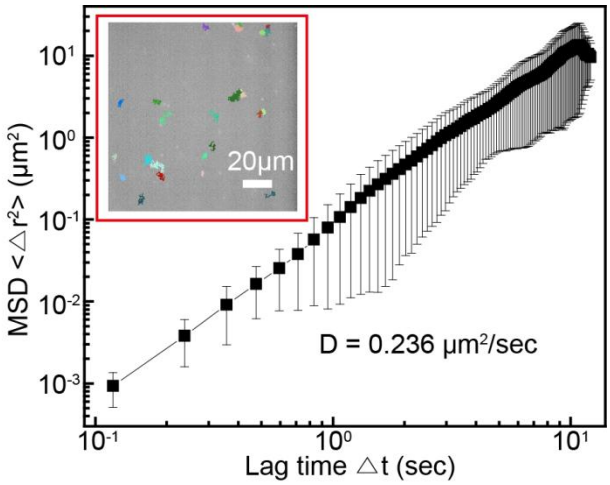

Figure 3.6 Diffusivity of Biotin-FluorM13 in Fusion 5 membrane.

Classification of phage binding mechanisms. We image phage as they bind to the functionalized Fusion 5 membranes and use the motion of phage relative to the membrane prior to binding to classify each binding event into one of four modes: wetting, collisional, helical, or sliding (Figure 3.7 [Biotinylated FluorM13 bind to functionalized fibers in four different modes. (1) "Wetting" binding occurs only during the initial imbibition of fluid into the membrane, during which thin liquid films form along the fibers. Only phage trapped between the fiber and the liquid/air interface are deemed to be using this mode. (2) Phage that bind immediately after encountering the fiber are deemed to use the "collisional" mode. Alternately, phage that do not immediately bind are transported along the fiber prior to binding by the "helical" or "sliding" mode. (3) In the "helical" mode, phage move in curved trajectories over the fiber interface prior to binding. (4) Conversely, in "sliding" mode phage move in nearly linear trajectories along the fiber prior to binding and are oriented parallel to the fiber axis. A decision chart for classifying

binding modes is given in Figure 3.8]). First, immediately after fluid breakthrough a thin film of fluid wets each fiber; phage entrained in this thin liquid layer align preferentially along the fiber and eventually (but not typically immediately) are captured by the recognition agents thereon. This mode, which we label "wetting," occurs only when the solution/air interface is still visible, in the early stage of imbibition. After the strip is fully wetted, we identify three subsequent modes by which phage bind to the membrane. Second, some phage immediately bind to a membrane fiber within a single time step (within 0.04 s) of encountering the fiber and do not travel along it; we term this mode "collisional." In the remaining two modes, phage orient along the fiber surface and move a finite distance along the fiber prior to irreversibly binding. Here, they move along the fiber for N = 3 to 30 time steps (0.1 – 1 s), depending on the flow speed; we classify binding as one of two distinct modes based on the shape of the path traced out by the phage along the fiber. Phage binding using the third "helical" mode follow curved trajectories with respect to the fiber axis. Phage binding through the fourth "sliding" mode follow straight trajectories. Quantitatively, it is convenient to use the angle between the phage body and the fiber axis to distinguish these modes: less than 1° for sliding, greater than 1° for helical. A decision chart for classifying binding modes is given in the Figure 3.8.

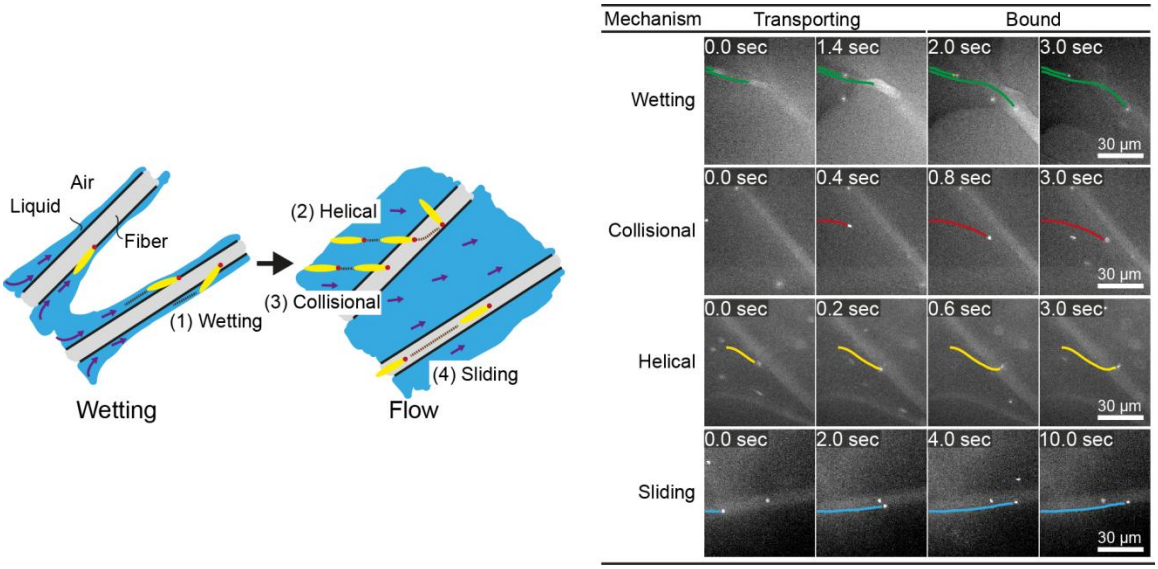

Figure 3.7 Observed FluorM13 binding modes.

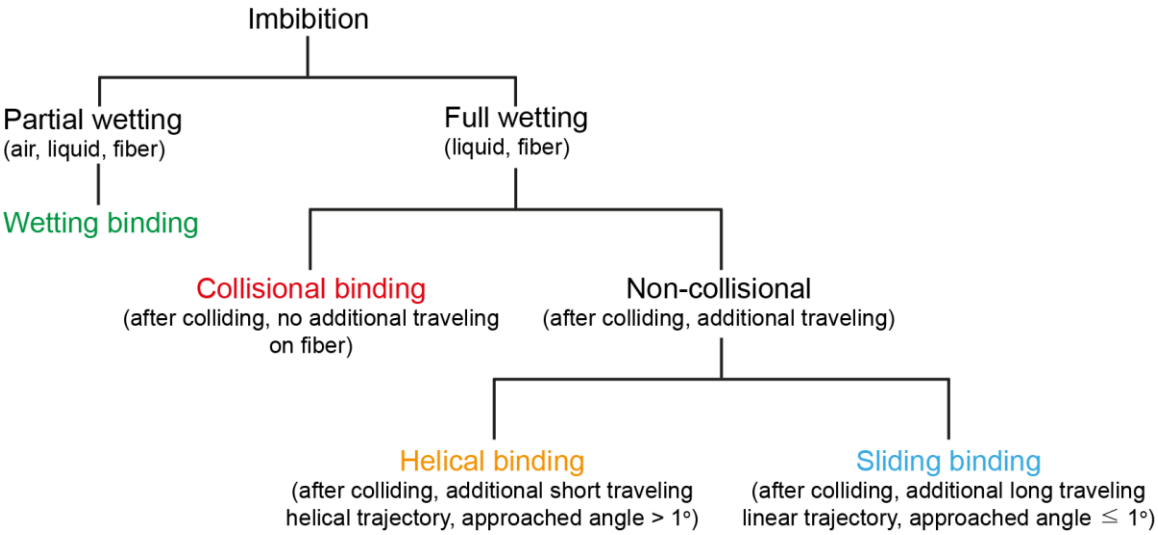

Figure 3.8 Decision chart for classifying binding modes.

Phage captured by anti-M13 antibodies (predominantly side-bound) and by NeutrAvidin (tip-bound) exhibit differences in the distribution of the modes by which they bind to functionalized LFA membranes. Over seventy percent of side-bound phage (total number of binding events N = 356) bind immediately after colliding with a membrane fiber (Figure 3.9a). In this case the antibodies on the fiber are able to capture

phages that are oriented in all directions with respect to the fiber axis, and so the majority of phage do not have to precisely align with the fiber to bind. Nonetheless, one-third of the phage bind after transport along the fiber; filamentous phage have a larger effective capture surface area (relative to a sphere of the same volume) and hence are more likely to be captured before advecting away.

Tip-bound phage, by contrast, exhibit a more uniform distribution of binding modes. Only N = 101 phage in total are observed to bind across all movies, consistent with a lower binding efficiency of tip-binding, and only forty percent of tip-bound phage use the collisional mode (Figure 3.9b). We note that the affinity constant of the BiotinNeutrAvidin bond ($10^{15}\,M^{-1}$)[109] and the association rate constant ($k_{on} = 7.5 \times 10^7$) are much greater than those for a typical antibody-antigen pair ($10^8\,M^{-1}$, $k_{on} \sim 10^4 - 10^6$), even after accounting for the greater number of binding sites for the antibody (~2,700 per phage) than for the NeutrAvidin (1 to 5 per phage). The lower binding efficiency of tip-binding phage despite the higher binding affinity and association constant suggest that tip-binding phage are unlikely to be properly oriented for binding during flow; even if phage are transported along a streamline and collide with the fiber surface, only approximately half will have the Biotinfunctionalized tail correctly oriented to bind upon collision.[110] Instead, wetting (early in imbibition), helical, and sliding modes are more common for tip-binding than for side-binding. In these modes phage align along the fiber prior to binding, increasing their residence time near the fiber; both reorientation and the long residence time increase the likelihood that the biotin recognition element successfully encounters a NeutrAvidin on the fiber before the phage is advected away from the fiber surface.

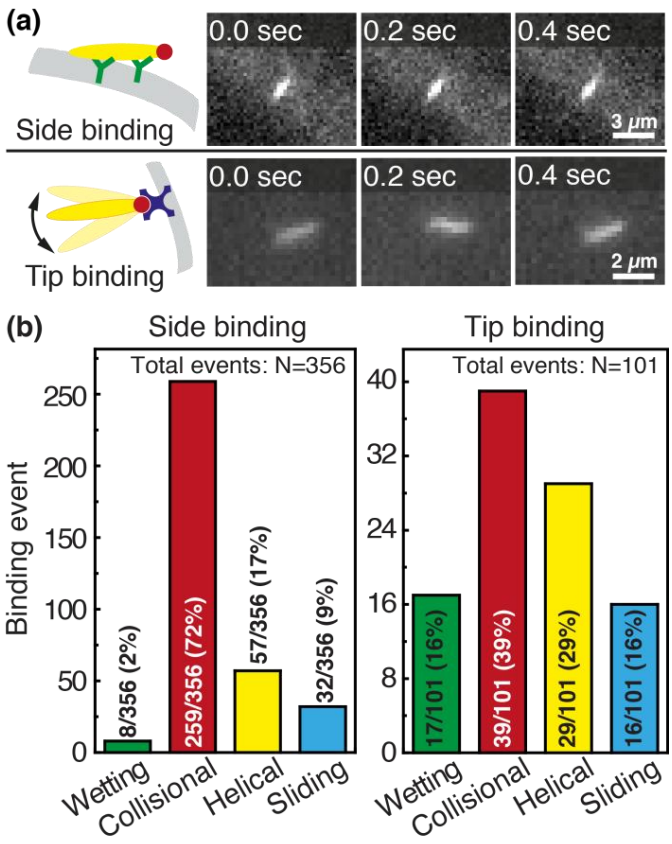

Figure 3.9 Comparison of side-binding and tip-binding modes.

We first characterize each binding mode by the relative (2-D projected) angle at which the phage body is oriented with respect to the fiber axis as it attaches. For side-binding (capture via anti-M13 antibodies), phage binding via collision preferentially orient at high angles with respect to the fiber axis but exhibit a broad distribution across all angles (Figure 3.10b). Phage binding via the helical mode preferentially bind at low angles, but with a broad distribution. Wetting and sliding entrain the phage along the fiber and hence phage binding in these modes are oriented along the fiber axis.

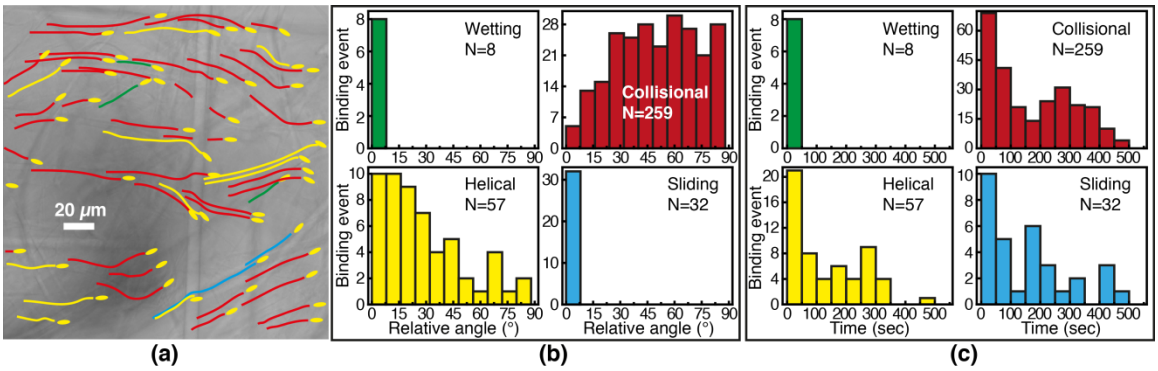

Figure 3.10 Relative angle and time for side binding.

The timing of binding events after the arrival of the fluid meniscus also depends on binding mode. All wetting binding events occur right after breakthrough, when the liquid-air interface is still present (Figure 3.10c). In the other modes, most phage also bind early (i.e. within 100 seconds of breakthrough), when the flux of phage is highest per the velocity measurements in Figure 3.5b. (Indeed the binding time distribution is correlated with the velocity, as shown in Figure 3.11. The number of unbound phage is nearly constant across at all times, as shown in Figure 3.12, and hence higher velocity likely increases the rate at which phage encounter fibers.) For example, collisional and helical binding events preferentially occur at shorter times after breakthrough; nonetheless, collisional, helical, and sliding binding events occasionally occur even at the longest accessible time scales, for which the advection velocity is nearly zero. Both the high likelihood of binding through collision and the wide distribution of binding angles are consistent with the omnidirectional capture of phage by anti-M13 antibodies on the membrane fibers.

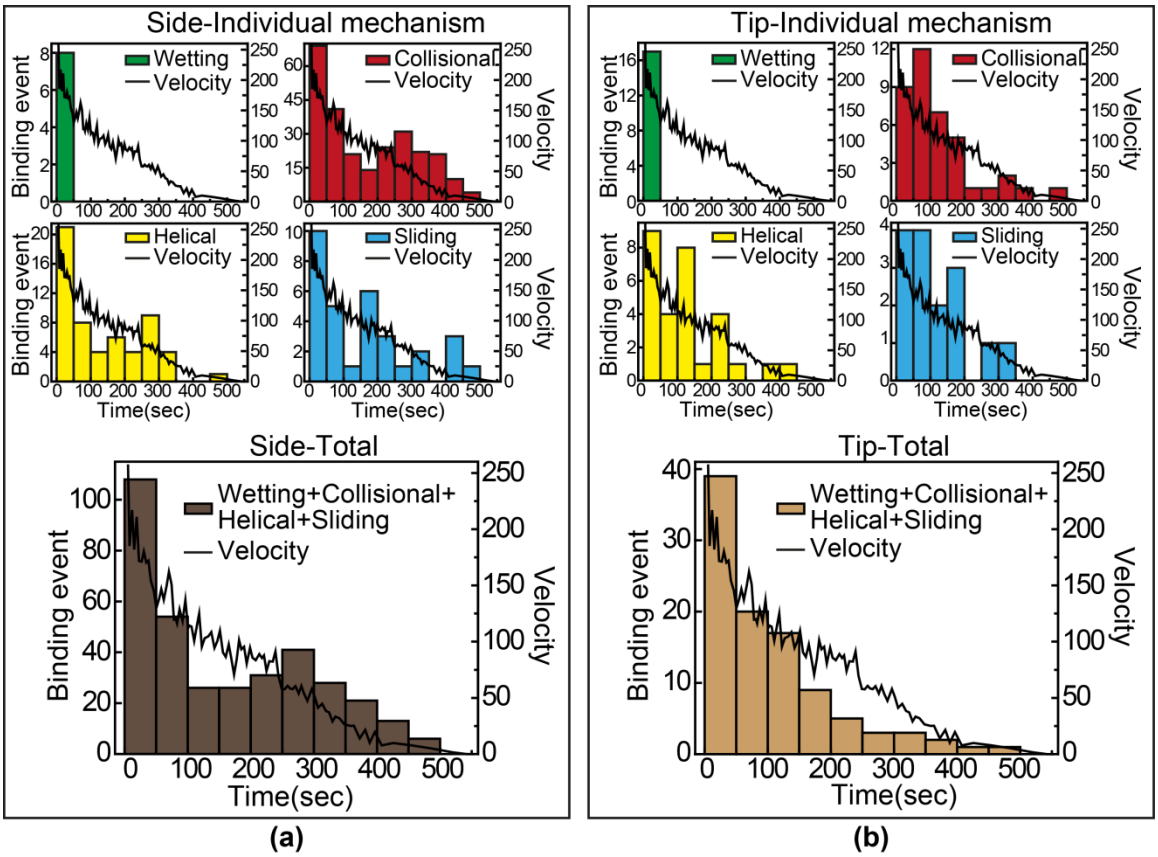

Figure 3.11 Comparison of the binding time distributions and the local maximum velocity.

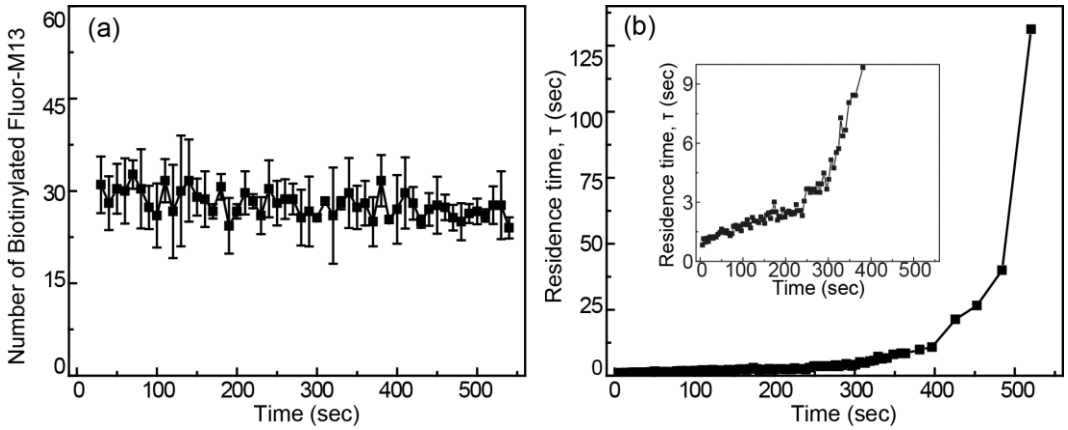

Figure 3.12 Number of unbound phage in the field of view (212.5 μm × 213 μm) as a function of time.

Phage binding to a NeutrAvidin-functionalized membrane, by contrast, must properly orient the biotin group to be captured by one of the NeutrAvidin proteins on the

fiber surface. This requirement is a more stringent condition on the orientation of the phage with respect to the fiber axis. As a result, fewer phage are able to immediately bind upon reaching the fiber surface. Indeed, phage that bind in collision are all oriented at a high angle (Figure 3.13b) so that the biotin functionality encounters the NeutrAvidin binding sites. Phage that are not properly oriented are less likely to bind but can nonetheless bind after reorientation. Notably, phage that arrive at the surface oriented at a low angle (< 30°) only bind if they are able to reorient and align along the fiber axis (i.e. in helical or sliding modes) or if they are forced to reorient by the presence of the fluid interface (i.e. in wetting, early after breakthrough). Phage that do not reorient instead slide over the fibers and are transported further into the membrane. Most tip-binding events, as in side-binding, occur early during the fluid flow (Figure 3.13c), consistent with the higher phage flux during the transient flow on those time scales.

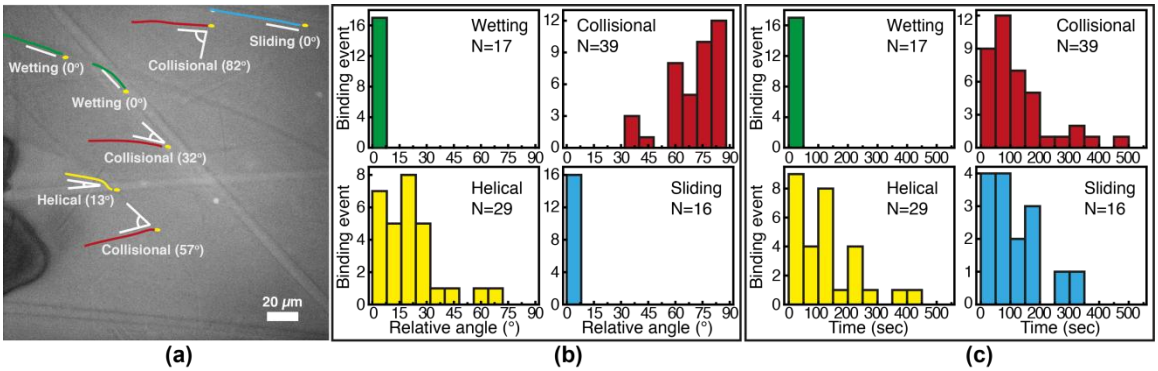

Figure 3.13 Relative angle and time for tip binding events.

Role of tumbling in binding. Coupling between the flow field within the porous membrane and the phage shape promotes reorientation for binding through other mechanisms not described by the four modes above. Figure 3.14 illustrates one example, in which a phage tumbles end-over-end prior to capture on the fiber. The physics

underlying tumbling is straightforward: M13 phage are elongated. Close to the surface of a fiber, no-slip boundary conditions hold; far from the fiber surface, fluid flows rapidly through the open pore network. This geometry generates a gradient of increasing flow speed farther from the surface of the fiber. A phage encountering a fiber at a nonzero angle hence is rotated by the vorticity field to align parallel to the fiber; for Biotinconjugated phage whose binding group is located far from the fiber surface, this rotation would bring the binding group closer to the fiber surface. Hence we expect near-fiber tumbling (at low Re) to enhance the binding of anisotropically-shaped particles by increasing the effective cross-section for capture, relative to that of a sphere of the same volume. Similar arguments regarding capture cross-section have been used to explain the increase of non-specific binding of low-aspect-ratio ellipsoidal nanoparticles in dense packed beds.[111]

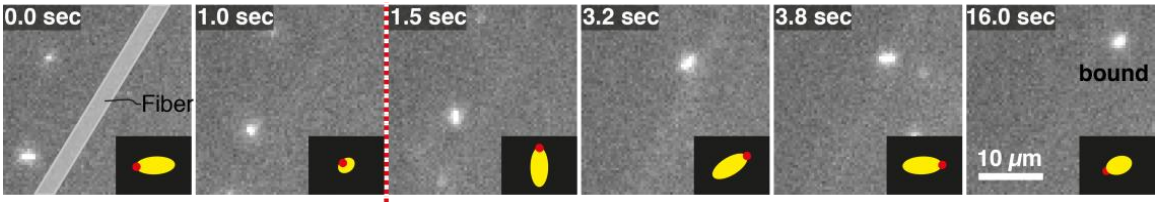

Figure 3.14 Reorientation of Biotin-FluorM13 by tumbling for tip binding.

To illustrate the role of local flow fields on particle reorientation, we use a simplified COMSOL model of a shear-thinning non-Newtonian fluid flowing around two fibers. As in the experimental membrane, the local flow velocity depends on proximity and position of the fibers (Figure 3.15) and streamlines diverge around the fiber surface. Across a range of flow rates, the vorticity is highest near the fiber surface (Figure 3.15a, b); moreover, because the streamlines typically encounter the fibers at an angle they distort to flow along the fibers. The bending of streamlines along the fibers is similar to

the bending of phage trajectories near the fiber observed in the experiments (c.f. Figures 3.7, 3.10a, 3.13a). These flow features are expected to promote reorientation of anisotropic phage along the fiber axis. We note that this reorientation does not depend on the non-Newtonian character of the solutions; similar flow fields are obtained for a COMSOL simulation of Newtonian water (Figure 3.15c, d). In the additional experiments with varying in the viscosity of the solution, we also have similar results, such as binding number, binding modes and the relative angles (Figure 3.16—3.20). Although this model neglects most of the geometric complexity of the experimental system, it nonetheless suggests that the local flow can promote reorientation of filamentous M13 bacteriophage along the fiber axis, providing one route to increase binding and capture in the open porous Fusion 5 membrane. In a highly porous membrane such as Fusion 5, the diverging streamlines around the fibers reorient phage to promote attachment; in contrast, in dense porous media the converging streamlines in a pore instead transport anisotropic particles towards the pore center and hence have been reported to reduce (non-specific) binding.[112]

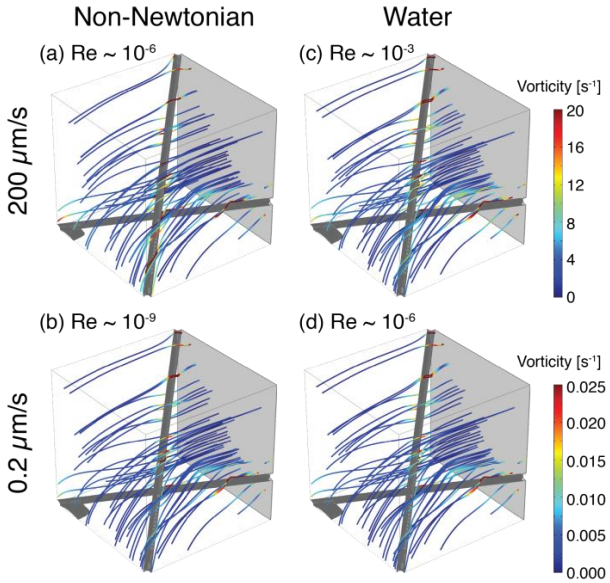

Figure 3.15 Example streamlines from COMSOL simulations of fluid flow around two fibers.

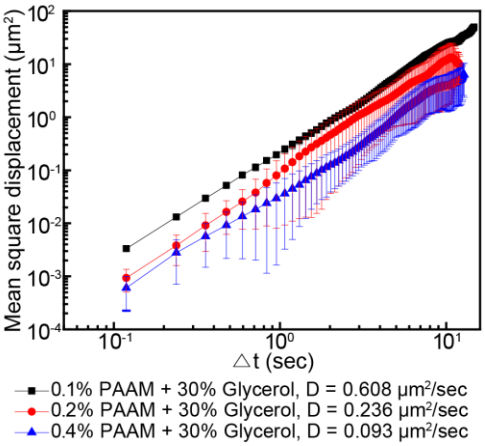

Figure 3.16 Diffusivity of Biotin-FluorM13 in Fusion 5 membrane with varying in the HPAM concentrations.

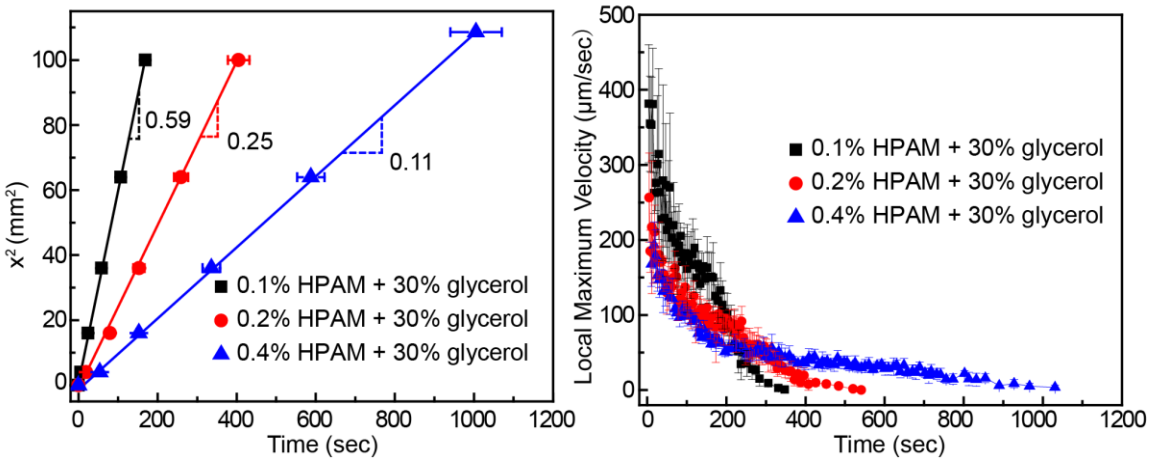

Figure 3.17 Flow characteristics of Biotin-FluorM13 solutions in Fusion 5 membranes with varying in the HPAM concentrations.

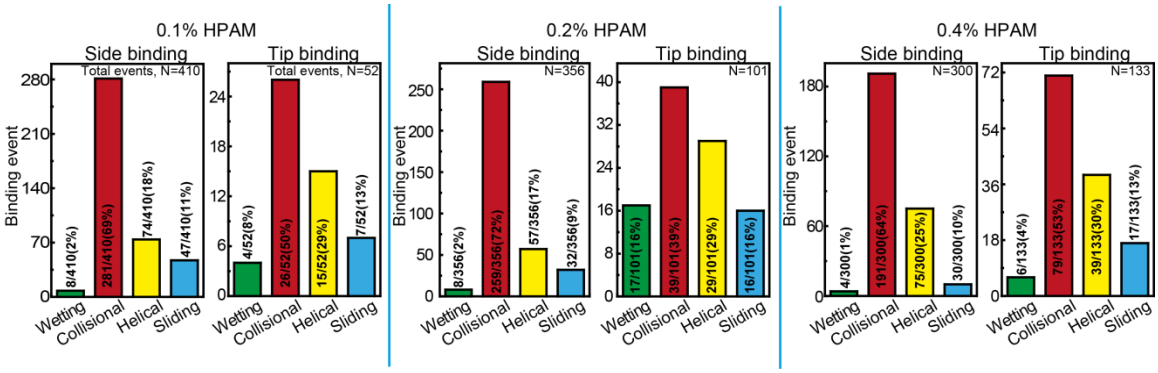

Figure 3.18 Comparison of side-binding and tip-binding modes at different viscous solution by varying in the HPAM concentrations.

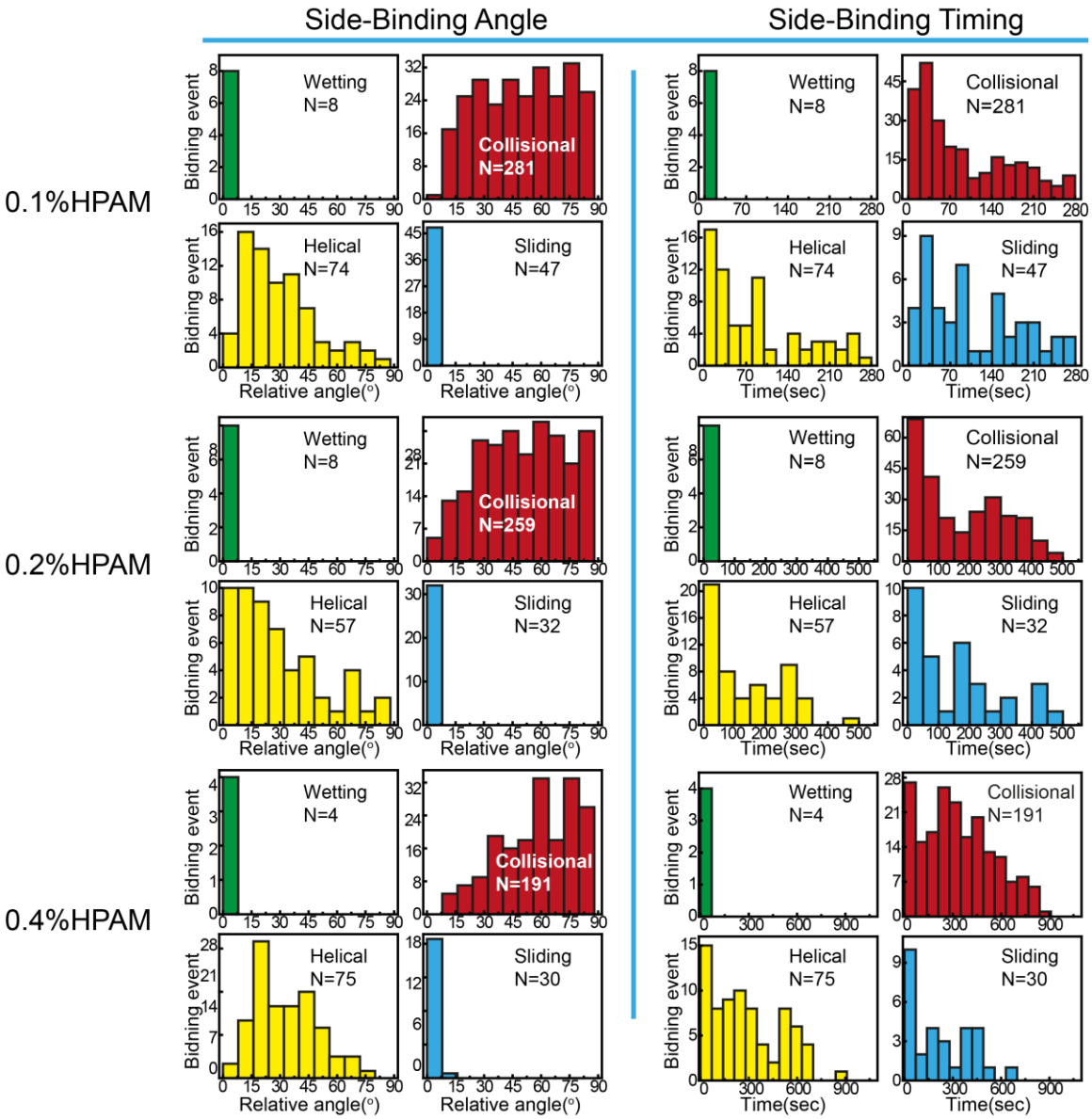

Figure 3.19 Relative angle and time for side binding with varying in the HPAM concentrations.

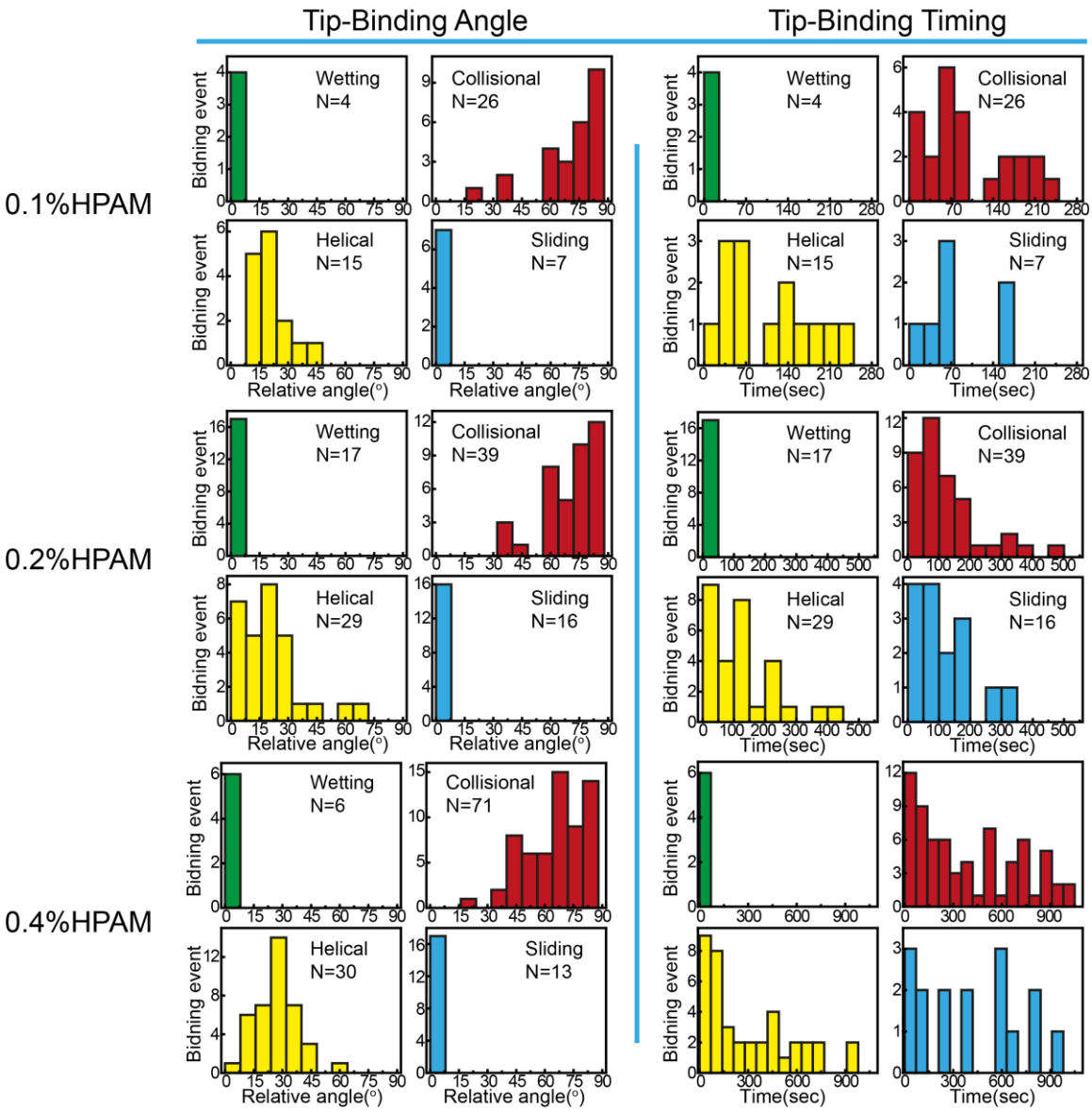

Figure 3.20 Relative angle and time for tip binding with varying in the HPAM concentrations.

3.4 Conclusions

We characterized the binding modes of elongated viral nanoparticles to functionalized open-porous membranes at the pore scale using a model LFA. M13 bacteriophage captured by anti-M13 antibodies on the membrane preferentially bind immediately after colliding with a fiber, and do so regardless of their orientation with respect to it. By contrast, a large fraction of the phage captured by a Biotin and

NeutrAvidin interaction at their tip bind only after reorienting and transporting along the fiber axis. Our results are consistent with (though not proof positive of) the idea that the anisotropic phage shape may promote binding of phage used as reporters in lateral-flow immunoassays by two mechanisms: by increasing the capture cross-section and by reorienting in flow to increase capture likelihood. This idea may explain part of the increase in sensitivity of the viral-nanoparticle LFAs compared to traditional gold-nanoparticle-based LFAs, which employ spherical or nearly-spherical reporters that cannot rotate to increase the likelihood of capture.

Beyond the specific application to phage-reporter LFAs explored here, we expect that the coupling between reporter shape and binding in a random open porous membrane may inspire new routes towards the design of improved or sensitive LFAs. First, the idea that anisotropic reporters promote binding can be extended to inorganic/abiotic nanoparticles. The excellent control afforded by modern synthetic methods (e.g. for gold nanoparticles, which can be synthesized in a variety of anisotropic morphologies[113]) would enable systematic studies of the role of particle shape on transport and capture towards identification of design rules for reporters. Second, our results suggest that the orientation of fibers relative to the local flow direction modifies the local vorticity, which in turn generates tumbling near the fiber and increases the likelihood that phage reorient along the fiber. It is thus possible that modifying (in, for example, paper membranes[114]) either the strip architecture[115] or the fiber orientation may increase capture of anisotropic particles and hence also improve LFA sensitivity. These ideas arise in the context of the relatively open LFA membranes studied here. As the characteristic pore size of the membrane is decreased, additional coupling between flow and particle shape may lead to

other nanoparticle orientations[116] that, in turn, could promote reporter capture and hence increase LFA sensitivity. More broadly, the methods established here to probe the effects of particle anisotropy on capture and binding at the pore-scale may prove useful towards optimizing particle capture in a variety of microscale open porous media, with relevance for applications in on-chip chromatography, virus purification, membrane chromatography, and in microfluidic nanocomposite fabrication.

Chapter 4. Effect of phage length on binding to LFA membranes

4.1 Introduction

Point-of-care (PoC) devices are used for medical testing at or near the site of patient care.[6] One of the PoC tests that are the most widely used and commercially available is the lateral flow immunoassays (LFAs) due to its low cost, simple assay operation, ease of mass production, and good specificity.[7] The widespread use of the LFAs, however, remains limited by two main issues: lack of sensitivity and difficulties in quantification.[117] More sensitive LFAs would expand the potential set of applications, including for pathogen monitoring in food and in biopharmaceutical manufacturing.[14] To improve sensitivity of LFAs, we can consider three strategies by developing (1) new LFA reaction membranes,[115, 118] (2) new reporter materials,[119, 120] and/or (3) new read-out methods.[121, 93]

The reaction membrane, in which analytes and reporters bind to generate readable signals, is one of the most important components of LFAs. The optimal binding of specific analytes and reporters within the membrane maximizes read-out signals, thereby enhancing detection limits. Currently, the newly developed sensitive LFAs were optimized empirically for better binding efficiency and assay performance by tuning a variety of operating parameters, including fluid velocity[118], concentration[122] and size [123] of reporters. Despite significant experimental efforts, few existing studies investigate the influence of these assay parameters affect the binding efficiency. Systematic studies of these parameters are expected to suggest practical insights towards improving LFA sensitivity.

Here, we addressed the effect of reporter length and fluid flow on the binding of reporters in a fibrous glass membrane. In Chater 3, we reported that the flow field within the Fusion 5 membrane coupled to the phage shape promotes reorientation for binding, and postulated the binding efficiency can be increasing by tuning the size and shape of the phage. To test this postulate, we used three different sizes of filamentous phage (PVM, length 0.2 μm, M13, 0.9 μm, and Pf1, 2 μm) in a simplified LFA. Phage were functionalized with biotin and AlexaFluor 555 on their major coat proteins. Through these experiments, we identified two mechanisms that increased the number of bound phage in the NeutrAvidin-treated Fusion 5. First, the number of bound phage increased as the phage length or surface area increased. Second, the number of bound phage also depended on the bulk flux, which in turn depended on the concentration of phage or the flow rate. Both the phage length and the high flux increase the likelihood that phage encountered a fiber. For example, phage predominantly bound at the beginning of flow, when the bulk flow rate was fastest. Nonetheless, there was significant spatiotemporal variation in the flow rate across the membrane. To test whether binding properties were primarily determined by bulk or local flow properties, we examined the effect of local flow rate on the binding efficiency of phage. We found that phage were more likely to bind in regions of the membrane featuring faster-than-average flows, again consistent with the idea that higher flux increased the encounter probability to fibers. Finally, we examined the directionality of binding. Bound phage did not show a particular preferred orientation for binding, indicating that the angle at which phage approached fibers did not alter binding efficiency. Here, the large number of biotins attached to the phage major coat protein enabled multivalent binding and minimized any orientational dependence.

Our experimental results suggest that reporter length and flux are tunable parameters that can be used to influence the binding efficiency in model LFAs and should be considered as design parameters.

4.2 Materials and Method

Biotinylation of phage. Wilde type filamentous Pf1 bacteriophage (Pf1) (ASLA Biotech), potato virus M virus-like particles (PVM) (ASLA Biotech), and M13 bacteriophage (M13) (ATCC, #34768) were modified with biotins (EZ-Link® Sulfo-NHS-LC-Biotin, ThermoFisher Scientific, #21327) as illustrated in Figure 4.1. The amine reactive biotinylation reagent was conjugated to the primary amines of the p8 major coat proteins of phage, according to the manufacturer's instructions (ThermoFisher Scientific, #21327). We offered 100-fold molar excess of biotin reagent to label ~10^{10} phage. A 7K MWCO Zeba spin desalting column (Thermo Scientific #89877) was used to remove excess biotin.

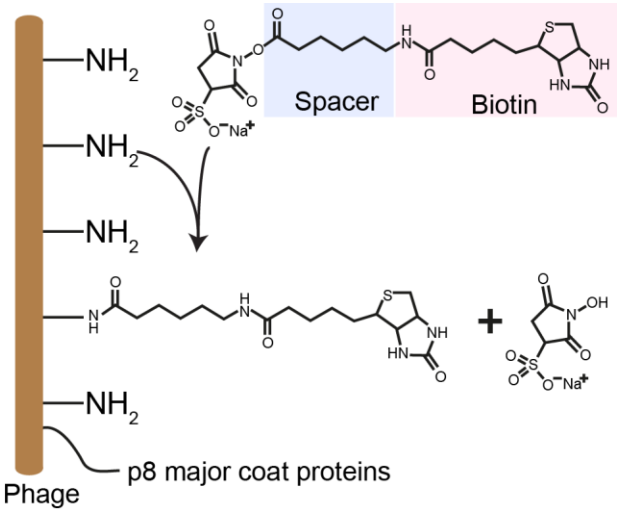

Figure 4.1 Functionalization of phage with biotins on p8 major coat proteins.

AlexaFluor 555 labeling of phage (Fluor-phage). Biotinylated phage, including Pf1, PVM and M13 were further modified with AlexaFluor 555 Carboxylic Acid

(Succinimidyl Ester, Life Technologies #A-20009) as previously described.[124] Biotinylated Fluor-phage were detectable by epi-fluorescence microscopy and capturable by NeutrAvidin (Figure 4.2).

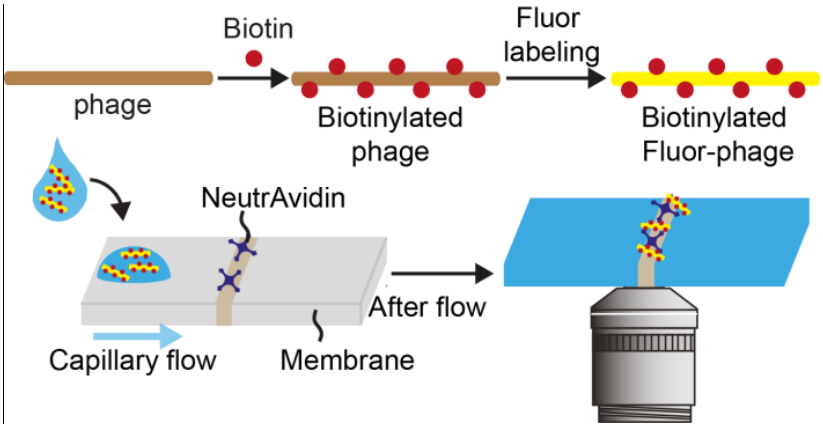

Figure 4.2 Schematic of phage modification and capture.

Validation of biotinylation of Fluor-phage using enzyme-linked immunosorbent assay (ELISA). The biotinylation of Fluor-phage was evaluated using TMB (3,3',5,5'-Tetramethylbenzidine)-ELISA. 100 µl of biotinylated Fluor-phage at concentrations of 0, 10^6, 10^7, 10^8 and 10^9 pfu/mL in 2% (w/v) BSA were added to NeutrAvidin-coated 96-well plates (Pierce Reacti-bind 96-well plates, Thermo Scientific #15128). After a 2 h incubation at room temperature, the plate was washed and rinsed four times each with PBST (PBS containing 0.05% (v/v) Tween 20) and PBS, respectively. Next, bound biotinylated Fluor-phage were allowed to react with 100 µl of horseradish peroxidase (HRP)-conjugated StreptAvidin (1:5,000 dilution, ThermoFisher Scientific, #N100) for 1 h at room temperature, followed by washing and rinsing. 50 µl of TMB was added to the plate to develop the color for 15 min, and the reaction was terminated by adding 50 µl of 2 N H_2SO_4. Absorbance was measured at 450 nm in an ELISA reader (Tecan, Infinite

M200 PRO). As a control experiment, we also performed an ELISA test for non-biotinylated Fluor-phage on NeutrAvidin-coated 96-well microplates.

Flow experiments. Fusion 5 LFA matrix strips (3 mm × 50 mm × 0.35 mm, GE Healthcare & Life Sciences #8151−9915, pore diameter 11 μm [reported by manufacturer], average fiber diameter D = 4.35 ± 1.90 μm [measured]) were modified with 3 μl of 1 mg ml^{-1} NeutrAvidin (Thermo Scientific, #3100) in 50 mM acetate buffer at pH 4.0 by hand spotting at a fixed distance of 1 cm from the downstream end of the strip. After drying in air for 2 h at room temperature, each functionalized strip was placed on a large coverslip (48 × 65 mm, Gold Seal), covered with a second smaller coverslip (22 × 22 mm, Fisher Brand), and moved onto the stage of an epi-fluorescence microscope (Leica DMI 3000B) equipped with a 63× oil immersion objective lens (NA 1.4), as shown in Figure 4.3. For the model LFA experiments, biotinylated Fluor-phage were suspended in a background solution containing 0.1 w/v % hydrolyzed polyacrylamide (HPAM, FLOPAAM 3330, SNF, weight-averaged molecular weight of 8 MDa) and 30% v/v glycerol in PBST (PBS containing 0.01% (v/v) Tween 20) to increase the viscosity of the solution and reduce the local flow speed for imaging. Subsequently, 25 μl of 2-fold serially diluted phage at concentrations of $\frac{1}{32} \times 10^8$, $\frac{1}{16} \times 10^8$, $\frac{1}{8} \times 10^8$, $\frac{1}{4} \times 10^8$, and $\frac{1}{2} \times 10^8$ pfu ml^{-1} was dropped on the upstream end of the strip.

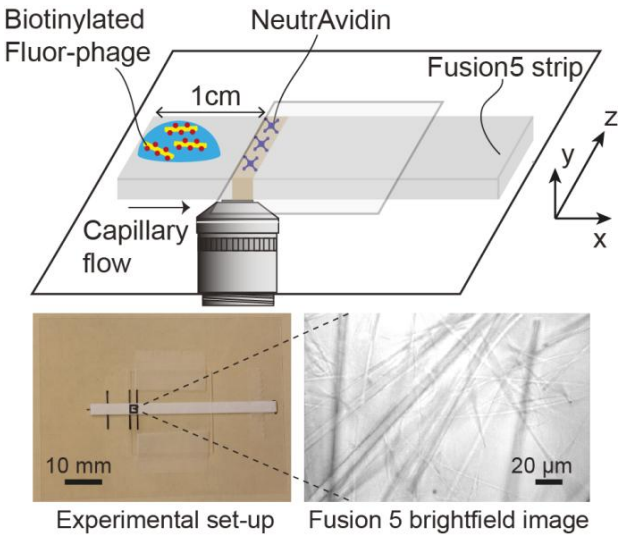

Figure 4.3 Schematic of the experimental setup.

Biotinylated Fluor-phage were imaged in capillary-driven transport through the membrane using a sCMOS camera (pco.edge 4.2, 30 frame/sec, 30 ms exposure time, 208 μm × 213 μm image field of view). Recording began immediately after liquid breakthrough in the field of view (set as 0 sec) and ceased when the phage particles exhibited only Brownian (rather than advective) motion, typically six minutes. Three movies were analyzed for each concentration of phage.

Counting of bound phage. In our flow experiments, phage bound to fibers over time, and accumulated in the images as static particles (Figure 4.4a). To locate and count the bound phage to the fibers in the movies, we manually analyzed nine three-second intervals in each of the three movies per different phage and concentrations (20 – 23 sec, 60 – 63 sec, 100 – 103 sec, 140 – 143 sec, 180 – 183 sec, 220 – 223 sec, 260 – 263 sec, 300 – 303 sec, and 340 – 343 sec). All bound phage in each movie were located manually; phage location in the phage shape was determined at the maximum pixel of brightness at the single pixel level (Figure 4.4b). The location of phage at maximum pixel was not significantly different from its centroid which was the averaged pixel indices by

weighting intensities (the error between maximum pixel and averaged pixel indices was sub-pixel level, such as (±0.29, ±0.25)).

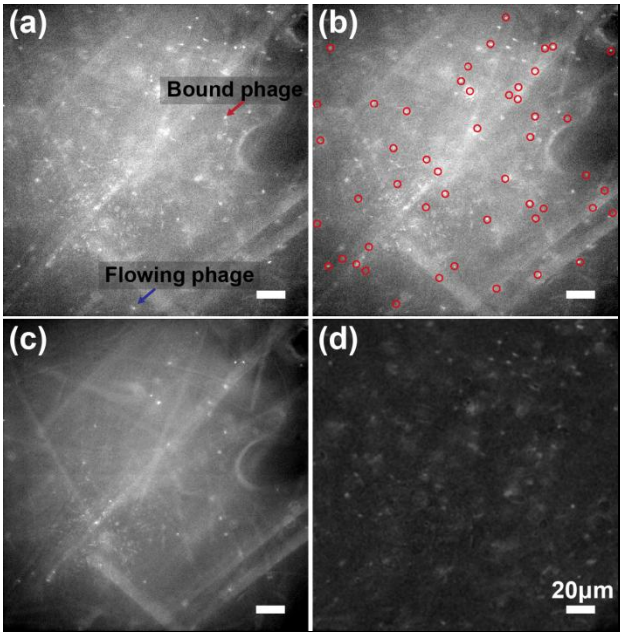

Figure 4.4 Bound phage counting and pre-image processing. (a) The original image of flowing and bound phage, (b) location of bound phage, (c) image of background, and (d) flowing phage

Pre-image processing for particle image velocimetry (PIV). We measured the local velocity at different positions in the image field of view using PIV. Prior to PIV analysis, images were processed to remove any static background that affected the PIV calculations. In particular, we found that phage bound to the membrane generated a static background signal that deleteriously affected the PIV processing. To remove bound phage from the image, we first created a background image (Figure 4.4c) from the three second interval movie (or image stack) using ImageJ software; the background image contained the minimum intensities at each pixel of the image stack. Then, the background was removed from the image stack via background subtraction (Figure 4.4d). The

background image (Figure 4.4c) showed bound phage at the same locations as in Figure 4.4b.

PIV Analysis. To obtain the flow velocity profiles, particle image velocimetry (PIV)[125] was performed on the images in three-second interval movies of a sample containing phage at a concentration of $\frac{1}{2} \times 10^8$ pfu ml^{-1}; a high density of phage was appropriate for PIV evaluation to improve statistical correlations and reduce error across the entire field of view of the image.[125] After pre-processing, we performed PIV[126](software downloaded from http://www.jpiv.vennemann-online.de/) using an interrogation window of 8 pixel × 8 pixel, a vector spacing of 3 pixel × 3 pixel, and a median filter of 3 pixel × 3 pixel. The four sequential images were correlated and averaged for PIV output at 20, 60, 100, 140, 180, 220, 260, 300, and 340 sec. The output of the PIV routines was the flow vectors at different pixel positions in the image. From the flow vectors, flow rates and directions were decoupled and represented as separated maps (Figure 4.5).

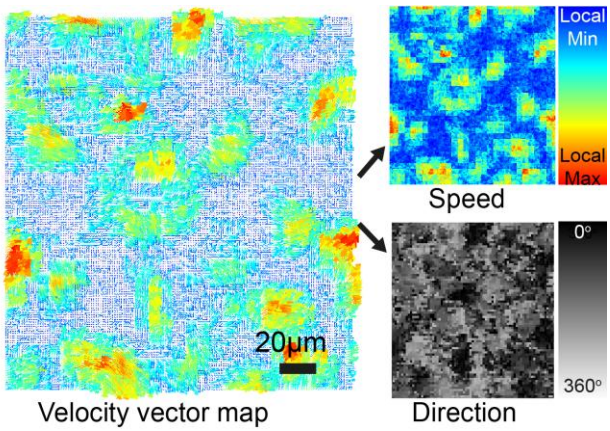

Figure 4.5 Particle image velocimetry (PIV) analysis.

Determination of flow direction on fiber surface. To image the fibers, a brightfield micrograph was acquired in the same focal area as the flow movie. Practically, it was difficult to segment the fiber features from background using image binarization, due to the variation of intensity and transparency of fibers (Figure 4.6a, left). Hence we conducted image binarization manually; fiber areas in the image were painted with black to generate extreme contrast, after which the threshold was applied to the painted image (Figure 4.6a, center). Some individual fibers so identified were overlapped and connected together at the intersection in the binary image. Fibers consisting of multiple segments in different directions were disassembled at the intersection. Next, to automatically obtain the fiber directions, each segment of fiber was labeled using connected component labeling (CCL). Next, an axis-aligned bonding box was applied to the labeled fibers. The orientation of fibers was calculated (in degrees, relative to the positive x-axis) from the length and width of the bounding box (Figure 4.6a, right). Finally, the flow direction obtained from the PIV analysis was correlated with the fiber orientation. The range of relative angles between flow and fiber varied from 0˚ (parallel) to 90˚ (vertical). Four different formulas were used to calculate the relative angle, depending on the angular ranges of the fiber angle (ϕ) and flow direction (θ) (Figure 4.6b).

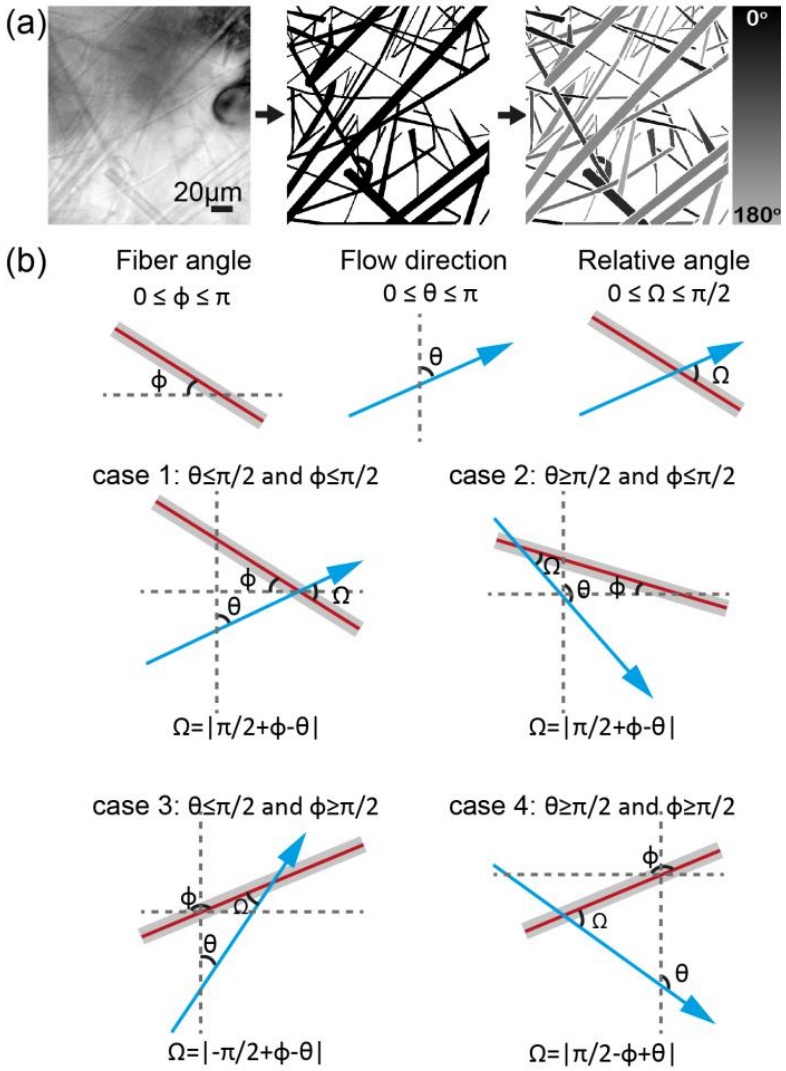

Figure 4.6 Image analysis to obtain relative angle between flow and fiber orientation.

Correlation of local flow with bound phage. The output from the PIV algorithms (Figure 4.7c) provided both the magnitude of the flow rate and the flow direction at each location within the image. The flow rate profile was extracted across the entire fiber area, and the specific local flow rates were obtained at the position where phage were bound (Figure 4.7d). Similarly, the specific flow directions, which were correlated to fiber orientation (Figure 4.6), were obtained at the position where phage were bound (Figure 4.7e).

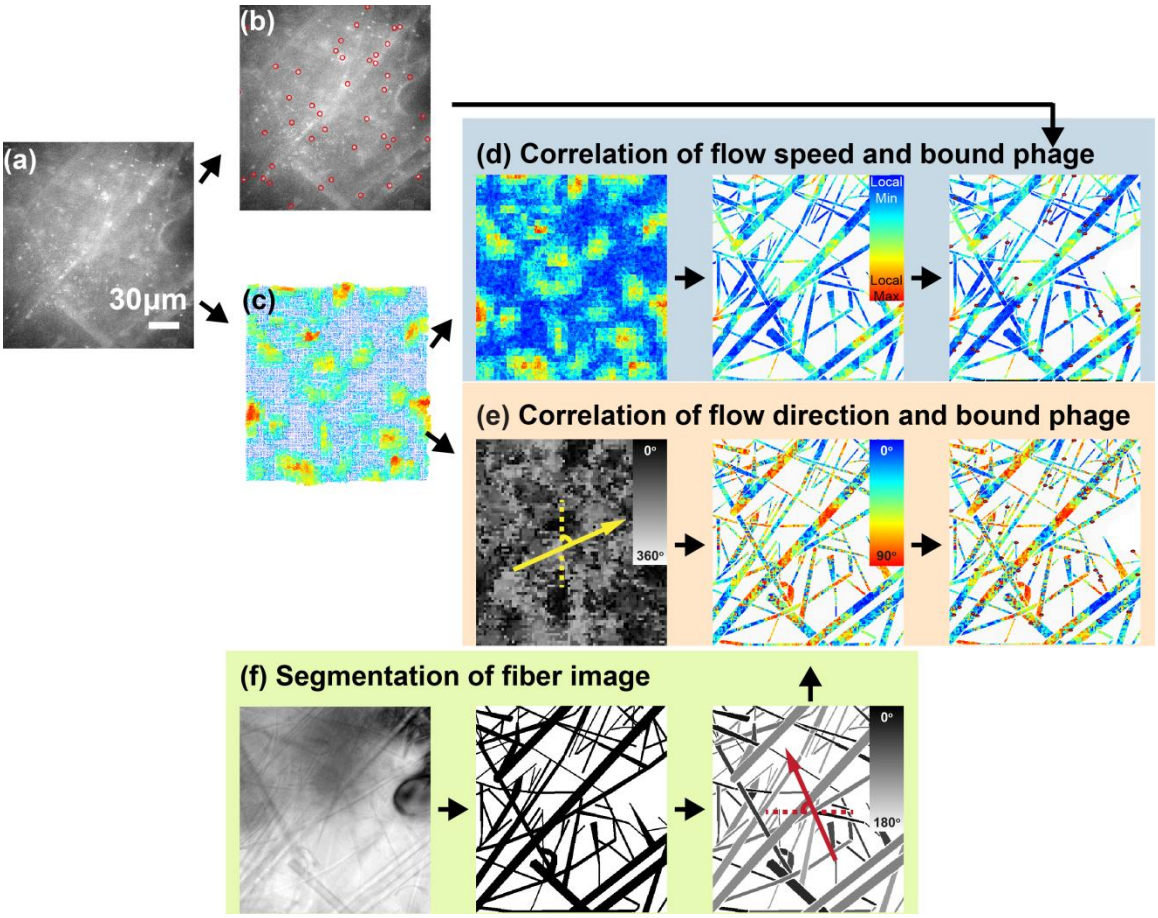

Figure 4.7 Correlation of local flow rates with bound phage.

4.3 Results and Discussion

Characterization of Biotinylated Fluor-phage. Three filamentous phage of different lengths (PVM, length 0.2 μm; M13, 0.9 μm; and Pf1, 2 μm) were functionalized with biotins and AlexaFluor 555. To confirm the success of the fluorescent labeling, we acquired fluorescence micrographs of the biotinylated Fluor-phage. Each phage type was readily visualized using fluorescence microscopy, as shown in the representative images in Figure 4.8. To verify that Fluor-phage retained biotins after biotinylation, we conducted ELISA assays on NeutrAvidin-coated plates. Biotinylated Fluor-phage exhibited positive ELISA outputs whereas non-biotinylated Fluor-M13 in the control experiment did not give ELISA signals on the NeutrAvidin coated-plate (Figure 4.9),

confirming that the biotinylated Fluor-phage were specifically bound to the NeutrAvidin-coated plate.

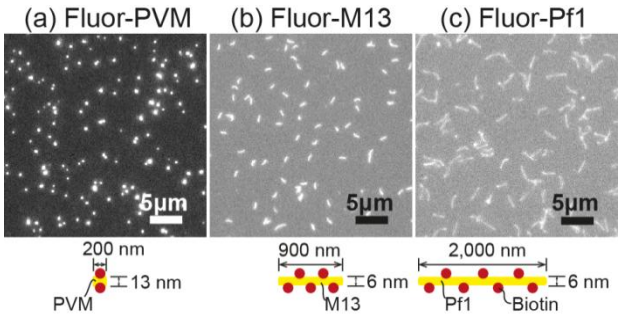

Figure 4.8 Representative micrographs of phage reporter series.

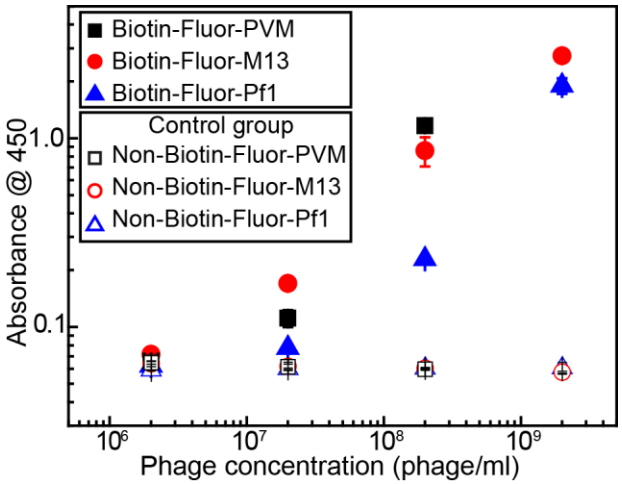

Figure 4.9 Conformation of biotinylation of phage using ELISA.

Comparison of number of bound phage PVM, M13 and Pf1 in LFA. To compare the binding efficiency of phage of different lengths in the Fusion 5 membrane, we counted the number of bound phage as a function of time and concentration ($\frac{1}{32} \times 10^8$, $\frac{1}{16} \times 10^8$, $\frac{1}{8} \times 10^8$, $\frac{1}{4} \times 10^8$, and $\frac{1}{2} \times 10^8$pfu ml^{-1}), as shown in Figure 4.10a – c for the PVM, M13, and Pf1 phage. The number of phage bound on the membrane increased with the concentration of phage and with time for each phage series.

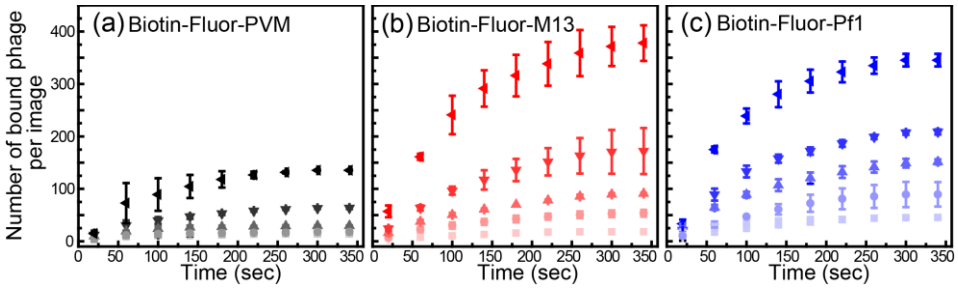

Figure 4.10 Bound phage counting results. (a) Biotin-Fluor-PVM, (b), Biotin-Fluor-M13, and (c) Biotin-Fluor-Pf1.

Phage predominantly bound early after breakthrough during flow. More than 50% of bound phage bound to fibers within 100 sec, before the bulk flow rate decreased by about 50% (Figure 4.11a). After the flow ceased, the phage exhibited Brownian motion from which their diffusivity can be calculated using mean square displacement (Figure 4.11b). Because the flow rate was related to phage flux, we counted flowing phage in the field of view at 20, 60, 100, 140, 180, 220, 260, 300, and 340 sec (Figure 4.12a, b, and c); the number of flowing phage was calculated by subtracting the total number of phage from bound phage in the image. The number of flowing phage was nearly constant in the membrane at all times (Figure 4.12a, b, and c); phage concentration was independent of time because the relatively large pore diameter (11 μm) did not preclude phage transport. The number of phage passing through the same field of view decreased over time (Figure 4.12d, e, and f), concomitant with decrease in the capillary flow rate shown in Figure 4.11. The rate at which phage bound to the network, calculated from the instantaneous derivative of the curves in Figure 4.10, was strongly correlated with the phage flux; a direct comparison is shown in Figure 4.13. The proportionality between binding rate and flux suggested that the binding reaction was promoted by increasing the chance that phage encounter fibers, and hence we attributed the greater number of bound phage to the higher flux of phage.

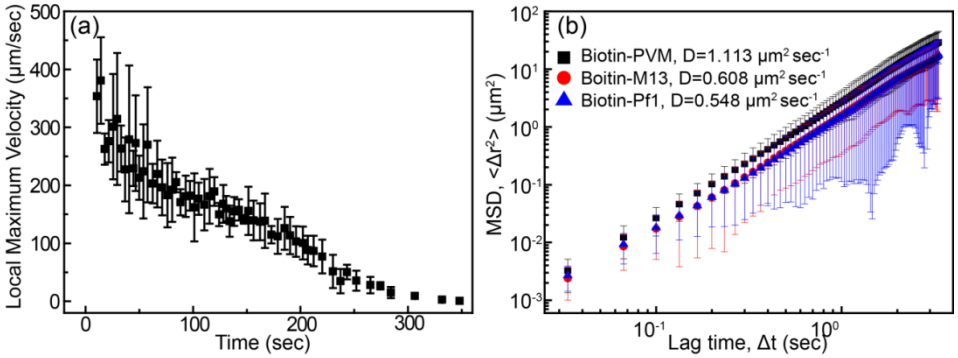

Figure 4.11 Flow characteristics of Biotin-FluorM13 solutions in Fusion 5 membranes.(a) Bulk flow rate, and (b) mean square displacement of phage in background solution.

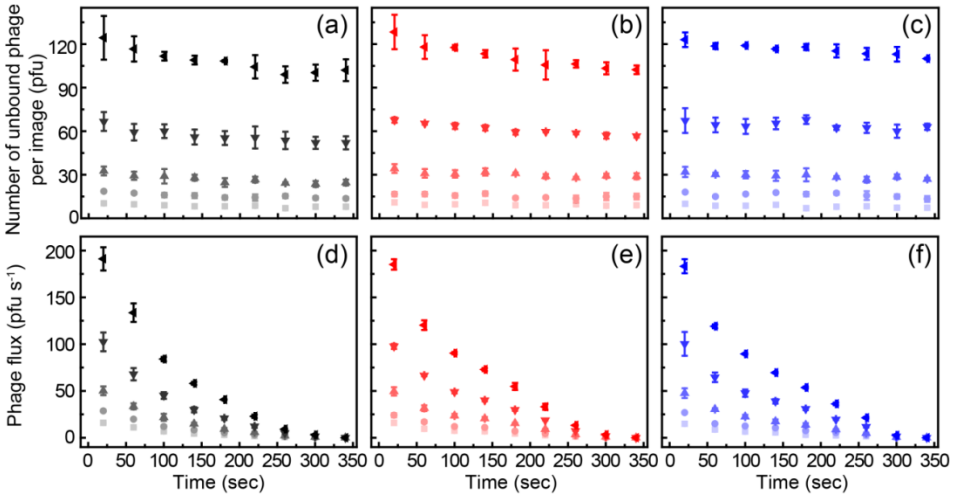

Figure 4.12 Concentrations of flowing phage over time. (a, d) Biotin-Fluor-PVM, (b, e) Biotin-Fluor-M13, and (c, f) Biotin-Fluor-Pf1.

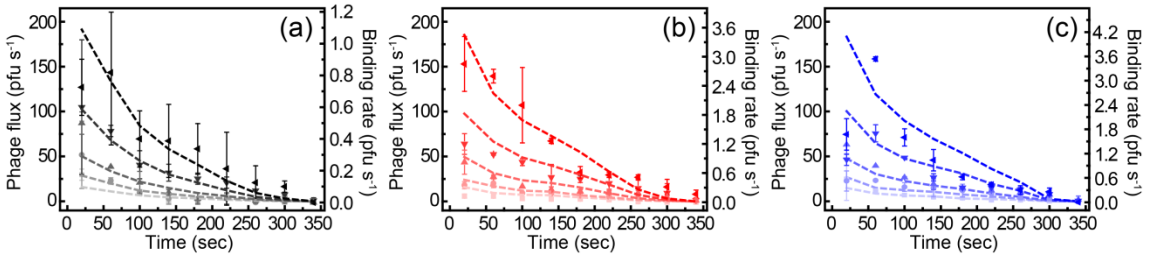

Figure 4.13 Comparison of binding rate with phage flux. (a) Biotin-Fluor-PVM, (b) Biotin-Fluor-M13, and (c) Biotin-Fluor-Pf1.

The three phage studied exhibited differences in width and length (Table 4.1); we therefore examined the dependence of binding on the physical properties. Specifically, because we varied both the phage dimensions as well as concentration we examined the dependence on several metrics related to the volume occupied by the phage, including total volume, surface area, and swept volume; The volume of phage was calculated by assuming they were cylindrical (volume = $\pi \times r^2 \times l$, where r and l are radius and length of phage, respectively). The surface area of phage was calculated by assuming they were cylindrical (surface area = $2\pi \times r \times l$). The swept volume was sphere volume that was created by phage rotating in a three dimension space (swept volume = $4/3 \times \pi \times l^3$). The total number of bound phage from a 25 μl background solution is shown as a function of number, volume, surface area, and swept volume of phage in Figure 4.14a, b, c, and d, respectively. The number of bound phage, in general, increased with any of these metrics. At a fixed concentration of $\frac{1}{16} \times 10^8$ pfu m^{-1}, for example, the number of bound Pf1 phage (longest) was greater than that of than PVM (shortest) phage (Figure 4.14a); this comparison suggested that phage size influenced binding. Neither the total volume occupied by phage (Figure 4.14b) nor the spherical volume swept out by phage as they flowed through the membrane (Figure 4.14d) were able to collapse all the binding curves. Instead, we found that the number of bound phage collapsed for all three phage onto a single curve as a function of the total cross-sectional (or surface) area, as shown in Figure 4.14c. These results showed the binding efficiency can be related to phage surface area, not volume. For example, even though the PVM and M13 phage had nearly the same relative volume, the surface area of M13 was twice that of PVM (Table 4.1). The surface area of phage can be also correlated as the number of coat proteins (CPs); PVM of ~1,

600 CP[127], M13 of ~2,800 CP[128] and Pf1 of ~7000 CP[129]. The larger surface area (or number of capsid proteins) of the elongated phage increased the probability of interaction between phage and fibers in the membrane; this result implies that phage with higher aspect ratios have better binding efficiency than lower aspect ratio phage with the same volume.

Table 4.1 Comparison of phage dimension properties

Phage	Diameter (nm)	Length (nm)	Relative volume *	Relative surface area**	Relative swept volume***
PVM	13	200	1	1	1
M13	6	900	0.96	2.07	91.12
Pf1	6	2000	2.13	4.61	1000

*Relative volume: The volume of phage was calculated by assuming they were cylindrical. PVM volume was set as reference volume and dividing other phage volumes (volume = $\pi \times r^2 \times l$, where r and l are radius and length of phage, respectively).

** Relative surface area: The surface area of phage was calculated by assuming they were cylindrical. PVM surface area was set as reference surface area (surface area = $2\pi \times r \times l$).

*** Relative swept volume: The swept volume was sphere volume that was created by phage rotating in a three dimension space (swept volume = $4/3 \times \pi \times l^3$).

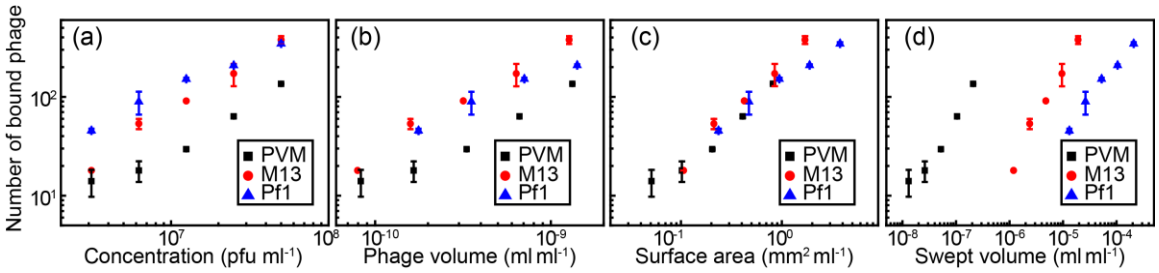

Figure 4.14 Number of bound phage as various functions of (a) concentration, (b) phage volume, (c) surface area and (d) swept volume.

Surprisingly, the swept volume did not correlate with the binding efficiency of phage, implying that phage do not rotate during flow. To evaluate the period of rotation for each phage during the flow, we applied Jeffery orbit theory and determined the theoretical rotational motion of ellipsoidal particles in a steady linear flow field.[122] This

theory was based on the assumption that Brownian motion does not play a role, and that the surrounding fluid is infinite with the only boundaries being those of the ellipsoid. Before calculating the period at which phage tumbled in flow, we first confirmed that our system approximately satisfied the two Jeffery orbit conditions: (1) the flow was laminar and steady, and (2) the advective transport dominated over diffusivity. Given the open pore network, we estimated the Reynolds number as $\mathrm{Re} = \rho DV/\mu$, where $\rho = 1094\ kg\ m^{-3}$ was the background solution density, D was the average fiber diameter, V was the phage velocity as a function of time (Figure 4.11a), and $\mu = 8.67cP$ was the solution viscosity measured at a fixed shear rate of 42 s^{-1} using an Ubbelohde viscometer. Similarly, we estimated the Péclet number as $\mathrm{Pe} = VD/D_p$, where D_p = 0.608 $\mu m^2\ s^{-1}$ was the measured translational diffusivity of the Biotin-FluorM13 (Figure 4.11b). The Reynolds number was less than one at all times as shown in Table 4.2, confirming that the flow was laminar and steady, and the Péclet number was greater than one at all times, suggesting that Brownian motion can be neglected. Finally, phage were rodlike with high aspect ratios and could be approximated as ellipsoids. We therefore applied Jeffery orbit theory to calculate the phage tumbling period, $\mathrm{T} = \frac{2\pi}{\dot{\gamma}}(r + 1/r)$, where $\dot{\gamma}$ was the average shear rate, calculated by dividing the flow rate by the pore diameter, and r was the aspect ratio of phage. The tumbling period varies inversely Although the lower aspect ratio of PVM was faster tumbling period than higher aspect ratio of phage (M13 or Pf1) (Table 4.2), in general every phage underwent barely tumbling in the flow, unless the tumbling was promoted by vorticity near fibers as discussed in Chapter 3. Hence, the swept volume can be ignored and not influenced the binding efficiency in our system.

Table 4.2 Péclet and Reynolds number of flow, and corresponding tumbling period of phage as a function of time

Time (sec)	Reynolds number	Péclet number (for M13 phage)	Tumbling period (sec)		
			PVM	M13	Pf1
20	1.7×10^{-4}	2.2×10^{3}	3.2	33	72
60	1.2×10^{-4}	1.6×10^{3}	4.3	47	107
100	8.8×10^{-5}	1.1×10^{3}	6.6	63	143
140	6.8×10^{-5}	8.9×10^{2}	9.4	75	181
180	5.1×10^{-5}	6.7×10^{2}	13	97	238
220	3.2×10^{-5}	4.2×10^{2}	22	155	345
260	1.5×10^{-5}	2.0×10^{2}	53	388	575
300	3.3×10^{-6}	4.3×10^{1}	160	1555	4607

Correlation of local flow with bound phage. Next, we investigated the effect of local flow conditions on the binding of phage. We hypothesized that the relevant region of the local flow that controlled the binding of phage is that near/on the fiber surfaces, where phage bound. Hence we identified the locations of fibers in the fluorescence movies by acquiring bright field images in the same focal area. Next, the flow rate profile was extracted across the entire fiber area and the specific local flow rates were obtained at the positions where phage bound. Similarly, the specific flow directions were correlated to fiber orientation at the positions where phage were bound. These correlations allowed us to relate the magnitude and direction of the local flow to the likelihood that phage were bound there.

The specific local flow rates and directions at the locations of bound phage varied with time, as shown in Figure 4.15. Because the capillary flow rate decreased with increasing time, the local flow velocity also varied over time. To determine the effect of the relative local flow rate at a given time after breakthrough, we normalized the magnitude of the flow rate by the difference between the local minimum and maximum for each PIV result. The average local flow rate was calculated across the entire fiber area

at each PIV result at 20, 60, 100, 140, 180, 220, 260, 300, and 340 sec. We defined slower and faster flow domains as those domains in which the local flow rate was slower and faster, respectively, than the average local flow rate. Distributions of the number of bound phage as a function of the specific local flow rate are shown in Figure 4.16 Each type of phage (PVM, M13, Pf1) bound in greater numbers in the faster local flow domain than in the slower domain (Figure 4.17). The result that phage were more likely to bind in the faster local flow domain is consistent with the idea that higher phage flux promotes binding; this idea arose in the context of the bulk flow studies (Figure 4.13).

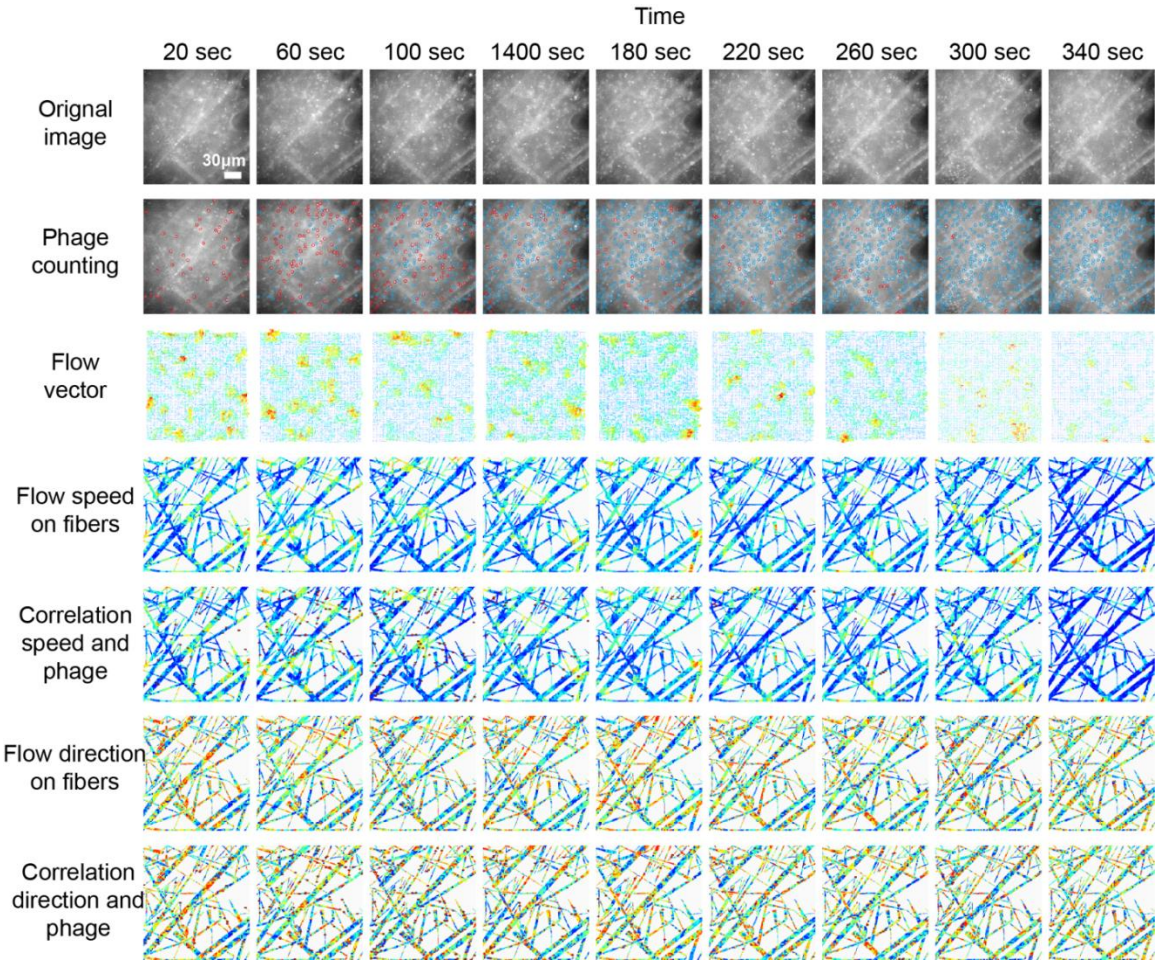

Figure 4.15 Correlation of local flow with locations of bound phage.

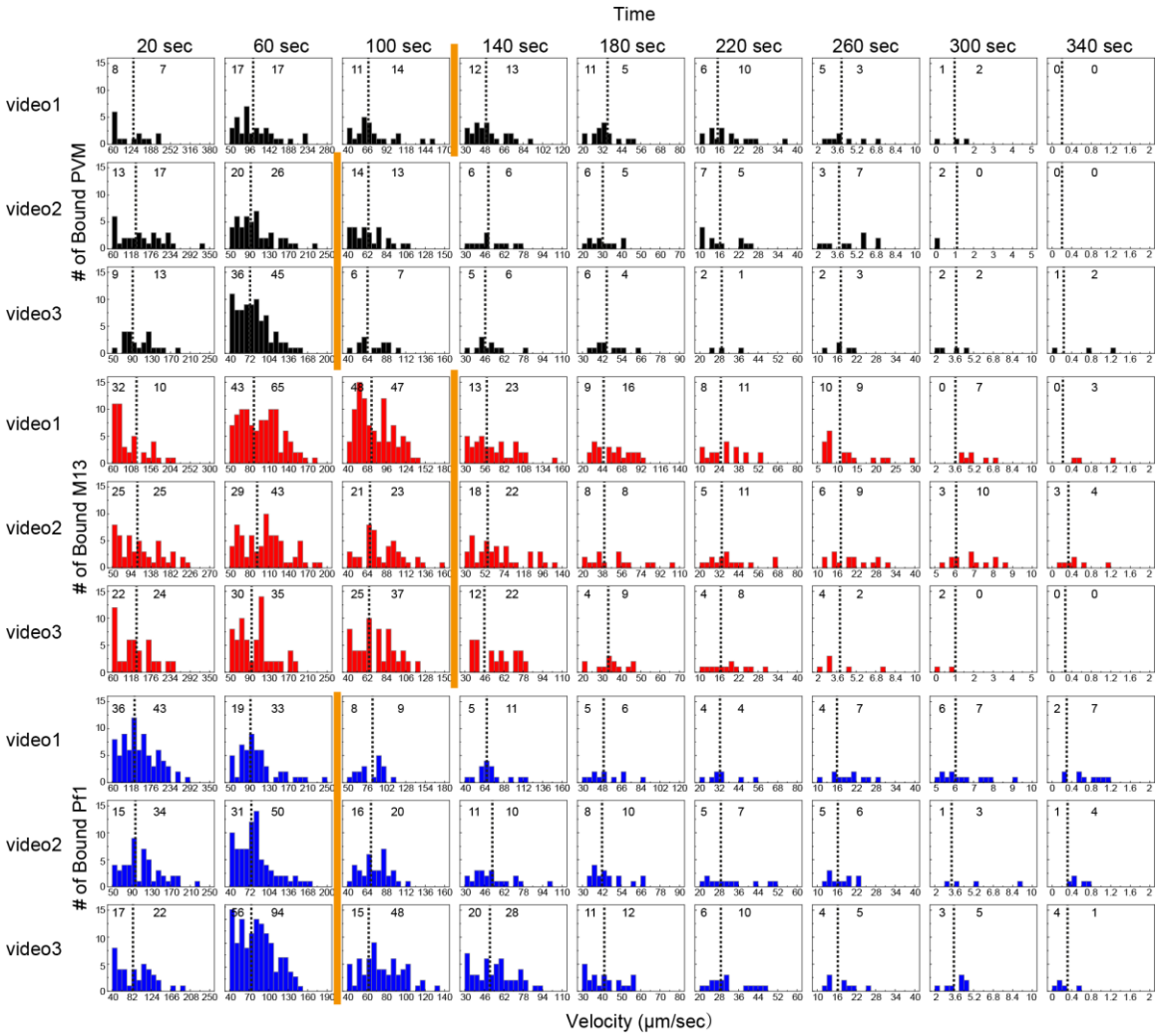

Figure 4.16 Binding distributions as a function of local flow rate and time.

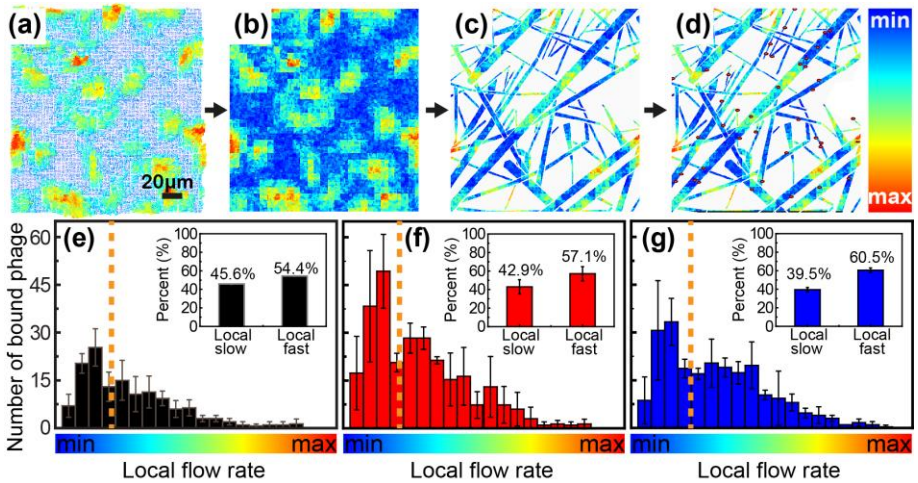

Figure 4.17 Binding efficiency depends on local flow rate.

Similarly, we compared the likelihood of binding to the angle at which the local flow encountered the fiber. Here, we surmised that the vorticity generated by flow near the fiber surface might reorient the phage and hence influence their binding interaction. In contrast to the results for local velocity, however, phage did not exhibit a preferred local flow direction for binding (Figure 4.18). Instead, the distribution of local flow angles across the bound phage population was constant within the errors of the measurements. This omnidirectional binding likely arises from the large number of bonds that could be formed from the biotins attached to the phage major coat proteins. Phage approaching the fiber could be captured on any of the biotins, thereby diminishing the orientation dependence.

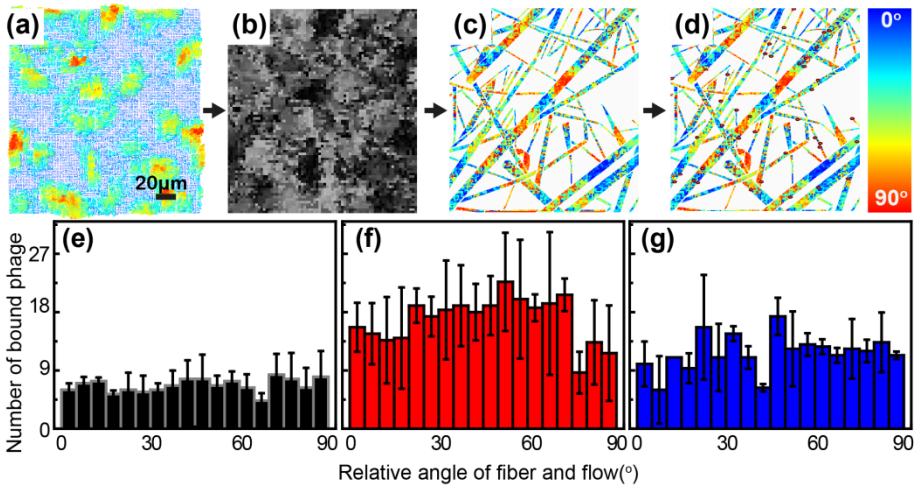

Figure 4.18 Relative flow angle does not affect binding.

4.4 Conclusions

In this study, we investigated how two assay parameters, phage size and flux, influence the binding efficiency of reporters in LFA membrane. Filamentous phage of different sizes (PVM of length 0.2 μm, M13 of length 0.9 μm, and Pf1 of length 2 μm) were functionalized with biotins and AlexaFluor 555. A Fusion 5 membrane was used in

LFA as a solid capture phase. Increasing the phage length and the average bulk flux increased the likelihood that phage encountered a fiber, thereby increasing binding interaction. We confirmed these ideas from the bulk assays by measuring the local flow rate and angle relative to the fibers as a function of time. Phage were more likely to bind in the faster local flow domain, consistent with the bulk flow results, but exhibited no preference for binding in the local flow direction relative to the fiber axis.

Our results suggest that tuning the flux and size of phage can increase the binding efficiency of elongated reporters in fibrous membranes. In turn, this suggests that careful tuning of membrane design variables such as the pore diameter and membrane geometry (which control the local flow rate and hence the bulk flow rate) could increase the sensitivity of LFAs. There are limitations, however, on the ranges of these variables that are feasible for applications. A too-small pore diameter may deleteriously reduce the flow rate and prevent transport of phages or of analytes to the functionalized test region. An ultrasensitive LFA (as demonstrated in Chapter 2) was capable of detecting a few analytes [100 MS2 viruses per strip]. A poorly designed membrane may cause significant loss of analyte prior to the test line, leading to poor signal-to-noise. Our study therefore suggests that tuning membrane parameters (or reporter parameters) to promote reporter binding efficiency is one route towards developing ultrasensitive LFAs.

Chapter 5. Understanding Mechanism of Temperature-tolerant M13 Bacteriophage

5.1 Introduction

Although the sensitive phage reporter was developed in Chapter 2, preservation of the functionalized phage remains a significant challenge to reproduce the reliable assay that may facilitate the use of PoC devices in resource-constrained settings with lack of storage amenities. In contrast to the extremely stable gold nanoparticles typically employed in LFAs, M13 phage is a biomaterial and has a half-life up to 120 days at desiccated, anhydrous, and room temperature conditions at which LFA products are distributed and stored.[130] The phage particles are assembled with the coat proteins that may become denatured when not in their native environments, resulting in protein degradation. To enhance M13 reporter stability and physical resistance, we selected mutant M13 phage that survived in one extreme environment of near-boiling temperatures of 98℃. Then, we sequenced the genome of the temperature-tolerant M13 phage to understand the origin of its thermostability phenotype. To select and isolate temperature-tolerant phage, we incubated M13K07 helper phage at temperatures that were steadily increased from 90℃ to 98℃, as shown in Figure 5.1. After isolating the mutants, we confirmed their thermal stability by two methods: (i) determining the survival rate as a function of temperature from 80℃ to 98.3℃, and (ii) using a thermal shift assay to measure the melting temperature of phage. Mutants exposed to a temperature of 90℃ for 30 min exhibited temperature tolerance that was up to 200-fold greater than the parental phage. The melting temperatures of the mutants showed 2℃ shift from the parental phage.

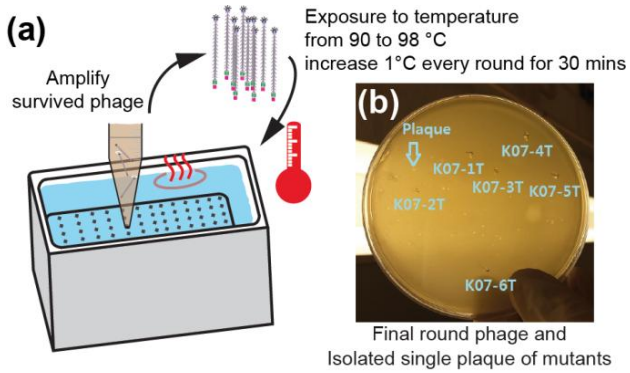

Figure 5.1 (a) Schematic of selection of temperature tolerant phage, and (b) isolated mutant phages on the top-agar plate.

To elucidate the thermostable phenotype of the isolated M13 mutants, the first step would be to investigate mutations in the structural proteins encoded by the phage. M13 phage contains a circular single-stranded DNA (ssDNA) of 6,407 bases packaged in the coat proteins. The reproductive life cycle of phage starts with the adsorption of phage to the tip of the F-pilus of the host *Escherichia coli* (*E. coli*), mediated by p3 coat (viral adsorption) protein. Next, the phage genome is subsequently transported into the cell cytoplasm. The phage genome of (+) ssDNA is converted into a double-stranded DNA, called replicable form (RF) DNA (+/-) (Figure 5.2); (-) strand synthesis starts at the stem-loop b and c in the intergenic region (Figure 5.3b) by the action of host enzyme. The RF DNA is used as the template for subsequent phage DNA replication, as well as for encoding 11 proteins associated with phage assembly (p1, p4 and p11), phage coat proteins (p3, p6, p8, p7 and p9), phage DNA replication (p2 and p10), and ssDNA binding protein (p5). For DNA replication of the (+) strand synthesis, the p2 protein covalently binds and cut the nick site in the step-loop d (Figure 5.3c); then the rolling circle DNA replication is initiated.

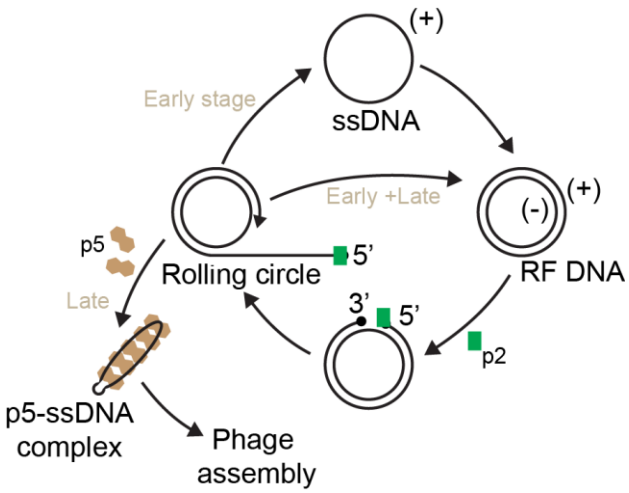

Figure 5.2 Mechanism of M13 phage DNA replication cycle.

In this study, we used M13KO7 helper phage. M13K07 helper phage is a variant of wildtype M13 whose origin of replication (specifically, domain B in M13 Ori) is disrupted by insertion of a different origin of replication, p15A and a kanamycin resistance cassette (Figure 5.3d). Even though p15A Ori ensures a replication of the phage genome in the cells independently of p2 protein, the disruption of M13 origin leads to a decrease in the packaging efficiency of the phage. Taking advantage of this latter property, helper phage are used widely for packaging of phagemid vectors. A phagemid is a dsDNA plasmid which contains the M13 or f1 origin of replication. This phagemid can be packaged as ssDNA into phage particles in the presence of a helper phage which provides all the necessary proteins for particles formation.

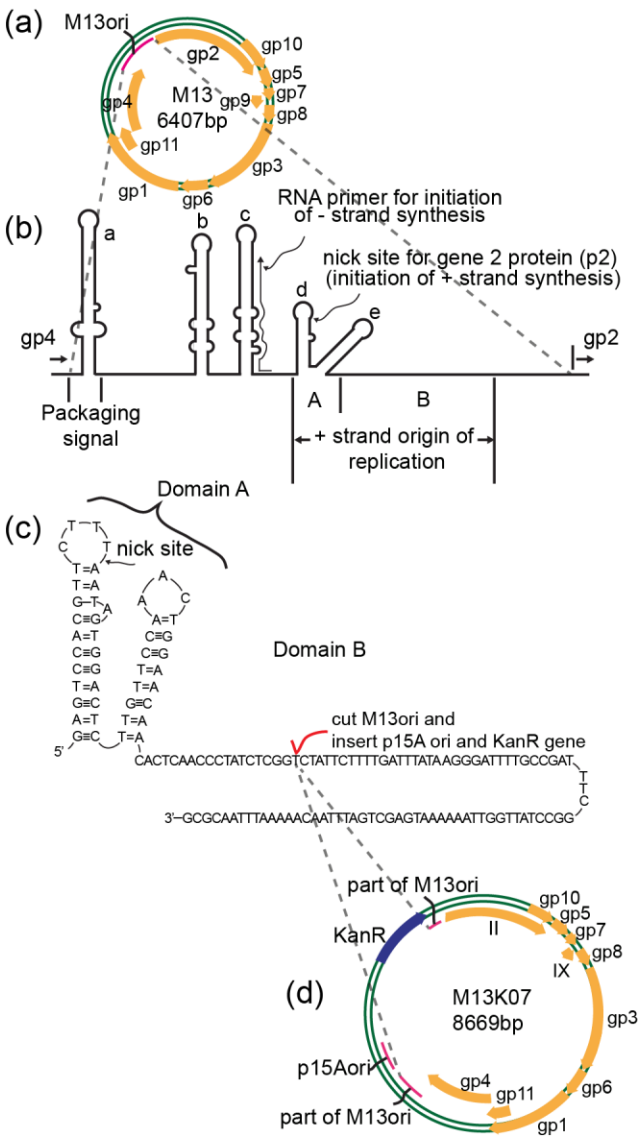

Figure 5.3 Comparison of genomes between M13and M13KO7 phage.

To understand the nature of the mutations responsible for the thermostability phenotype and their localization in the genome, we sequenced phage genome using next-generation multiplex sequencing (Illumina). Illumina sequencing, also known as barcode sequencing, is a fast and high-throughput sequencing technique. It can process up to 96 pooled samples in a single run, dramatically reducing sequencing cost and time. Sequencing outputs were about 20 million reads per sample with 150 read lengths that are more than sufficient to cover whole phage genomes, which contains 8,669 base pairs. The

sequencing outputs were aligned to a reference genome of M13K07 (accession number, HH807327) or to the parental phage used in the selection process to identify variation in the DNA of the isolated thermostable mutants. Based on the sequencing results, we present three potential mechanisms for the apparent increase in temperature tolerance: gene replication enhancement (due to mutations in gp2), miniphage, and mutations in the p7 coat protein.

5.2 Materials and Methods

Screening of temperature-tolerant mutant M13K07. M13K07 helper phage (#37468) was purchased from ATCC® and used as the parental phage. A 15 ml Falcon tube containing 1 ml of 5×10^{10} pfu ml^{-1} parental phage was immersed in a circulating water bath at 90˚C for 30 min. The phage suspension was then mixed with 100 µl of overnight fresh *E. coli* strain TG1 culture and grown overnight at 37˚C in a total volume of 10 ml LB medium supplemented with 25 µg ml^{-1} kanamycin. The grown bacteria were pelleted by centrifugation at 3,200 rpm and the supernatant filtered through 0.2 µm membranes (Corning, #CLS431227). The produced phage was concentrated to 1 ml volume in PBS by PEG precipitation and then used in the next round of selection. This procedure was repeated while increasing the screening temperature from 90˚C to 98˚C in one degree increments for each round for a total of nine rounds (Figure 5.1a). After the final round at 98˚C, the surviving phage particles were serially diluted and titered as shown in Figure 5.1b. The phage plaques were formed on 0.7% w/v of top agar on TG1 bacteria lawn. Six single plaques were isolated and amplified. We named each isolated mutant as K07-1T, K07-2T, K07-3T, K07-4T, K07-5T, and K07-6T. The titer of all 6

mutants as well as the parental phage was calculated and phage stocks were then stored at 4˚C.

Measuring temperature tolerance of mutant M13K07. 1 ml of 1×10^{10} pfu ml^{-1} from each of the six mutants and the parental phage were incubated at five different temperatures: 80, 85, 90, 95, and 98.3˚C for 30 min in a circulating water bath. After incubation, all 35 samples were titrated to determine plaque forming unit of the surviving phage. Thermal shift assay validation: 3 µl of 100× SYPRO Orange Protein Gel Stain (Sigma-Aldrich, #S5692-50UL) was mixed with 27 µl of 1×10^{11} pfu ml^{-1} phage. Thermal scanning (70˚C to 98˚C at 1˚C /5min) was performed using real-time PCR (Agilent Technologies, Mx3005P QPCR System) and fluorescence intensity was measured every 5 min during temperature increase.

Isolation of a replicative form (RF) DNA of phage genome. As required by the Illumina sequencing protocol, we converted single stranded DNA phage genome to double-stranded replicable form (RF) DNA by infecting phage into *E. coli* TG1. Six mutants and parental phage were each grown in *E. coli* culture overnight at 37˚C in 5 ml LB medium supplemented with 100 µg/ml ampicillin and 30 µg/ml kanamycin. The TG1 cells used here were *E. coli* bacteria carrying a pCAC2 plasmid conferring ampicillin resistance. The pCAC2 plasmid is irrelevant for the purpose of our experiment, but was used as an additional resistance selection parameter. Since M13K07 carry kanamycin resistance gene, infected TG1 can be grown in a medium containing both ampicillin and kanamycin antibiotics, verifying that RF DNA is formed in the specific host cells.

The phage RF DNA and pCAC2 were extracted from the infected TG1 using QIAprep® Spin Miniprep Kit (QIAGEN, #27106). 4 µg of the extracted DNA was

linearized with 40 units of HindIII (BioLabs, #R0104S) restriction enzyme in 1×CutSmart® buffer (BioLabs, #B7204S), and subsequently purified using DNA Clean & Concentrator™-5 (Zymo Research, #D4013). Both dsDNAs, pCAC2 and M13 RF DNA contain one restriction site for HindIII. To verify the size of the linearized DNA, gel electrophoresis was performed in 0.6 % w/v agarose (Sigma-Aldrich, #A9539-250G) in 1×TAE buffer at 94V at 4˚C.

Separation of linearized M13 RF DNA and pCAC2 plasmid in the digested DNA samples was done using QIAquick® Gel Extraction Kit (QIAGEN, #28074). To avoid DNA dye contamination during gel extraction, we ran two identical 1 µg DNA samples on a 0.6% w/v agarose gel in 1×TAE buffer at 94V at 4˚C at the same time. We extracted one of the lanes and stained it with 0.5 µg/ml ethidium bromide (Sigma-Aldrich, #28751-1G) in DI water for 15 min. The location of RF DNA band was identified on the Ultraviolet Transilluminator (FisherBiotech, #FBTI614) and marked using the edge of a razor blade. We replaced the marked lane and matched it to the unstained lane. The RF DNA band was cut out of the unstained lane by inferring its location from the marked lane.

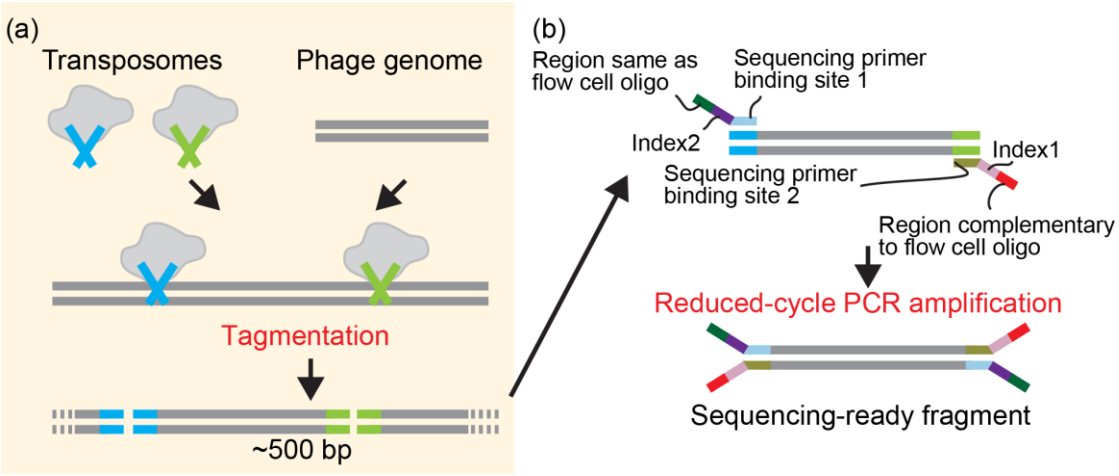

Figure 5.4 Schematic of genome tagmentation and amplification.

Next-generation and multiplex sequencing. Nextera XT DNA Library Preparation Kit (#FC-131-1024) was purchased from Illumina. For the DNA library preparation, we first performed the tagmentation (Figure 5.4a). We mixed 10 µl Tagment DNA Buffer, 5 µl of 0.2 ng/µl DNA and 5 µl Amplicon Tagment Mix. The mixture was placed in a thermocycler (BIO-RAD, MJ Mini). The reaction of tagmentation was carried out at 55˚C for 5 min and held at 10˚C, after which the mixture was neutralized by adding 5 µl Neutralize Tagment Buffer.

Table 5.1 Index information

Sample id	Index 1	Index 2
K07-1T-1K	N701 - TAAGGCGA	S517 – GCGTAAGA
K07-1T-2K	N702 - CGTACTAG	S517 - GCGTAAGA
K07-2T	N703 - AGGCAGAA	S517 - GCGTAAGA
K07-3T	N704 - TCCTGAGC	S517 - GCGTAAGA
K07-4T	N705 - GGACTCCT	S517 - GCGTAAGA
K07-5T	N706 - TAGGCATG	S517 - GCGTAAGA
K07-6T	N701 - TAAGGCGA	S502 - CTCTCTAT
M13KO7	N702 - CGTACTAG	S502 - CTCTCTAT
control	N703 - AGGCAGAA	S502 - CTCTCTAT

For the PCR-amplification of the tagmented DNA (Figure 5.4b), tagmented DNA library was mixed with 15µl Nextera PCR Master Mix, 5 µl index 1 primer, and 5 µl index 2 primer. The indices pairs for each sample library are listed in Table 5.1. The conditions for the PCR-amplification with the mixture in the thermocycler were as follow: initial denaturation for 3 min at 72˚C followed by 30 sec at 95˚C, 12 limited-PCR cycles (denaturation for 10 sec at 95˚C, primer annealing for 30 sec at 55˚C and extension for 30 sec 72˚C), and final extension for 5 min 72˚C. The amplified DNA library was cleaned up using AMPure XP beads (Backman Coulter, # A63880) and a magnetic stand. We

evaluated the quantity and quality of the amplified libraries using Qubit® 2.0 Fluorometer (#Q32866) and Agilent High Sensitivity DNA Kit (#5067-4626). All DNA libraries were pooled with 1:1 volume ratio with 4 nM in the 1.5 ml Eppendorf tube. Finally, the pooled library was sequenced using NextSeq 500/550 kit v2 mid output 300 bp cycle (Illumina, #FC-404-2003) and Illumina MiSeq system (Figure 5.5).

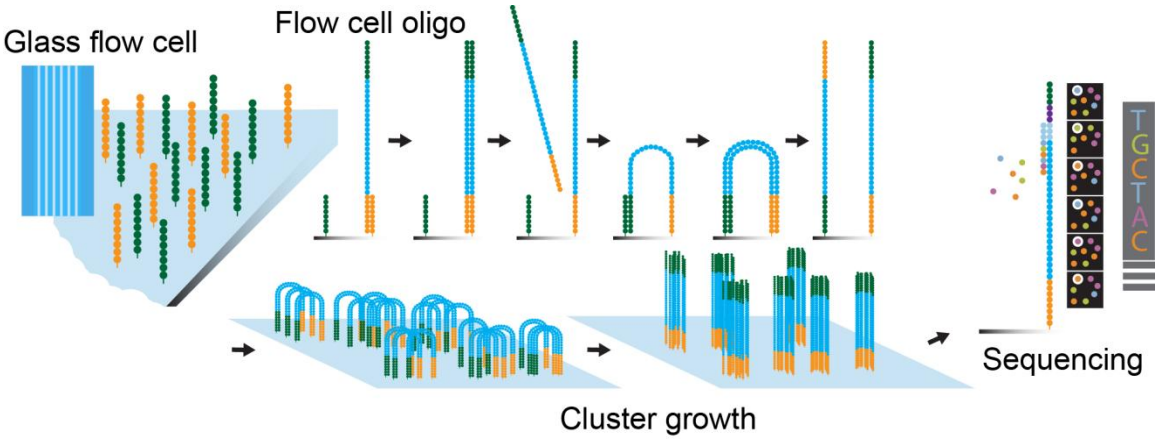

Figure 5.5 Schematic of next-generation sequencing read-out mechanism.

5.3 Results and Discussion

We selected and isolated six mutants of M13KO7 which were able to infect E. coli TG1 cells after exposing them to high temperatures (90˚C — 98˚C). We tested their temperature stability by determining survival rates as a function of temperature (Figure 5.6a) and by measuring the phage melting temperatures (Figure 5.6b). The viability of M13, in general, decreases significantly after its incubation at temperatures above 80 ˚C. However, all mutants had a higher fractional survival than the parental phage. At 85 ˚C most mutants had ~10^{-2} survival fraction, whereas the survival rate of parental phage was 4×10^{-5}. At 90˚C, most mutants had ~4×10^{-6} survival fraction, over two hundred fold greater than that of the parental phage (4×10^{-8} survival fraction). Figure 5.6b shows the intensity from SYPRO Orange dye that emits light when the dye interacts with the

hydrophobic sites of unfolding proteins. The SYPRO Orange, binding assay, allows the estimation of the apparent melting temperature (T_m) by searching the inflection point of the melting curves. All mutants showed 2℃ shift of the melting temperature from the parental phage.

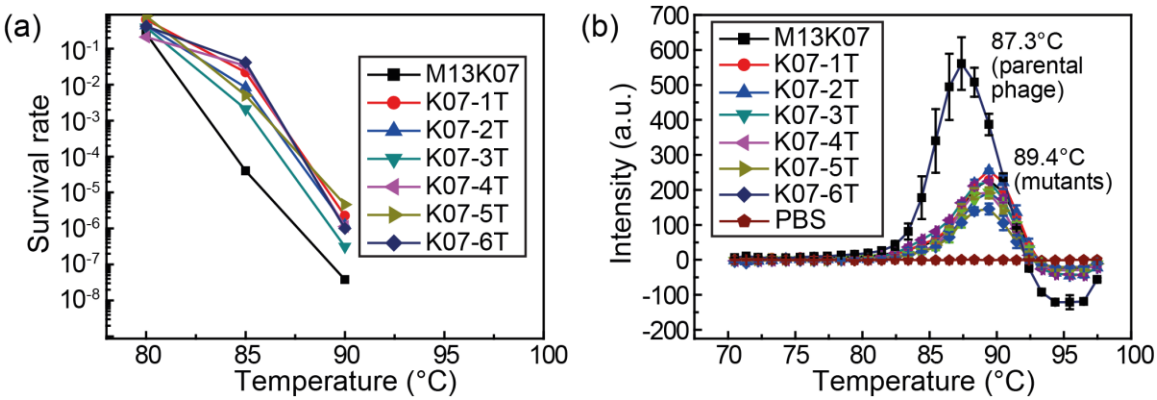

Figure 5.6 Estimation of temperature stability of mutant phage.

To investigate mutations in the genome, we first extracted plasmids from the host cells infected by the isolated variants or parental phage. The extracted plasmids included RF DNA that consisted of both phage DNA and the pCAC2 plasmid originally carried by the host cell. To test the quality of the plasmids, we performed gel electrophoresis. We identified the multiple DNA bands that appeared on the gel (Figure 5.7a), responsible for the nicked and supercoiled forms. After linearization of plasmids using HindIII restriction enzyme, the multiple bands turned into the two bands of phage DNA and pCAC2 plasmid (Figure 5.7b), because both phage RF DNA and pCAC2 plasmid contain HindIII restriction site. The control lane included only the pCAC2 plasmid obtained from the non-infected host cells, confirming that the heavier DNA band is phage DNA (Figure 5.7b). For K07-1T sample, we observed strong DNA band signal at 1k base pair (bp) and 2k bp, and decided to isolate those two DNA bands that were then labeled as K07-1T-1K

and K07-1T-2K, respectively. Finally, RF DNAs were separated from pCAC2 in the linearized DNA samples using gel extraction kit (Figure 5.7c).

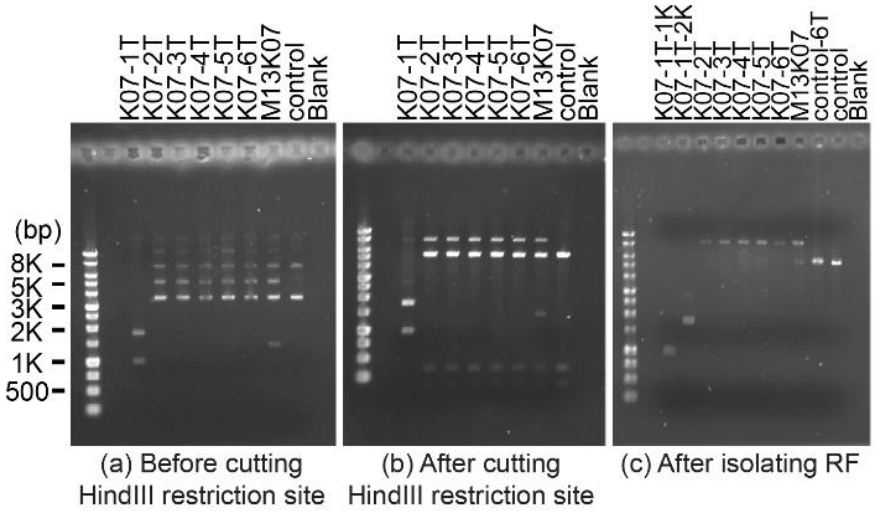

Figure 5.7 Isolation of RF DNA from infected host cells.

We used Illumina multiplex sequencing to sequence phage genome. To do this, we first prepared the DNA library. The preparation of DNA library included tagmentation and amplification. In the tagmentation step, the transposome enzyme simultaneously fragments and tags the phage DNA. The DNA fragments were subsequently PCR-amplified to add unique indices and sequencing primers at the end of the fragments. The concentration of the prepared DNA libraries was around 15 nM, and its sizes and distributions fall within the expected range (35—7,000 bp), as shown in Figure 5.8. All DNA libraries were mixed and pooled together with 1:1 volume ratio with 4 nM in a single 1.5 ml Eppendorf tube. Each phage DNA library can be distinguished from the others by reading the unique indices. We sequenced the pooled library using NextSeq 500/550 kit v2 mid output 300 bp cycle. The total read number of sequencing output was ~20 million for each sample library, and the read lengths were both 150 bp for forward and reverse read (Table 5.2).

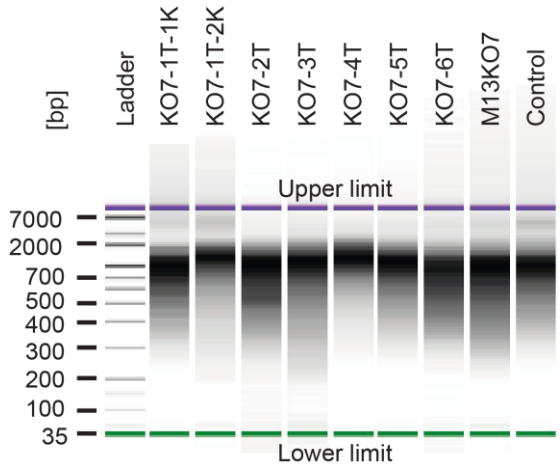

Figure 5.8 Sizes and distributions of phage DNA library.

Table 5.2 Sequencing output information

Sample id	Number of reads (bp)	Read length (read1, read2)	File type
K07-1T-1K	20,141,786	150 bp, 150 bp	FASTQ
K07-1T-2K	16,739,866	150 bp, 150 bp	FASTQ
K07-2T	8,616,120	150 bp, 150 bp	FASTQ
K07-3T	17,506,610	150 bp, 150 bp	FASTQ
K07-4T	9,513,150	150 bp, 150 bp	FASTQ
K07-5T	13,252,254	150 bp, 150 bp	FASTQ
K07-6T	22,798,244	150 bp, 150 bp	FASTQ
M13KO7	23,827,868	150 bp, 150 bp	FASTQ

The sequencing output for each library is a FASTQ file of size ~2 gigabytes, as shown in Table 5.2. For alignment of the parental DNA of M13KO7, we first selected 2 million reads whose length were more than 100 bp with no read errors from ~22 million data; even though 150 bp of each DNA fragment was read, some readings were not complete and contained non-read signals. Two million reads were sufficiently large to cover the phage genome DNA, whose size is 8,669 bp. The filtered data was aligned on a reference M13K07 genome (Accession number: HH807327) obtained from the National Center for Biotechnology Information (NCBI) using SeaView4.5.4.[131] However, we

could not match exactly our parental phage to the reference. Table 5.3 shows disagreement of nucleotides of parental phage with the reference data at multiple locations. Based on the differences in temperature stability between parental phage and the mutants, we decided to use the parental phage genome as a base line to align and compare mutant genome DNA.

Table 5.3 Disagreement of parental phage genome with reference data at multiple locations

Disagreement location	M13KO7 (from reference data)	M13KO7 (from our parental phage sequencing)
1737	T	C
2710	A	G
4453	T	A
4471	T	A
4477	A	T
4479	T	A
4480	T	C
4489	A	T
4747	A	T
4786	T	A
5374	A	G
5443	C	T
8445	C	T

The DNA coverage across the genome was not uniform (Figure 5.9), indicating some DNA fragments were not read efficiently. However, the read number was indeed large enough to complete phage genome sequence. After comparing the mutants' genome to the parental phage genome, we identified mutations in ORF of genes at gp2, gp7, gp9 and M13ori, as shown Table 5.4. The short DNA samples of K07-1T-1K and K07-1T-2K were part of the phage genome. K07-1T-1K was 1,379 bp, containing M13origin and packaging signal. K07-1T-2K was 2,858 bp, containing gp4, M13ori, p15Aori, and packaging signal.

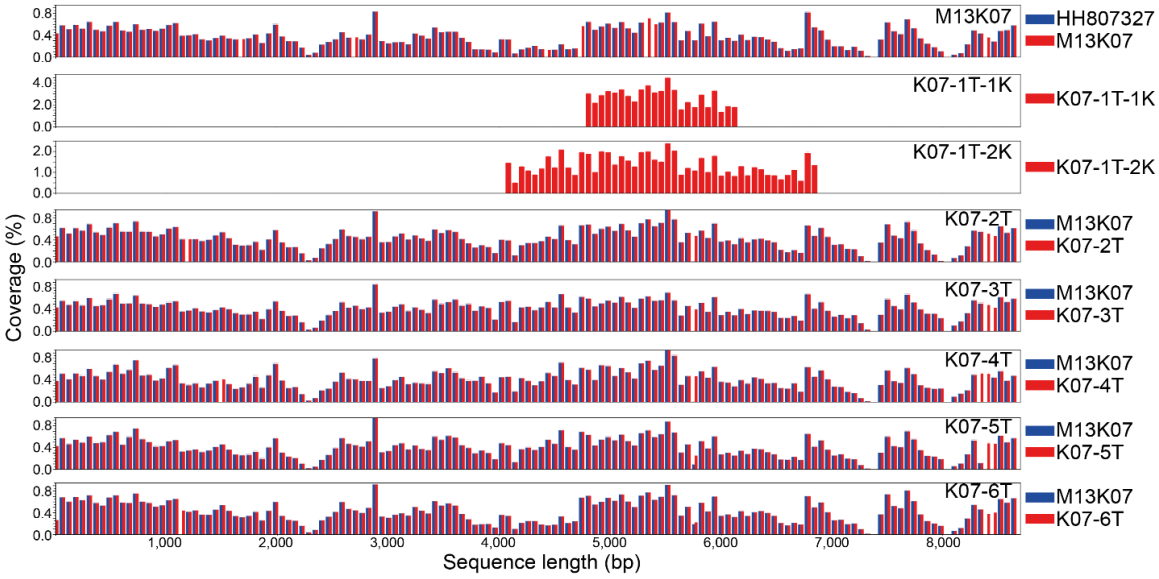

Figure 5.9 Coverage of DNA alignment.

Table 5.4 Mutated nucleotides

Location	Sample id	Mutation	Gene included	Amino acid change
1199	K07-6T	G → C	gp7	G31A
1217	K07-2T	A → G	gp9	Silent
1555	K07-4T	C → T	Noncoding region	.
5778,5779,5780	K07-2T, 3T, 4T, 5T, 6T	deleted	M13ori	.
8387	K07-4T, 5T	G → C	gp2	M40I
8445	K07-2T, 3T, 4T, 5T, 6T	T → C	gp2	L60F
8484	K07-2T, 3T, 5T, 6T	G → A	gp2	G73S
4801-6180	K07-1T-1K (1,379 bp)		M13ori, packaging signal	
4078-6936	K07-1T-2K (2,858 bp)		gp4, M13ori, p15Aori, packaging signal	

Here, we suggest three potential mechanisms underlying the observed temperature stability based on the mutations found in the different variants:

(1) *Gene replication enhancement*. M13ori of M13KO7 helper phage is disrupted by an insertion of p15Aori and kanamycin resistance gene. Because of this insertion, the

gene copy numbers from M13ori decrease significantly by 100-fold, compared to WT M13.[132] This decrease in M13K07 DNA replication can be rescued by mutations found in p2 protein, which binds to nick or relax at M13ori. Two previously identified changes in the amino acid sequence of gp2 were shown to increase the rate of DNA replication, M40I and G73S. M40I gp2 mutant was shown to increase the co-operativity of protein-protein interactions, which are necessary to bind M13ori and form a functional complex for the nicking reaction.[133] G73S gp2 mutant also showed much higher nicking activity than the wild type gp2 by reducing superhelicity requirement on relaxed DNA.[133] Table 5.5 shows that K07-4T and 5T have the M40I mutation in gp2, and K07-2T, 3T, 5T, 6T contain G73S mutation. Hence, the mutations in p2 could enhance the gene replication of these variants. In this case, the survival rate in Figure 5.6a may be misread as temperature tolerance instead of gene replication efficiency. Because the survival rate was calculated based on titration, the gene replication and growth rate of phage on the plate could affect the result of the plaque forming unit; we suggest that gp2 mutants increased gene replication and production of ssDNA, increasing the number of plaque forming units.

(2) *Miniphage.* The length of filamentous phage is determined by the length of viral DNA that is encapsulated within viral particles. Typical wild type M13 is 990 nm long and 6 nm width. One literature study reported very short M13 mutants, whose size is one-fifth to one-half that of standard M13, that were discovered after multiple passages of infection.[134] The multiple passages lead to high multiplicities in which mutants accumulated and overgrew the wild-type phage. Those deletion mutants, called miniphage, cannot replicate themselves without helper phage due to more than 70% loss of the genome. We isolated the genomes of K07-1K-1T and K07-1K-2T whose size is

1,379 bp and 2,858 bp, respectively. K07-1K-1T contains part of M13ori (including the nick site) and packaging signal. K07-1K-2T contains gpIV, part of M13ori, p15Aori, and packaging signal. Because these mutants include both the origin and the packaging signal, the mutants can be packaged and propagated acting as a phagemid with helper phage during infection cycles. Moreover, short phage are known to exhibit greater heat resistance; for example, M13 microphage was shown to be more resistant to heating in 1% SDS at 70 ℃ in comparison to full-length phage.[135] Therefore, the production of miniphage may also explain the increased temperature tolerance.

(3*) Mutations in the coat protein*. The amino terminal residues of the p7 and p9 interact with p8 major coat proteins and viral DNA. The p9 is exposed on the surface, whereas p7 (located at the same end) is buried. The p7 and p9 are essential to initiate viral particle assembly in the host cell. To initiate assembly, p7 and p9 first interact with the packaging signal in p5-ssDNA complex, followed by the p7 binding to p8 major coat proteins.[136] K07-2T and K07-6T showed nucleotide variations in gp9 and gp7, respectively (Table 5.4). The gp9 mutation was a silent mutation and did not lead to a chance in the amino acid sequence. However, K07-6T had G31A mutation in p7. The G31A mutation may improve heat resistance of phage; deformation of p7 by heat may break interaction with the viral ssDNA and p8, leading to ssDNA leakage from capsid proteins.

5.4 Conclusions

We isolated six variants of M13KO7 phage that exhibited temperature tolerance. To identify the reasons underlying the temperature tolerance, we sequenced the genome of all mutants using next-generation sequencing. The phage variants showed nucleotide

changes in gp2, gp7, gp9 and M13ori. Based on the results from sequencing, we suggest three potential mechanisms for the apparent increase in temperature tolerance: gene replication enhancement (due to mutations in gp2), miniphage and mutations in the p7 coat protein. The selection and growing of the surviving phage in the extreme condition is a simple method to isolate phage particles with enhanced properties. To understand the cause of the enhancement, next generation sequencing is a powerful tool to search for mutations in the genome that influence the phage temperature stability.

Chapter 6. Development of Portable, Ultrasensitive, and Smart phone-Based Light Detector for Measurement of 1,5- Anhydroglucitol

6.1 Introduction

Point-of-care (PoC) testing is performed at or near the site of patient care rather than in the traditional central laboratory.[137] One of the best examples of PoC diagnostics is the hand-held glucose meters for determining glucose concentration in blood. This technique has evolved from the demands of self-monitoring of blood glucose for diabetic patients. Measurement of blood glucose is required for appropriate diabetes treatment, especially for adjustment of insulin dosing. The number of people with diabetes has increased dramatically over the past 35 years.[138] Having uncontrolled diabetes and too high level of blood glucose can cause serious problems, such as cardiovascular disease, retinopathies and nephropathies.[138] The majority of diabetes most often developing in middle-or older aged people (accounting for 90 to 95% of cases) is type 2 diabetes (T2D) which is formally called non-insulin-dependent diabetes.[139] A tight glycaemic control is required for patients to maintain the blood glucose at normal level, improving their health conditions by delaying or avoiding chronic complications. For early diagnosis of T2D, some metabolites can be measured as a clinical marker for glycemic monitoring, such as 1,5-anhydroglucitol (AHG), haemoglobin (HbA1c) and glucose in blood samples.[140] AHG is an unmetabolizable glucose analogue that is present in human blood predominantly due to dietary ingestion.[141] Physiologically, the human body rebalances AHG level by readsorption through the kidneys and by excretion in urine; normal range of AHG level in human body is around 6.8–32.3 μg/ml.[141] AHG concentration in blood decreases during times of hyperglycemia, resulting from urinary excretion of AHG which

is competitively inhibited by glucose to readsorb in the blood. Once hyperglycemia is corrected, AHG begins to reabsorb from the kidney back into normal level at a steady rate, approximately taking two to four weeks.[141] As a result, even if the blood glucose testing shows normal values, AHG level could be on the way back to normal, enabling to identify glycemic variability or a recent history of high blood glucose. Therefore, AHG level monitoring maybe provide T2D patients with optimizing therapy solutions.[142]

Conventional methods such as liquid chromatography (LC), gas-liquid chromatography and high performance liquid chromatography (HPLC) are typically used to determine the concentration of AHG in the serum.[143]; typical detection limit of AHG using HPLC is 0.2 μg ml^{-1}.[144] However, these methods exhibit several critical disadvantages for PoC monitoring (i.e. in a home setting); they require a large amount of sample volume, a series of sample preparations, complex laboratory equipment, and trained personnel. An appealing alternative to these conventional methods is to use enzymatic systems. As one example, pyranose oxidase (PROD) has been used for determining D-glucose and AHG in clinical analysis.[143] PROD oxidizes the second position hydroxyl group of AHG and thereby generates hydrogen peroxide (H_2O_2), which can be detected using a variety of methods, including colorimetry,[145] electrochemical[146] and chemiluminescence (CL) assay.[147] Among these technologies, CL method is one of the most promising ones for detection of H_2O_2 due to its high specificity and sensitivity.[147] The CL assay is based on the substrate 5-amino-2,3-dihydro-1,4-phthalaxinedione (luminol) which emits a blue glow (at 428 nm peak) in the presence of oxidizing reagents of H_2O_2, and catalyst such as horse radish peroxidase (HRP).

A recent report revealed that AHG in saliva is strongly associated with T2D. [140, 148] Saliva samples have many distinct advantages over blood or urine in a diagnostic assay; (1) noninvasive collection, (2) easy sampling without special training or equipment, and (3) assessment of large scale of population for epidemiological study. The normal range of AHG level in saliva has been unknown at our best knowledge. The levels of other monosaccharide in saliva are approximately two-orders of magnitude less than in blood. Based on this idea, the development of an AHG assay with limit of detection as lower as 0.06 µg ml^{-1} is required.

Here, we demonstrated an CL assay for determining low levels of AHG in a simple handheld format, using two photon sensors, a multi-pixel photon counter (MPPC) and a photomultiplier tube (PMT) in a smartphone accessory. In our assay format, we first oxidized AHG in the sample with PROD to produce H_2O_2, and subsequently added luminol and HRP conjugated Streptavidin (HRP-Strepavidin). The light emitted from the luminol reaction, as shown in Figure 6.1, was detected using the two developed detectors. The limits of detection (LoD) of this assay for detecting AHG were 5 mg l^{-1} and 0.5 mg l^{-1} in a 10 µl sample using MPPC and PMT, respectively.

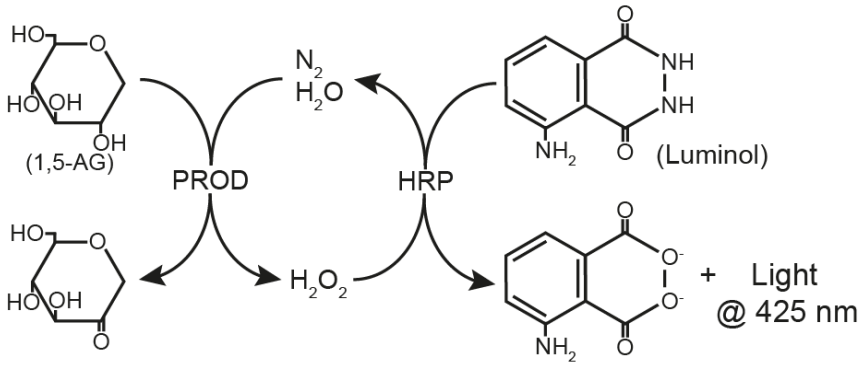

Figure 6.1 Reaction scheme for chemiluminescence-based detection of AHG.

6.2 Materials and Methods

Multi-pixel photon counter (MPPC). MPPC is one example of silicon photomultipliers (SiPMs). MPPC is a single-photon sensitive device that consists of multiple avalanche photodiode (APD) arrays on silicon (Si) substrate. APD is a highly sensitive semiconductor that exploits the photoelectric effect, converting light to electricity. MPPC is, in general, an analog output device, because all APD arrays are read in parallel to generate an integrated analog signal. We purchased the MPPC (Hamamatsu, C12662-350, analog output type), which is capable of detecting light in a dynamic range of 10^6 to 10^{10} photons within an area of 3 mm^2 in which 3,600 APDs are arrayed.

Analog-to-digital converter (ADC). To read MPPC analogue output, we developed a simple, inexpensive, and high-resolution analog-to-digital converter (ADC). ADC is a digitizer that converts analog signals to digitized values. A typical read range of ADC is 0 – 5 V or 4 – 20 mA for DC voltage or current, respectively. The bit resolution of ADC varies depending on manufacturers, but is generally in the range of 8 – 18 bit. We purchased ADC (Microchip, MCP3421), which supports up to 18-bit resolution and inter-integrated circuit (I^2C) interface**.** To send the digitized values from ADC to the computer or smart phone, a master device is required as a mediator. We used Arduino (Arduino, Nano Atmega328) as the master device for I^2C communication with ADC. The circuit diagram (Figure 6.2a) and ADC board (Figure 6.2b) were built. To program I^2C protocol for Arduino, we used the Arduino library <Wire.h>.

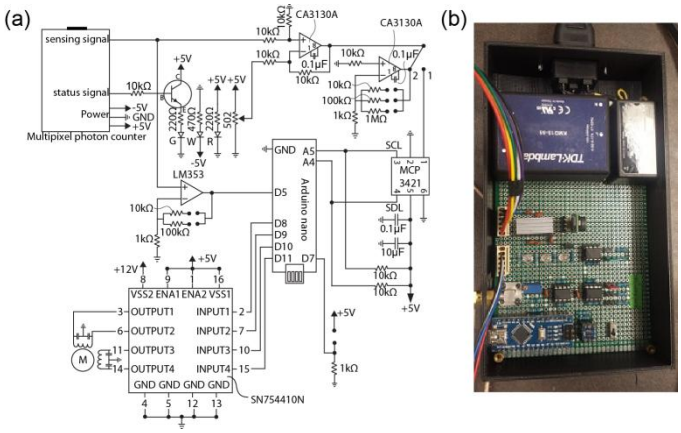

Figure 6.2 Complete circuit board development for MPPC system.

Sample loading and measurement system of MPPC. To develop a sample loading and measurement system for MPPC, a sample holder was fabricated using 3D modeling software (Autodesk, Inventor Professional 2015, student edition) and a 3D printer (Flashforge, Creator Pro), as shown in Figure 6.3. We designed a disposable cassette to which a liquid sample is added. To mount the cassette on the MPPC detector, a stepper motor (Nema 8, 8HS11-0204S) brings the slider to the cassette door, after which the cassette can be inserted by the user into the slider. The slider carrying the cassette moves back and stops at the location of APD array on MPPC. It is noted that the chemiluminescence reaction will be initiated, as soon as the sample is added to cassette. It is true that we missed some emitted light during inserting the cassette to the detector. However, it was not significant loss due to the durable reaction which generates readable light signals for more than one min.

During the reaction, the light generated by the chemiluminescence reaction passes through the glass window on the bottom of the cassette and reaches the APD array. The motor position is calibrated using an on-off sensor, which is located in the opposite side of the cassette door. When the slider hits the position-sensor, the sensor switches on to set

the motor position as zero. The stepper motor is controlled using a quadruple half-H driver (Texas Instruments, SN754410N). The circuit diagram for the motor driver is shown in Figure 6.2a. To program and implement the motor driver, we used the Arduino library <AccelStepper.h>.

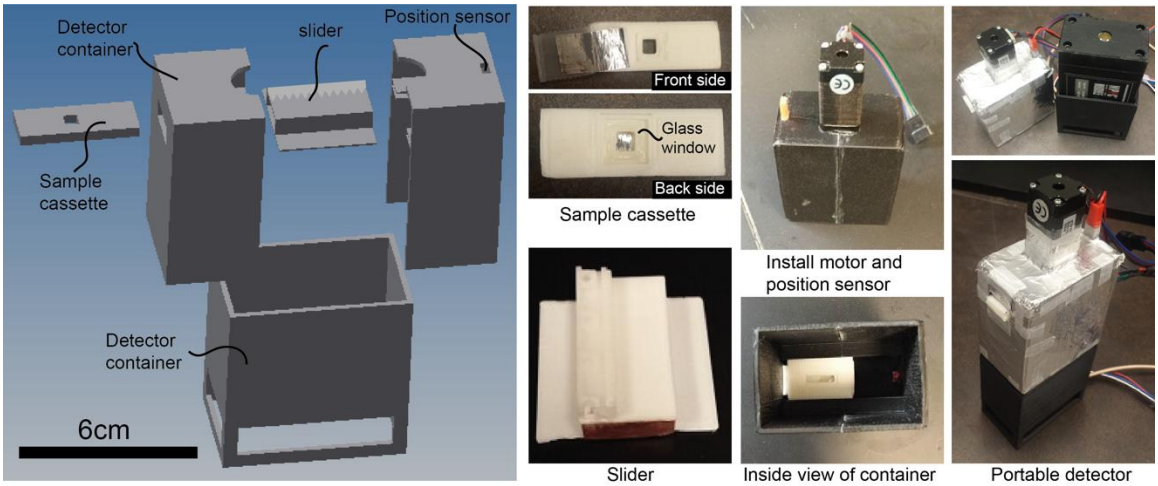

Figure 6.3 Solid work for sample holder and measurement system.

LabView Graphic user interface (GUI). To operate the MPPC measurement system and display sensed values of light intensity measured by MPPC, a graphical user interface (GUI) was developed using LabView 8.6 (National Instruments) as shown in Figure 6.4. One of the main functions of GUI is to send requests to and receive responses from the Arduino to operate the ADC and stepper motor. We adopted a serial interface for communication between the computer and the Arduino, because both LabView and Arduino support a serial interface and library. The commands for the serial communication are listed in Table 6.1.

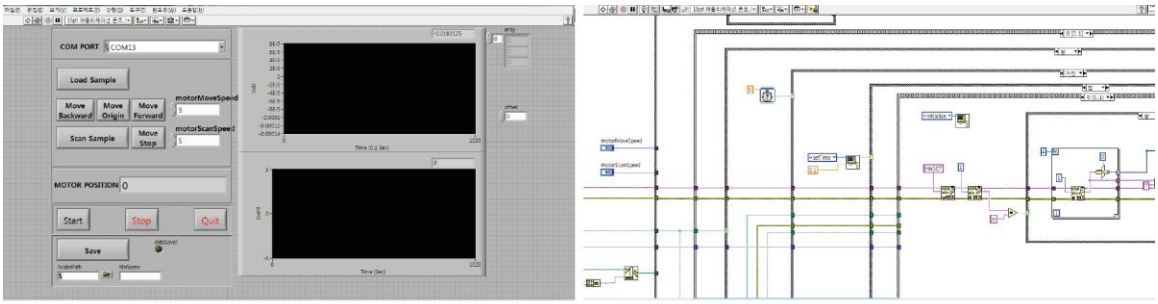

(a) LabView front panel (b) LabView block diagram

Figure 6.4 LabView GUI for data acquisition and MPPC operation.

Table 6.1 Protocols for serial communication

Command	Request code	Response code	Error code
ADC Request Data	HASOT	HXXXT	.
Motor Stop	HMSOT	HXT	.
Motor Load Sample	HMLOT	HXT	.
Motor Move Origin	HMOOT	HXT	.
Motor Move Forward	HMFOT	HXT	.
Motor Move Backward	HMBOT	HXT	.
Motor Move Scan	HMMXT	HXT	.

*X is 8bit number

Photomultiplier Tube (PMT). We developed another light intensity measurement system using photomultiplier (PMT), and compared its sensitivity with MPPC. This comparison will show how different type of detectors affects CL assay performance. The general differences between MPPC and PMT are listed in Table 6.2. PMT is a vacuum (~10 P^{-4}) tube consisting of input window, a photocathode, focusing electrodes, an electron multiplier (dynodes), and an anode (last dynode). In principle, light first passes through the input window of PMT and excites the electrons in the photocathode. The excited electrons are accelerated and focused by the focusing electrodes, efficiently arriving at the first dynode. As electrons hitting the dynode, it emits secondary electrons and thereby multiplies the electronic signal. This secondary emission is repeated at each of the successive dynodes. The multiplied secondary electrons are finally collected at the

anode, generating a readable signal. We purchased a photon counting head which embeds the comprehensive PMT and its operating circuit (Hamamatsu, H7421-50). PMT was capable of detecting light in a dynamic range of 80 to 10^8 photons.

Table 6.2 General comparison of MPPC and PMT

	MPPC	**PMT**
Material	solid-state	photocathode and dynode
Output	analog	digital
Sensitivity (limit of detection)	$10^6 – 10^{10}$ photon	$80 – 10^{18}$ photon
Physical Size	small	big
Cost	cheap	expensive

Pulse counter. PMT generates a pulse signal of width 30 ns and height 3.6 V. To count the number of output pulses, the 70 ns pulse-pair resolution requires a 14 MHz pulse counter. In practice, we found that a 8MHz pulse counter was sufficient for low level light, in which fewer than ~1000 pulses are generated per second. We used the Arduino, which has a 8MHz sampling speed, as the pulse counter. To program and implement the pulse counter, we used the Arduino library <FreqCount.h>.

Wireless data acquisition system. We developed a wireless data acquisition system based on smartphone and Wi-Fi networking. The smartphone was used as GUI for the displaying of sensed values and operating of PMT detector. After the Arduino counts PMT pulse output, the counted number is sent to the smartphone through Wi-Fi. To do this, a Wi-Fi interface is needed to communicate between the Arduino and the smartphone. The ESP8266 (Espressif) is a programmable WiFi module equipped with serial port and digital input/output pins. ESP8266 provides access point (AP) mode and webserver service for clients. Unlike Wi-Fi direct and Bluetooth, multiple clients can access the ESP8266 webserver at distances up to 1 km in AP mode. The ESP8266

receives data from the Arduino through the serial port and saves it in the ESP8266 RAM. Clients that connect to the AP of ESP8266 can request the web service provided by ESP8266 server. Next, the web server responds through the hypertext transfer protocol (HTTP) and transfers a document written by hypertext markup language (html) containing the saved data. To program the web server of the ESP8266, we used the Arduino integrated development environment (IDE). The circuit diagram for the wireless data acquisition is shown in Figure 6.5. We spent less than ten dollars to build the circuit board for the pulse counter and wireless data acquisition system.

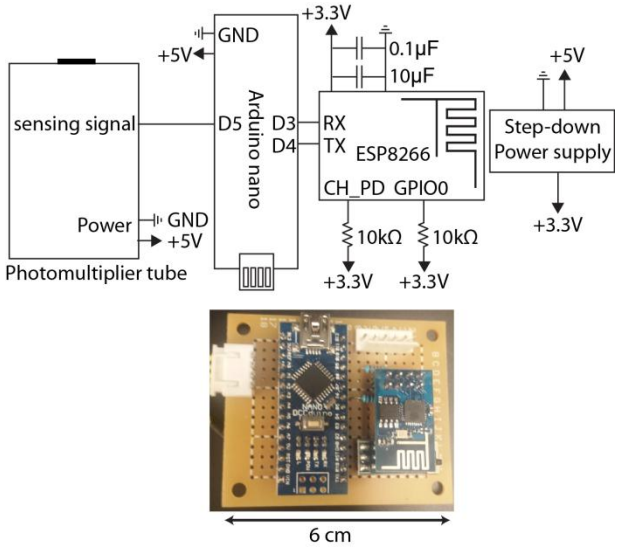

Figure 6.5 Circuit diagram (top figure) and board (bottom figure) for wireless data acquisition for PMT.

Android GUI. To display sensed signals and assay results, GUI was required and developed using Android studio, one of the Android application IDEs, as open-source software. Our Android application consists of two activities, measurement Activity and result Activity, as shown in Figure 6.6. The measurement Activity performs data acquisition, data visualization, and data save. After the measurement, the data is saved as a .txt file in AHG_Data folder in the external device storage of the smartphone. Users can

transfer the data file to computers through USB ports. The result Activity displays the final measurement results and stores history data in the AHG_Data folder.

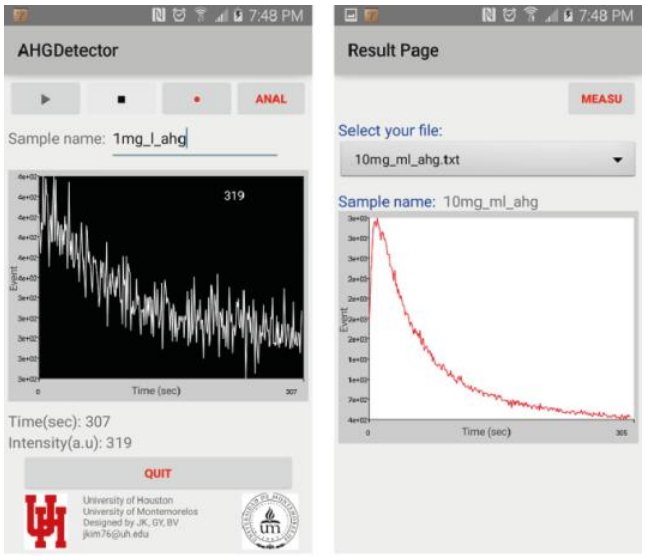

Figure 6.6 Android GUI for AHG measurement.

Optical path and cooling detector. Only a low fraction of the light generated from the chemiluminescence reaction reaches PMT sensor. To increase the amount of the captured light, we developed an optical set-up that collimates and focuses the chemiluminesce emission on the photon sensor using plano-convex lenses (ThorLabs, N-BK7 Plano-Convex Lens, Ø 1", f = 35.0 mm, AR Coating: 350-700 nm), as shown in Figure 6.7. The optical alignment was performed experimentally. To lower the dark photon count, the detector was cooled using a Peltier chip, whose temperature was controlled at 0℃ using a PID controller. The PID controller was programed in Arduino using the Arduino library <PID_v1.h>. The complete circuit diagram and PMT detector are shown in Figure 6.8.

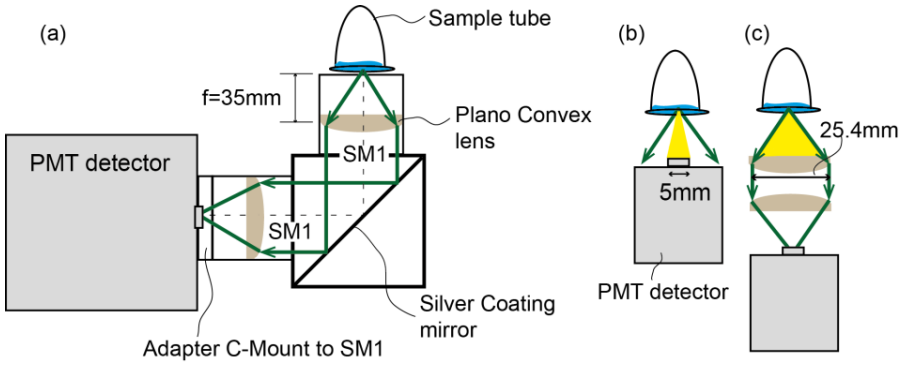

Figure 6.7 Optical set-up for increasing amount of captured light.

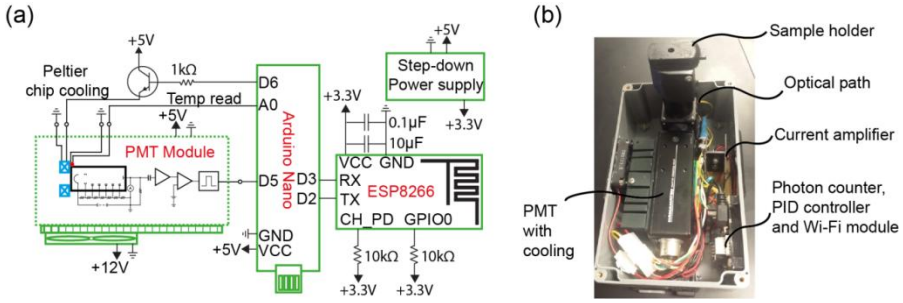

Figure 6.8 Complete PMT system with photon counter, sensor cooling and optical path adjustment.

6.3 Results and Discussions

Detection of hydrogen peroxide (H_2O_2). To demonstrate that MPPC or PMT systems described here are able to quantify the amount of hydrogen peroxide (H_2O_2) at low concentrations, we measured H_2O_2 at concentrations of 1.7 mM – 170 nM as a function of time using the assay (Figure 6.9). 30 µl luminol solution (Michigan Diagnostics, customized FEMTOFLOW) was mixed with 10 µl of H_2O_2 at various concentrations, and 10 µl of 1 µg ml^{-1} or 10 µg ml^{-1} HRP-Streptavidin; subsequently, the light intensity was measured using MPPC or PMT. The customized luminol solution does not contain H_2O_2. We detected H_2O_2 in the presence of two different concentrations of HRP-Streptavidin, such as 10 µg ml^{-1} and 1 µg ml^{-1}. If the concentration of HRP-Streptavidin is too high, the signal rapidly decayed to the background signal within 50

seconds. In this case, insufficiently quick loading of the sample in the cassette or holder can prevent the signal generated at the beginning of the reaction from being detected. Conversely, if the concentration of HRP-Streptavidin is too low, the reaction did not generate sufficient light for detection using our system. The light signal decreased with increasing time, due to consumption of H_2O_2 which is reduced in the chemiluminescence reaction. The decay rate of intensity appeared faster with HRP-Streptavidin at 10 μg ml^{-1} than 1 μg ml^{-1}; the reaction rate is a function of the concentration of HRP-Streptavidin. The maximum peak of the light intensities was proportional to the concentration of H_2O_2 (Figure 6.10).

The MPPC detector has the noise level of a single bit resolution which is 0.0625 mV. The MPPC detector for measurement of 17 μM H_2O_2 showed the sensed intensities of 0.75 mV and 1.125 mV using 1 μg ml^{-1} and 10 μg ml^{-1} HRP-Streptavidin, respectively. These values were one order of magnitude higher than the noise signal, clearly distinct from noise level (Figure 6.10, left). However, for measurement of 1.7 μM H_2O_2, the light intensities of MPPC fell into the noise level. Thus, we determined 17 μM as the limit of detection (LoD) of H_2O_2 for our MPPC system.

The noise level of PMT detector was around 300 (dark count) ± 20 (signal fluctuation noise). The dark count is a constant background generated by thermal noise. We controlled the temperature of the PMT with set-point at 0 ˚C. However, we could not completely remove the dark count. For measurement of 1.7 μM H_2O_2 using the PMT detector, the light intensities were detected, and one order of magnitude higher than the level of the signal fluctuation noise, clearly distinct from the background signal. Thus, we determined 1.7 μM as the limit of detection (LoD) of H_2O_2 for MPPC. The developed

PMT was approximately 10-times more sensitive than the MPPC for the detection of H_2O_2.

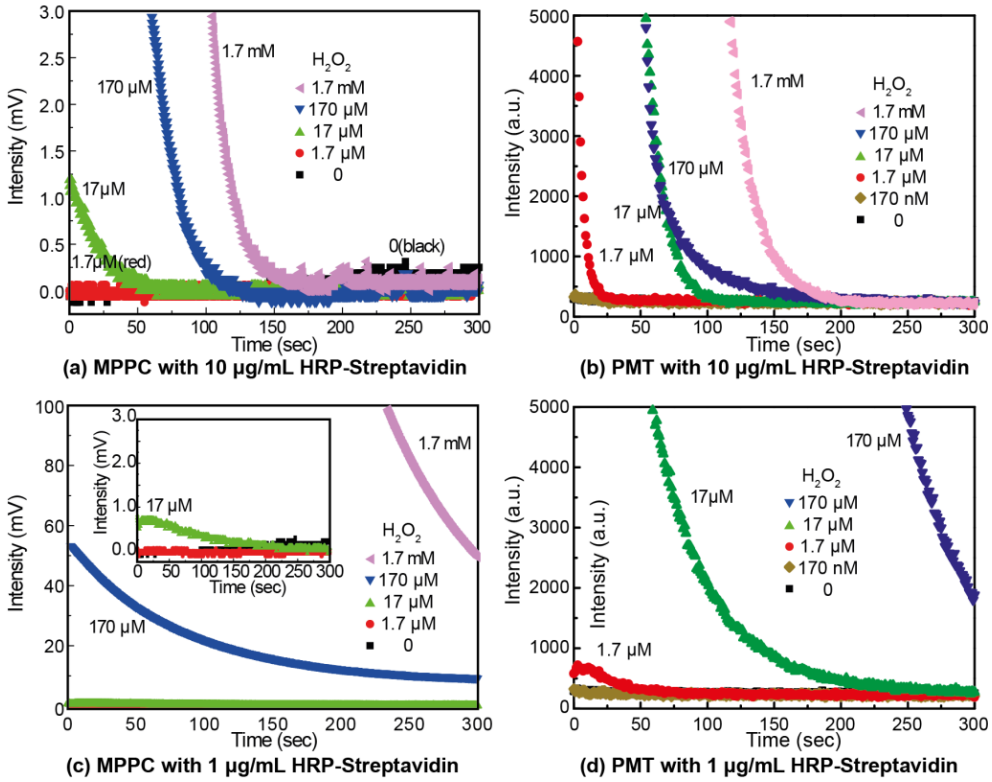

Figure 6.9 Detection of H_2O_2 using chemiluminescence assay.

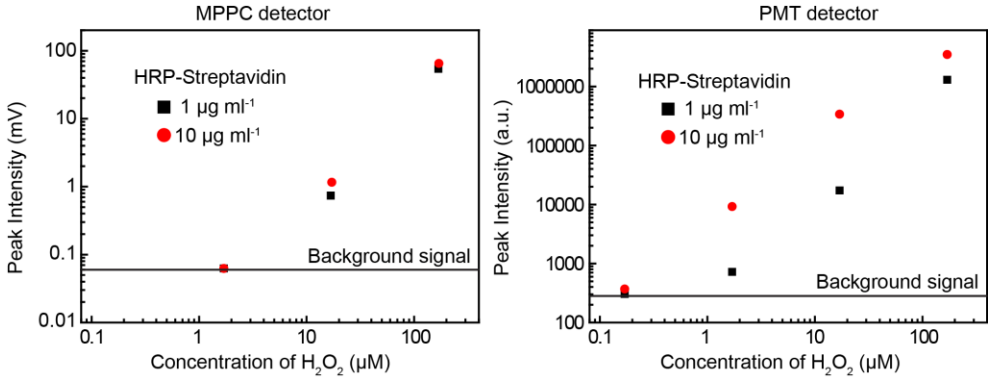

Figure 6.10 Measurement of H_2O_2 represented by peak sensed intensities.

Detection of AHG using MPPC or PMT. To evaluate the sensitivity of the MPPC and PMT for detecting low levels of AHG, we measured AHG at various concentrations

(50 – 0.2 mg l^{-1}) using the chemiluminescence assay. 10µL AHG was mixed with 10 µL of 1 mg ml^{-1} PROD to produce H_2O_2 for 5 min at room temperature. After the reaction of PROD and AHG, 30µL luminol solution and 10µL of 1 µg ml^{-1} HRP-Streptavidin were added to the AHG sample solution, and the resulting light intensities were then measured using MPPC or PMT. The light intensities decreased with increasing time (Figure 6.11), due to the consumption of H_2O_2 in the chemiluminescence reaction. The peaks of light intensities were proportional to AHG concentrations (Figure 6.11). Similarly, the observed intensity levels were compared to the noise levels, the limits of detection (LoD) of this assay were 5 mg l^{-1} and 0.5 mg l^{-1} AHG in a 10 µl sample using MPPC and PMT, respectively. The PMT system is ten-fold more sensitive than MPPC for detection of AHG. The sensitivity difference between MPPC and PMT is consistent with the result of H_2O_2 detection.

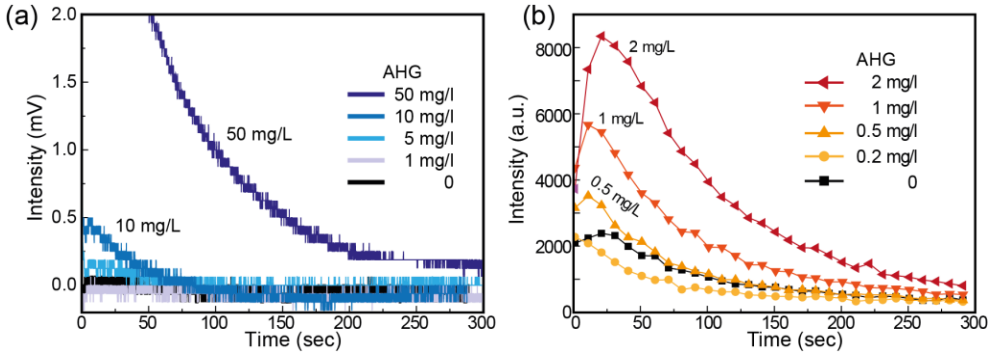

Figure 6.11 Detection of AHG using chemiluminescence assay.

6.4 Conclusions

We developed two different, sensitive, hand-tile light detectors using MPPC and PMT sensors and demonstrated a CL assay for detecting low levels of AHG using a combination of enzymatic reactions. In this enzymatic system, AHG is oxidized to produce H_2O_2 as the reporter molecules. To detect H_2O_2, luminol was used to generate

light in the presence of HRP-Streptavidin. Even if the light intensity was proportional to the AHG concentration, the limit of detection (LoD) of this assay was determined due to detector sensitivity as 5 mg l^{-1} and 0.5 mg l^{-1} in a 10 µl sample using MPPC and PMT, respectively. The PMT system was ten-times more sensitive than the MPPC for detection of AHG, proving that assay performance can be affected by detector capability and sensitivity. The sensitivity of MPPC system can be improved by designing and adjusting the light path to maximize the light to reach the sensor. An MPPC is cheaper and simpler to be manufactured than a PMT, enabling an affordable price in the market. A PMT sensor is the most feasible way to translate this ultra-sensitive handheld device as a PoC diagnostic device. The price of the PMT system can go down by using cheap electronic components, such as Arduino, and ESP8266 WiFi module. Although with the present setup we could not achieve an LoD of 0.06 mg/l AHG (as clinically demanded) the PMT shows a similar LoD with HPLC. [144]

Sensitive detection of light is frequently required in PoC applications, including our phage LFA assay described in Chapter 2, that uses light as a visual read-out; these applications demand light detectors that are sensitive yet also portable, simple and cheap. So we envision that the developed detectors seem promising for a variety of other light emitting assays, such as a fluorescence assay with optical filters, and phosphor assay.[96], [97]

Chapter 7 Summary and Future Work

The focus of this dissertation includes (1) development of the phage reporter used in ultra-sensitive LFAs, (2) characterization of binding modes of the phage reporter in the glass fiber membrane, (3) investigation of binding efficiency of the phage reporter with various morphology and local flow regimes, (4) genome sequencing of temperature-tolerant mutant phage, and (5) development of ultra-sensitive light detectors. This work is an effort towards the development of ultra-sensitive PoC diagnostics.

7.1. Overall Conclusions of this work

Bacteriophage nanoparticles were explored as a promising reporter for use in ultra-sensitive LFAs. The functional M13 phage reporters were developed and demonstrated for the detection of MS2 virus. The phage reporter exhibited significant improvement of sensitivity in LFAs compared to conventional gold nanoparticles, and individual reporter were resolved using standard fluorescence microscopy.

We postulated the shape of the reporter phage also influenced the LoD of the assay. To test the postulation, the binding modes of M13 were investigated in a simple model LFA. The resulting mechanisms revealed that the elongated shape of M13 phage led to reorientation on the glass fiber surfaces, increasing binding interactions and enhancing capture efficiency.

We investigated the other assay parameters that further influence binding efficiency. The binding reaction is characterized by the probability of interaction between phage and fibers in the membrane. This idea revealed that the long size and high flux of phage increased the phages's encounter chance to fibers, enhancing binding efficiency.

The stability and durability of the phage reporters are two of the most important issues when translating this assay to a real-world setting. The selection and growing of the surviving phage in extreme conditions is a simple method to enhance the properties of phage particles without any chemical or physical treatments. To understand the mechanism of the enhancement, the investigation of mutant genome combined with next-generation sequencing technology and bioinformatics analyses was a very effective strategy for identifying mutations in nucleotides; we were able to sequence seven phage samples, six mutants and one parental phage in a single run, dramatically reducing sequencing cost and time. We also enabled to recover and sequence the whole genome of a phage owing to enormous sequence readout. However, our sequencing results were controversial yet, we suggest three potential mechanisms for the apparent increase in temperature tolerance: gene replication enhancement (due to mutations in gp2), production of miniphage, and mutations in the p7 coat protein.

Sensitive detection of light is frequently required in PoC applications, including our phage LFA. The features of PoC devices are user-friendly, and handheld system. The miniaturization for the phage LFA is feasible, equipped with portable, ultra-sensitive detectors. We developed and demonstrated the MPPC and PMT photon detectors coupled with a smartphone accessory for determining low levels of AHG using a chemiluminescence enzymatic assay. The assay result was affected by detector performance; the PMT detector exhibited a ten-time better sensitivity than the MPPC in the assay. We envision that the developed detectors can be applied to the phage LFA by inserting an appropriate light source and optical filters, as well as in a variety of other light –based assays.

7.2. Outlook and future challenges

In phage LFAs, the binding efficiency of phage depended significantly on the interactions with the fibers. To improve the interaction, we can also consider tuning of the pore diameter of the membrane. The correlation of pore size, flow rate and binding efficiency may give some ideas to design an optimal structure of membranes that maximize capturing events. However, there are still many other assay parameters that influence the assay performance, such as binding affinity, mono/multivalency, available binding sites and surface energy, etc. If necessary, it might be useful to design simple experimental set-up for investigation of the assay parameters, separately and independently.

The flow experiments in phage LFA required index-matching to ensure transparency of membrane materials without affecting binding affinity. The poor index-matching leads to low quality of imaging or bad binding results. For the biotin and neutravidin interaction, the developed index-matching solution works well in these experiments. However, this specific solution may not work for other antigen-antibody interactions. Moreover, the use of index-matching could be useful in the colorimetric assay as well.

Even though the fluor labeled phage is detectable at a single phage level, it required a very strong excitation light source and a very sensitive camera. The miniaturization of the fluorescent phage assay still looks promising, but challenges remain in the development of the detection system of the required specifications.

References

1. Giljohann, D. A.; Mirkin, C. A., Drivers of Biodiagnostic Development. *Nature* **2009,** *462* (7272), 461-464.

2. Douketis, J. D., Patient Self-Monitoring of Oral Anticoagulant Therapy: Potential Benefits and Implications for Clinical Practice. *American journal of cardiovascular drugs : drugs, devices, and other interventions* **2001,** *1* (4), 245-51.

3. Laurence, C. O.; Gialamas, A.; Bubner, T.; Yelland, L.; Willson, K.; Ryan, P.; Beilby, J.; Point Care Testing Gen, P., Patient Satisfaction with Point-Of-Care Testing in General Practice. *British Journal of General Practice* **2010,** *60* (572).

4. Peeling, R. W.; Holmes, K. K.; Mabey, D.; Ronald, A., Rapid Tests for Sexually Transmitted Infections (Stis): The Way Forward. *Sexually Transmitted Infections* **2006,** *82*, V1-V6.

5. Chin, C. D.; Linder, V.; Sia, S. K., Commercialization of Microfluidic Point-of-Care Diagnostic Devices. *Lab on a Chip* **2012,** *12* (12), 2118-2134.

6. Gubala, V.; Harris, L. F.; Ricco, A. J.; Tan, M. X.; Williams, D. E., Point of Care Diagnostics: Status and Future. *Analytical Chemistry* **2012,** *84* (2), 487-515.

7. Posthuma-Trumpie, G. A.; Korf, J.; van Amerongen, A., Lateral Flow (Immuno) Assay: Its strengths, Weaknesses, Opportunities and Threats. A Literature Survey. *Analytical and Bioanalytical Chemistry* **2009,** *393* (2), 569-582.

8. Yetisen, A. K.; Akram, M. S.; Lowe, C. R., Paper-Based Microfluidic Point-of-Care Diagnostic Devices. *Lab on a Chip* **2013,** *13* (12), 2210-2251.

9. Gordon, J.; Michel, G., Analytical Sensitivity Limits for Lateral Flow Immunoassays. *Clinical Chemistry* **2008,** *54* (7), 1250-1251.

10. Uyeki, T. M.; Prasad, R.; Vukotich, C.; Stebbins, S.; Rinaldo, C. R.; Ferng, Y.-h.; Morse, S. S.; Larson, E. L.; Aiello, A. E.; Davis, B.; Monto, A. S., Low Sensitivity of Rapid Diagnostic Test for Influenza. *Clinical Infectious Diseases* **2009,** *48* (9), E89-E92.

11. Izzo, M. M.; Kirkland, P. D.; Gu, X.; Lele, Y.; Gunn, A. A.; House, J. K., Comparison of Three Diagnostic Techniques for Detection of Rotavirus and Coronavirus in Calf Faeces in Australia. *Australian Veterinary Journal* **2012,** *90* (4), 122-129.

12. Li, Y.; Hou, L.; Ye, J.; Liu, X.; Dan, H.; Jin, M.; Chen, H.; Cao, S., Development of A Convenient Immunochromatographic Strip for the Diagnosis of Infection with Japanese Encephalitis Virus in Swine. *Journal of Virological Methods* **2010,** *168* (1-2), 51-56.

13. Mashayekhi, F.; Chiu, R. Y. T.; Le, A. M.; Chao, F. C.; Wu, B. M.; Kamei, D. T., Enhancing the Lateral-Flow Immunoassay for Viral Detection using an Aqueous Two-Phase Micellar System. *Analytical and Bioanalytical Chemistry* **2010,** *398* (7-8), 2955-2961.

14. Song, C.; Li, J.; Liu, J.; Liu, Q., Simple Sensitive Rapid Detection of Escherichia Coli O157:H7 in Food Samples by Label-Free Immunofluorescence Strip Sensor. *Talanta* **2016,** *156-157*, 42-7.

15. Wieser, A.; Berting, A.; Medek, C.; Poelsler, G.; Kreil, T. R., The Evolution of Down-Scale Virus Filtration Equipment for Virus Clearance Studies. *Biotechnology and Bioengineering* **2015,** *112* (3), 633-637.

16. Juntunen, E.; Myyrylainen, T.; Salminen, T.; Soukka, T.; Pettersson, K., Performance of Fluorescent Europium(Iii) Nanoparticles and Colloidal Gold Reporters in Lateral Flow Bioaffinity Assay. *Analytical Biochemistry* **2012,** *428* (1), 31-38.

17. Corstjens, P.; de Dood, C. J.; van der Ploeg-van Schip, J. J.; Wiesmeijer, K. C.; Riuttamaki, T.; van Meijgaarden, K. E.; Spencer, J. S.; Tanke, H. J.; Ottenhoff, T. H. M.; Geluk, A., Lateral Flow Assay for Simultaneous Detection of Cellular- and Humoral Immune Responses. *Clinical Biochemistry* **2011,** *44* (14-15), 1241-1246.

18. Ambrosi, A.; Castaneda, M. T.; Killard, A. J.; Smyth, M. R.; Alegret, S.; Merkoci, A., Double-Codified Gold Nanolabels for Enhanced Immunoanalysis. *Analytical Chemistry* **2007,** *79* (14), 5232-5240.

19. Edwards, K. A.; Baeumner, A. J., Dna-Oligonucleotide Encapsulating Liposomes as a Secondary Signal Amplification Means. *Analytical Chemistry* **2007,** *79* (5), 1806-1815.

20. Mason, J. T.; Xu, L. X.; Sheng, Z. M.; O'Leary, T. J., A Liposome-Pcr Assay for The Ultrasensitive Detection of Biological Toxins. *Nature Biotechnology* **2006,** *24* (5), 555-557.

21. Thaxton, C. S.; Elghanian, R.; Thomas, A. D.; Stoeva, S. I.; Lee, J. S.; Smith, N. D.; Schaeffer, A. J.; Klocker, H.; Horninger, W.; Bartsch, G.; Mirkin, C. A., Nanoparticle-Based Bio-Barcode Assay Redefines "Undetectable" Psa And Biochemical Recurrence after Radical Prostatectomy. *Proceedings of the National Academy of Sciences of the United States of America* **2009,** *106* (44), 18437-18442.

22. Domaille, D. W.; Lee, J. H.; Cha, J. N., High Density Dna Loading On The M13 Bacteriophage Provides Access to Colorimetric and Fluorescent Protein Microarray Biosensors. *Chemical Communications* **2013,** *49* (17), 1759-1761.

23. Parolo, C.; de la Escosura-Muniz, A.; Merkoci, A., Enhanced Lateral Flow Immunoassay using Gold Nanoparticles Loaded with Enzymes. *Biosensors & Bioelectronics* **2013,** *40* (1), 412-416.

24. Ahn-Yoon, S.; DeCory, T. R.; Baeumner, A. J.; Durst, R. A., Ganglioside-Liposome Immunoassay for the Ultrasensitive Detection of Cholera Toxin. *Analytical Chemistry* **2003,** *75* (10), 2256-2261.

25. Chen, C.; Wu, J., A Fast and Sensitive Quantitative Lateral Flow Immunoassay for Cry1ab Based on a Novel Signal Amplification Conjugate. *Sensors* **2012,** *12* (9), 11684-11696.

26. Kim, H.-J.; Rossotti, M. A.; Ahn, K. C.; Gonzalez-Sapienza, G. G.; Gee, S. J.; Musker, R.; Hammock, B. D., Development of a Noncompetitive Phage Anti-Immunocomplex Assay for Brominated Diphenyl Ether 47. *Analytical Biochemistry* **2010,** *401* (1), 38-46.

27. Kim, H.-J.; Ahn, K. C.; Gonzalez-Techera, A.; Gonzalez-Sapienza, G. G.; Gee, S. J.; Hammock, B. D., Magnetic Bead-Based Phage Anti-Immunocomplex Assay (Phaia) for the Detection of the Urinary Biomarker 3-Phenoxybenzoic Acid to Assess Human Exposure to Pyrethroid Insecticides. *Analytical Biochemistry* **2009,** *386* (1), 45-52.

28. Douglas, T.; Young, M., Viruses: Making Friends with Old Foes. *Science* **2006,** *312* (5775), 873-875.

29. Nash, M. A.; Waitumbi, J. N.; Hoffman, A. S.; Yager, P.; Stayton, P. S., Multiplexed Enrichment and Detection of Malarial Biomarkers using a Stimuli-Responsive Iron Oxide and Gold Nanoparticle Reagent System. *Acs Nano* **2012,** *6* (8), 6776-6785.

30. Mashayekhi, F.; Le, A. M.; Nafisi, P. M.; Wu, B. M.; Kamei, D. T., Enhancing the Lateral-Flow Immunoassay for Detection of Proteins using an Aqueous Two-Phase Micellar System. *Analytical and Bioanalytical Chemistry* **2012,** *404* (6-7), 2057-2066.

31. Lutz, B.; Liang, T.; Fu, E.; Ramachandran, S.; Kauffman, P.; Yager, P., Dissolvable Fluidic Time Delays for Programming Multi-Step Assays in Instrument-Free Paper Diagnostics. *Lab on a Chip* **2013,** *13* (14), 2840-2847.

32. Sharp, T. M.; Gaul, L.; Muehlenbachs, A.; Hunsperger, E.; Bhatnagar, J.; Lueptow, R.; Santiago, G. A.; Munoz-Jordan, J. L.; Blau, D. M.; Ettestad, P.; Bissett, J. D.; Ledet, S. C.; Zaki, S. R.; Tomashek, K. M., Fatal Hemophagocytic Lymphohistiocytosis Associated with Locally Acquired Dengue Virus Infection - New Mexico and Texas, 2012. *Mmwr-Morbidity and Mortality Weekly Report* **2014,** *63* (3).

33. Gire, S. K.; Goba, A.; Andersen, K. G.; Sealfon, R. S. G.; Park, D. J.; Kanneh, L.; Jalloh, S.; Momoh, M.; Fullah, M.; Dudas, G.; Wohl, S.; Moses, L. M.; Yozwiak, N. L.; Winnicki, S.; Matranga, C. B.; Malboeuf, C. M.; Qu, J.; Gladden, A. D.; Schaffner, S. F.; Yang, X.; Jiang, P.-P.; Nekoui, M.; Colubri, A.; Coomber, M. R.; Fonnie, M.; Moigboi, A.; Gbakie, M.; Kamara, F. K.; Tucker, V.; Konuwa, E.; Saffa, S.; Sellu, J.; Jalloh, A. A.; Kovoma, A.; Koninga, J.; Mustapha, I.; Kargbo, K.; Foday, M.; Yillah, M.; Kanneh, F.; Robert, W.; Massally, J. L. B.; Chapman, S. B.; Bochicchio, J.; Murphy, C.; Nusbaum, C.; Young, S.; Birren, B.; Grant, D. S.; Scheiffelin, J. S.; Lander, E. S.; Happi, C.; Gevao, S. M.; Gnirke, A.; Rambaut, A.; Garry, R. F.; Khan, S. H.; Sabeti, P. C., Genomic Surveillance Elucidates Ebola Virus Origin And Transmission during the 2014 Outbreak. *Science* **2014,** *345* (6202), 1369-1372.

34. Bamrungsap, S.; Apiwat, C.; Chantima, W.; Dharakul, T.; Wiriyachaiporn, N., Rapid and Sensitive Lateral Flow Immunoassay for Influenza Antigen using Fluorescently-Doped Silica Nanoparticles. *Microchim Acta* **2014,** *181* (1-2), 223-230.

35. Battaglioli, G.; Nazarian, E. J.; Lamson, D.; Musser, K. A.; George, K. S., Evaluation of the RIDAQuick Norovirus Immunochromatographic Test Kit. *Journal of Clinical Virology* **2012,** *53* (3), 262-264.

36. Mellors, J. W.; Rinaldo, C. R.; Gupta, P.; White, R. M.; Todd, J. A.; Kingsley, L. A., Prognosis In Hiv-1 Infection Predicted by the Quantity of Virus in Plasma. *Science* **1996,** *272* (5265), 1167-1170.

37. Towner, J. S.; Rollin, P. E.; Bausch, D. G.; Sanchez, A.; Crary, S. M.; Vincent, M.; Lee, W. F.; Spiropoulou, C. F.; Ksiazek, T. G.; Lukwiya, M.; Kaducu, F.; Downing, R.; Nichol, S. T., Rapid Diagnosis of Ebola Hemorrhagic Fever by Reverse Transcription-Pcr in an Outbreak Setting and Assessment of Patient Viral Load as A Predictor Of Outcome. *Journal of Virology* **2004,** *78* (8), 4330-4341.

38. de la Cruz-Hernandez, S. I.; Flores-Aguilar, H.; Gonzalez-Mateos, S.; Lopez-Martinez, I.; Alpuche-Aranda, C.; Ludert, J. E.; del Angel, R. M., Determination of Viremia and Concentration of Circulating Nonstructural Protein 1 In Patients Infected with Dengue Virus in Mexico. *American Journal of Tropical Medicine and Hygiene* **2013,** *88* (3), 446-454.

39. Mateu, M. G., Virus Engineering: Functionalization and Stabilization. *Protein Engineering Design & Selection* **2011,** *24* (1-2), 53-63.

40. Yang, S. H.; Chung, W.-J.; McFarland, S.; Lee, S.-W., Assembly of Bacteriophage into Functional Materials. *Chemical Record* **2013,** *13* (1), 43-59.

41. Zhang, H.; Xu, Y.; Huang, Q.; Yi, C.; Xiao, T.; Li, Q., Natural Phage Nanoparticle-Mediated Real-Time Immuno-Pcr for Ultrasensitive Detection of Protein Marker. *Chemical Communications* **2013,** *49* (36), 3778-3780.

42. Citorik, R. J.; Mimee, M.; Lu, T. K., Bacteriophage-Based Synthetic Biology for the Study of Infectious Diseases. *Current opinion in microbiology* **2014,** *19*, 59-69.

43. Litvinov, J.; Hagstrom, A. E. V.; Lopez, Y.; Adhikari, M.; Kourentzi, K.; Strych, U.; Monzon, F. A.; Foster, W.; Cagle, P. T.; Willson, R. C., Ultrasensitive Immuno-Detection using Viral Nanoparticles with Modular Assembly using Genetically-Directed Biotinylation. *Biotechnology Letters* **2014,** *36* (9), 1863-1868.

44. Kim, H.-J.; McCoy, M.; Gee, S. J.; Gonzalez-Sapienza, G. G.; Hammock, B. D., Noncompetitive Phage Anti-Immunocomplex Real-Time Polymerase Chain Reaction for Sensitive Detection of Small Molecules. *Analytical Chemistry* **2011,** *83* (1), 246-253.

45. Brasino, M.; Lee, J. H.; Cha, J. N., Creating Highly Amplified Enzyme-Linked Immunosorbent Assay Signals from Genetically Engineered Bacteriophage. *Analytical Biochemistry* **2015,** *470*, 7-13.

46. Adhikari, M.; Dhamane, S.; Hagstrom, A. E. V.; Garvey, G.; Chen, W. H.; Kourentzi, K.; Strych, U.; Willson, R. C., Functionalized Viral Nanoparticles as Ultrasensitive Reporters in Lateral Flow Assays. *Abstracts of Papers of the American Chemical Society* **2014,** *247*.

47. Goodridge, L.; Chen, J. R.; Griffiths, M., Development And Characterization of a Fluorescent-Bacteriophage Assay for Detection of Escherichia Coli O157 : H7. *Applied and Environmental Microbiology* **1999,** *65* (4), 1397-1404.

48. Goodridge, L.; Chen, J. R.; Griffiths, M., The Use of a Fluorescent Bacteriophage Assay For Detection of Escherichia Coli O157 : H7 in Inoculated Ground Beef and Raw Milk. *International Journal of Food Microbiology* **1999,** *47* (1-2), 43-50.

49. Namura, M.; Hijikata, T.; Miyanaga, K.; Tanji, Y., Detection of Escherichia Coli with Fluorescent Labeled Phages That Have a Broad Host Range to E-Coli in Sewage Water. *Biotechnology Progress* **2008,** *24* (2), 481-486.

50. Carrico, Z. M.; Farkas, M. E.; Zhou, Y.; Hsiao, S. C.; Marks, J. D.; Chokhawala, H.; Clark, D. S.; Francis, M. B., N-Terminal Labeling of Filamentous Phage to Create Cancer Marker Imaging Agents. *Acs Nano* **2012,** *6* (8), 6675-6680.

51. Tanji, Y.; Furukawa, C.; Na, S. H.; Hijikata, T.; Miyanaga, K.; Unno, H., Escherichia Coli Detection by Gfp-Labeled Lysozyme-Inactivated T4 Bacteriophage. *Journal of Biotechnology* **2004,** *114* (1-2), 11-20.

52. Awais, R.; Fukudomi, H.; Miyanaga, K.; Unno, H.; Tanji, Y., A Recombinant Bacteriophage-Based Assay for the Discriminative Detection of Culturable and Viable but Nonculturable Escherichia Coli O157 : H7. *Biotechnology Progress* **2006,** *22* (3), 853-859.

53. Zeng, L.; Skinner, S. O.; Zong, C.; Sippy, J.; Feiss, M.; Golding, I., Decision Making at a Subcellular Level Determines the Outcome of Bacteriophage Infection. *Cell* **2010,** *141* (4), 682-691.

54. Han, J.-H.; Wang, M. S.; Das, J.; Sudheendra, L.; Vonasek, E.; Nitin, N.; Kennedy, I. M., Capture and Detection of T7 Bacteriophages on a Nanostructured Interface. *ACS Applied Materials & Interfaces* **2014,** *6* (7), 4758-4765.

55. Adiga, P. S. U.; Malladi, R.; Baxter, W.; Glaeser, R. M., A Binary Segmentation Approach for Boxing Ribosome Particles in Cryo Em Micrographs. *Journal of Structural Biology* **2004,** *145* (1-2), 142-151.

56. McBride, M. T.; Gammon, S.; Pitesky, M.; O'Brien, T. W.; Smith, T.; Aldrich, J.; Langlois, R. G.; Colston, B.; Venkateswaran, K. S., Multiplexed Liquid Arrays for Simultaneous Detection of Simulants of Biological Warfare Agents. *Analytical Chemistry* **2003,** *75* (8), 1924-1930.

57. Hu, J.; Wang, S.; Wang, L.; Li, F.; Pingguan-Murphy, B.; Lu, T. J.; Xu, F., Advances in Paper-Based Point-of-Care Diagnostics. *Biosensors & Bioelectronics* **2014,** *54*, 585-597.

58. Wei, Q.; Qi, H.; Luo, W.; Tseng, D.; Ki, S. J.; Wan, Z.; Gorocs, Z.; Bentolila, L. A.; Wu, T.-T.; Sun, R.; Ozcan, A., Fluorescent Imaging of Single Nanoparticles and Viruses on a Smart Phone. *Acs Nano* **2013,** *7* (10), 9147-9155.

59. Vashist, S. K.; Mudanyali, O.; Schneider, E. M.; Zengerle, R.; Ozcan, A., Cellphone-Based Devices for Bioanalytical Sciences. *Analytical and Bioanalytical Chemistry* **2014,** *406* (14), 3263-3277.

60. Scholle, M. D.; Kriplani, U.; Pabon, A.; Sishtla, K.; Glucksman, M. J.; Kay, B. K., Mapping Protease Substrates by using a Biotinylated Phage Substrate Library. *Chembiochem* **2006,** *7* (5), 834-838.

61. Peng, T.; Balijepalli, A.; Gupta, S. K.; LeBrun, T., Algorithms for On-line Monitoring of Micro Spheres in an Optical Tweezers-based Assembly Cell. *Journal of Computing and Information Science in Engineering* **2007,** *7* (4), 330-338.

62. Yang, L.; Wu, X.; Zhao, D.; Li, H.; Zhai, J. In *An Improved Prewitt Algorithm for Edge Detection Based on Noised Image*, Image and Signal Processing (CISP), 2011 4th International Congress on, 15-17 Oct. 2011; 2011; pp 1197-1200.

63. Gonzalez, R. C. W., R. E.; Eddins, S. L., *Digital Image Processing Using MATLAB*. 1st ed.; Pearson Education: New Jersey, 2004.

64. Malladi, R.; Ravve, I., Fast difference Schemes for Edge Enhancing Beltrami Flow. In *Computer Vison - Eccv 2002, Pt 1*, Heyden, A.; Sparr, G.; Nielsen, M.; Johansen, P., Eds. 2002; Vol. 2350, pp 343-357.

65. Leong, F.; Brady, M.; McGee, J. O., Correction of Uneven Illumination (Vignetting) in Digital Microscopy Images. *Journal of Clinical Pathology* **2003,** *56* (8), 619-621.

66. Adams, R.; Bischof, L., SEEDED REGION GROWING. *Ieee Transactions on Pattern Analysis and Machine Intelligence* **1994,** *16* (6), 641-647.

67. Adiga, P. S.; Malladi, R.; Baxter, W.; Glaeser, R. M., A Binary Segmentation Approach for Boxing Ribosome Particles in Cryo EM Micrographs. *J. Struct. Biol.* **2004,** *145* (1-2), 142-151.

68. Malladi, R.; Ravve, I., Fast Difference Schemes for Edge Enhancing Beltrami Flow. In *Computer Vision — ECCV 2002*, Heyden, A.; Sparr, G.; Nielsen, M.; Johansen, P., Eds. Springer Berlin Heidelberg: 2002; Vol. 2350, pp 343-357.

69. Dillencourt, M. B.; Samet, H.; Tamminen, M., A General-Approach to Connected-Component Labeling for Arbitrary Image Representations. *J. ACM* **1992,** *39* (2), 253-280.

70. Martinez, A. W.; Phillips, S. T.; Whitesides, G. M.; Carrilho, E., Diagnostics for the Developing World: Microfluidic Paper-Based Analytical Devices. *Analytical Chemistry* **2010,** *82* (1), 3-10.

71. Xu, Y.; Liu, Y.; Wu, Y.; Xia, X.; Liao, Y.; Li, Q., Fluorescent Probe-Based Lateral Flow Assay for Multiplex Nucleic Acid Detection. *Analytical Chemistry* **2014,** *86* (12), 5611-5614.

72. Ozcan, A., Mobile Phones Democratize and Cultivate Next-Generation Imaging, Diagnostics and Measurement Tools. *Lab on a Chip* **2014,** *14* (17), 3187-3194.

73. PNNL Smartphone Microscope. http://availabletechnologies. pnnl.gov/technology.asp?id=393 (accessed Oct 13, 2014).

74. Posthuma-Trumpie, G. A.; Korf, J.; van Amerongen, A., Lateral Flow (Immuno)assay: Its Strengths, Weaknesses, Opportunities and Threats. A Literature Survey. *Analytical and bioanalytical chemistry* **2009,** *393* (2), 569-582.

75. Chinnasamy, T.; Segerink, L. I.; Nystrand, M.; Gantelius, J.; Svahn, H. A., A Lateral Flow Paper Microarray for Rapid Allergy Point of Care Diagnostics. *The Analyst* **2014,** *139* (10), 2348-54.

76. (a) Li, X.; Lu, D.; Sheng, Z.; Chen, K.; Guo, X.; Jin, M.; Han, H., A Fast and Sensitive Immunoassay of Avian Influenza Virus based on Label-Free Quantum Dot Probe and Lateral Flow Test Strip. *Talanta* **2012,** *100* (C), 1-6; (b) Rohrman, B. A.; Leautaud, V.; Molyneux, E.; Richards-Kortum, R. R., A Lateral Flow Assay for Quantitative Detection of Amplified HIV-1 RNA. *Plos One* **2012,** *7* (9), e45611; (c) Vanithamani, S.; Shanmughapriya, S.; Narayanan, R.; Raja, V.; Kanagavel, M.; Sivasankari, K.; Natarajaseenivasan, K., Lipopolysaccharide Specific

Immunochromatography Based Lateral Flow Assay for Serogroup Specific Diagnosis of Leptospirosis in India. *Plos One* **2015,** *10* (9), e0137130.

77. (a) Cho, I.-H.; Irudayaraj, J., Lateral-Flow Enzyme Immunoconcentration for Rapid Detection of Listeria Monocytogenes. *Analytical and bioanalytical chemistry* **2013,** *405* (10), 3313-3319; (b) Singh, J.; Sharma, S.; Nara, S., Nanogold based lateral flow assay for the detection of Salmonella typhi in environmental water samples. *Anal Methods-Uk* **2015,** *7* (21), 9281-9288.

78. Ongagna-Yhombi, S. Y.; Corstjens, P.; Geva, E.; Abrams, W. R.; Barber, C. A.; Malamud, D.; Mharakurwa, S., Improved Assay to Detect Plasmodium Falciparum Using an Uninterrupted, Semi-Nested PCR and Quantitative Lateral Flow Analysis. *Malaria journal* **2013,** *12*, 74.

79. (a) Wang, Y.; Fill, C.; Nugen, S. R., Development of Chemiluminescent Lateral Flow Assay for the Detection of Nucleic Acids. *Biosensors* **2012,** *2* (1), 32-42; (b) Fang, Z.; Wu, W.; Lu, X.; Zeng, L., Lateral Flow Biosensor for DNA Extraction-Free Detection of Salmonella Based on Aptamer Mediated Strand Displacement Amplification. *Biosensors and Bioelectronics* **2014,** *56*, 192-7; (c) Terao, Y.; Takeshita, K.; Nishiyama, Y.; Morishita, N.; Matsumoto, T.; Morimatsu, F., Promising Nucleic Acid Lateral Flow Assay Plus pCR for Shiga Toxin-Producing Escherichia coli. *J Food Protect* **2015,** *78* (8), 1560-1568.

80. (a) Corstjens, P. L.; de Dood, C. J.; van der Ploeg-van Schip, J. J.; Wiesmeijer, K. C.; Riuttamaki, T.; van Meijgaarden, K. E.; Spencer, J. S.; Tanke, H. J.; Ottenhoff, T. H.; Geluk, A., Lateral Flow Assay for Simultaneous Detection of Cellular- and Humoral Immune Responses. *Clinical Biochemistry* **2011,** *44* (14-15), 1241-6; (b) Mashayekhi, F.;

Le, A.; Nafisi, P.; Wu, B.; Kamei, D., Enhancing the Lateral-Flow Immunoassay for Detection of Proteins Using an Aqueous Two-Phase Micellar System. *Analytical and bioanalytical chemistry* **2012,** *404* (6), 2057-2066; (c) Oh, Y. K.; Joung, H.-A.; Han, H. S.; Suk, H.-J.; Kim, M.-G., A Three-line lateral Flow Assay Strip for the Measurement of C-reactive Protein Covering a Broad Physiological Concentration Range in Human Sera. *Biosensors and Bioelectronics* **2014,** *61* (C), 285-289.

81. (a) Liu, C. Y.; Ma, W.; Gao, Z. Y.; Huang, J. Y.; Hou, Y.; Xu, C. L.; Yang, W. S.; Gao, M. Y., Upconversion luminescence nanoparticles-based lateral flow immunochromatographic assay for cephalexin detection. *J Mater Chem C* **2014,** *2* (45), 9637-9642; (b) Peng, T.; Zhang, F. S.; Yang, W. C.; Li, D. X.; Chen, Y.; Xiong, Y. H.; Wei, H.; Lai, W. H., Lateral-Flow Assay for Rapid Quantitative Detection of Clorprenaline Residue in Swine Urine. *J Food Protect* **2014,** *77* (10), 1824-9.

82. (a) Anfossi, L.; Baggiani, C.; Giovannoli, C.; Biagioli, F.; D'Arco, G.; Giraudi, G., Optimization of a lateral flow immunoassay for the ultrasensitive detection of aflatoxin M1 in milk. *Analytica chimica acta* **2013,** *772*, 75-80; (b) Anfossi, L.; Di Nardo, F.; Giovannoli, C.; Passini, C.; Baggiani, C., Increased Sensitivity of Lateral Flow Immunoassay for Ochratoxin A through Silver Enhancement. *Analytical and bioanalytical chemistry* **2013,** *405* (30), 9859-67.

83. Kwizera, R.; Nguna, J.; Kiragga, A.; Nakavuma, J.; Rajasingham, R.; Boulware, D. R.; Meya, D. B., Performance of Cryptococcal Antigen Lateral Flow Assay Using Saliva in Ugandans with CD4 < 100. *Plos One* **2014,** *9* (7), e103156.

84. Paterson, A. S.; Raja, B.; Garvey, G.; Kolhatkar, A.; Hagstrom, A. E.; Kourentzi, K.; Lee, T. R.; Willson, R. C., Persistent Luminescence Strontium Aluminate

Nanoparticles as Reporters in Lateral Flow Assays. *Analytical chemistry* **2014,** *86* (19), 9481-8.

85. Quesada-González, D.; Merkoci, A., Nanoparticle-based Lateral Flow Biosensors. *Biosensors and Bioelectronics* **2015,** *73* (C), 47-63.

86. Bruno, J. G., Application of DNA Aptamers and Quantum Dots to Lateral Flow Test Strips for Detection of Foodborne Pathogens with Improved Sensitivity versus Colloidal Gold. *Pathogens* **2014,** *3*, 341-355.

87. Liu, C. Y.; Jia, Q. J.; Yang, C. H.; Qiao, R. R.; Jing, L. H.; Wang, L. B.; Xu, C. L.; Gao, M. Y., Lateral Flow Immunochromatographic Assay for Sensitive Pesticide Detection by Using Fe3O4 Nanoparticle Aggregates as Color Reagents. *Analytical chemistry* **2011,** *83* (17), 6778-6784.

88. Corstjens, P. L.; Zuiderwijk, M.; Nilsson, M.; Feindt, H.; Sam Niedbala, R.; Tanke, H. J., Lateral-Flow and Up-Converting Phosphor Reporters to Detect Single-Stranded Nucleic Acids in a Sandwich-Hybridization Assay. *Analytical biochemistry* **2003,** *312* (2), 191-200.

89. Lin, R.; Skandarajah, A.; Gerver, R. E.; Neira, H. D.; Fletcher, D. A.; Herr, A. E., A lateral electrophoretic flow diagnostic assay. *Lab Chip* **2015,** *15* (6), 1488-1496.

90. Moghadam, B. Y.; Connelly, K. T.; Posner, J. D., Two Orders of Magnitude Improvement in Detection Limit of Lateral Flow Assays Using Isotachophoresis. *Analytical chemistry* **2015,** *87* (2), 1009-1017.

91. Rivas, L.; Medina-Sánchez, M.; de la Escosura-Muñiz, A.; Merkoci, A., Improving Sensitivity of Gold Nanoparticle-based Lateral Flow Assays by Using Wax-Printed Pillars as Delay Barriers of Microfluidics. *Lab Chip* **2014,** *14*, 4406-4414.

92. (a) Barnett, J.; Wraith, P.; Kiely, J.; Persad, R.; Hurley, K.; Hawkins, P.; Luxton, R., An Inexpensive, Fast and Sensitive Quantitative Lateral Flow Magneto-Immunoassay for Total Prostate Specific Antigen. *Biosensors* **2014,** *4* (3), 204-220; (b) Orlov, A. V.; Bragina, V. A.; Nikitin, M. P.; Nikitin, P. I., Rapid dry-reagent immunomagnetic biosensing platform based on volumetric detection of nanoparticles on 3D structures. *Biosensors & bioelectronics* **2016,** *79*, 423-9.

93. Swanson, C.; D'Andrea, A., Lateral Flow Assay with Near-Infrared Dye for Multiplex Detection. *Clinical Chemistry* **2013,** *59* (4), 641-648.

94. Hwang, J.; Lee, S.; Choo, J., Application of a SERS-based Lateral Flow Immunoassay Strip for the Rapid and Sensitive Detection of Staphylococcal Enterotoxin B. *Nanoscale* **2016**, 1-8.

95. (a) Leonardi, G. P.; Wilson, A. M.; Zuretti, A. R., Comparison of Conventional Lateral-flow Assays and a New Fluorescent Immunoassay to Detect Influenza Viruses. *Journal of Virological Methods* **2013,** *189* (2), 379-382; (b) Lee, L. G.; Nordman, E. S.; Johnson, M. D.; Oldham, M. F., A Low-Cost, High-Performance System for Fluorescence Lateral Flow Assays. *Biosensors* **2013,** *3*, 360-373.

96. Mirasoli, M.; Buragina, A.; Dolci, L. S.; Guardigli, M.; Simoni, P.; Montoya, A.; Maiolini, E.; Girotti, S.; Roda, A., Development of a Chemiluminescence-based Quantitative Lateral Flow Immunoassay for On-field Detection of 2,4,6-trinitrotoluene. *Analytica chimica acta* **2012,** *721* (0), 167-172.

97. Fat, E. M. T. K.; Abrams, W. R.; Niedbala, R. S.; Corstjens, P. L. A. M., Lateral Flow Sandwich Assay Utilizing Upconverting Phosphor (UCP) Reporters. *Method Cell Biol* **2012,** *112*, 203-234.

98. Qin, Z.; Chan, W. C. W.; Boulware, D. R.; Akkin, T.; Butler, E. K.; Bischof, J. C., Significantly Improved Analytical Sensitivity of Lateral Flow Immunoassays by Using Thermal Contrast. *Angewandte Chemie International Edition* **2012,** *51* (18), 4358-4361.

99. (a) You, D. J.; Park, T. S.; Yoon, J. Y., Cell-phone-based measurement of TSH using Mie scatter optimized lateral flow assays. *Biosensors and Bioelectronics* **2013,** *40* (1), 180-185; (b) Erickson, D.; O'Dell, D.; Jiang, L.; Oncescu, V.; Gumus, A.; Lee, S.; Mancuso, M.; Mehta, S., Smartphone Technology can be Transformative to the Deployment of Lab-on-Chip Diagnostics. *Lab Chip* **2014,** *14* (17), 3159-3164.

100. (a) Adhikari, M.; Dhamane, S.; Hagström, A. E. V.; Garvey, G.; Chen, W.-H.; Kourentzi, K.; Strych, U.; Willson, R. C., Functionalized Viral Nanoparticles as Ultrasensitive Reporters in Lateral-Flow Assays. *The Analyst* **2013,** *138* (19), 5584-5587; (b) Hagström, A. E. V.; Garvey, G.; Paterson, A. S.; Dhamane, S.; Adhikari, M.; Estes, M. K.; Strych, U.; Kourentzi, K.; Atmar, R. L.; Willson, R. C., Sensitive Detection of Norovirus Using Phage Nanoparticle Reporters in Lateral-Flow Assay. *Plos One* **2015,** *10* (5), e0126571; (c) Kim, J.; Adhikari, M.; Dhamane, S.; Hagström, A. E. V.; Kourentzi, K.; Strych, U.; Willson, R. C.; Conrad, J. C., Detection of Viruses By Counting Single Fluorescent Genetically Biotinylated Reporter Immunophage Using a Lateral Flow Assay. *ACS Applied Materials & Interfaces* **2015,** *7* (4), 2891-2898; (d) Adhikari, M.; Strych, U.; Kim, J.; Goux, H.; Dhamane, S.; Poongavanam, M.-V.; Hagström, A. E. V.; Kourentzi, K.; Conrad, J. C.; Willson, R. C., Aptamer-Phage Reporters for Ultrasensitive Lateral Flow Assays. *Analytical chemistry* **2015,** *87* (23), 11660-11665.

101. (a) Soto, C. M.; Ratna, B. R., Virus Hybrids as Nanomaterials for Biotechnology. *Current opinion in biotechnology* **2010,** *21* (4), 426-38; (b) Yang, S. H.; Chung, W. J.;

McFarland, S.; Lee, S. W., Assembly of bacteriophage into functional materials. *Chem Rec* **2013,** *13* (1), 43-59.

102. Yoo, S. Y.; Chung, W.-J.; Lee, D.-Y., Chemical Modulation of M13 Bacteriophage and its Functional Opportunities for Nanomedicine. *International Journal of Nanomedicine* **2014,** *9* (1), 5825-5836.

103. (a) Douglas, T.; Young, M., Viruses: making friends with old foes. *Science* **2006,** *312* (5775), 873-5; (b) Zhang, H.; Xu, Y.; Huang, Q.; Yi, C.; Xiao, T.; Li, Q., Natural phage nanoparticle-mediated real-time immuno-PCR for ultrasensitive detection of protein marker. *Chemical communications* **2013,** *49* (36), 3778-80; (c) Litvinov, J.; Hagström, A. E. V.; Lopez, Y.; Adhikari, M.; Kourentzi, K.; Strych, U.; Monzon, F. A.; Foster, W.; Cagle, P. T.; Willson, R. C., Ultrasensitive Immuno-Detection using Viral Nanoparticles with Modular Assembly using Genetically-Directed Biotinylation. *Biotechnology Letters* **2014,** *36*, 1863-1868.

104. Kim, H. J.; Rossotti, M. A.; Ahn, K. C.; González-Sapienza, G. G.; Gee, S. J.; Musker, R.; Hammock, B. D., Deveopment of a Noncomptitive Phage Anti-immunocomplex Assay for Brominated Diphenyl Ether 47. *Analytical biochemistry* **2010,** *401* (1), 38-46.

105. Peng, T.; Balijepalli, A.; Gupta, S. K.; LeBrun, T., Algorithms for On-Line Monitoring of Micro Spheres in an Optical Tweezers-Based Assembly Cell. *Journal of Computing and Information Science in Engineering* **2007,** *7*, 330-338.

106. Babaye Khorasani, F.; Poling-Skutvik, R.; Krishnamoorti, R.; Conrad, J. C., Mobility of Nanoparticles in Semidilute Polyelectrolyte Solutions. *Macromolecules* **2014,** *47* (15), 5328-5333.

107. Slattery, J. C., Flow of Viscoelastic Fluids through Porous Media. *AIChE Journal* **1967,** *13* (6), 1066-1071.

108. Washburn, E. W., The Dynamics of Capillary Flow. *Physical Review* **1921,** *17* (3), 273-283.

109. Green, N. M., Avidin. *Advances in Protein Chemistry* **1975,** *29*, 85-133.

110. Knez, K.; Noppe, W.; Geukens, N.; Janssen, K.; Spasic, D.; Heyligen, J.; Vriens, K.; Thevissen, K.; Cammue, B.; Petrenko, V.; Ulens, C.; Deckmyn, H.; Lammertyn, J., Affinity Comparison of p3 and p8 Peptide Displaying Bacteriophages Using Surface Plasmon Resonance. *Analytical chemistry* **2013,** *85* (21), 10075-10082.

111. Weiss, T. H.; Mills, A. L.; Hornberger, G. M.; Herman, J. S., Effect of Bacterial Cell Shape on Transport of Bacteria in Porous Media. *Environmental Science and Technology* **1995,** *29*, 1737-1740.

112. Xu, S.; Liao, Q.; Saiers, J. E., Straining of Nonspherical Colloids in Saturated Porous Media. *Environmental Science and Technology* **2008,** *42*, 771-778.

113. Bao, C.; Conde, J.; Polo, E.; del Pino, P.; Moros, M.; Baptista, P. V.; Grazu, V.; Cui, D.; de la Fuente, J. M., A Promising Road with Challenges: Where are Gold Nanoparticles in Translational Research? *Nanomedicine* **2014,** *9* (15), 2353-2370.

114. Yetisen, A. K.; Akram, M. S.; Lowe, C. R., Paper-based Microfluidic Point-of-Care Diagnostic Devices. *Lab Chip* **2013,** *13* (12), 2210-51.

115. Parolo, C.; Medina-Sanchez, M.; de la Escosura-Muniz, A.; Merkoci, A., Simple Paper Architecture Modifications Lead to Enhanced Sensitivity in Nanoparticle based Lateral Flow Immunoassays. *Lab on a Chip* **2013,** *13* (3), 386-390.

116. Trebbin, M.; Steinhauser, D.; Perlich, J.; Buffet, A.; Roth, S. V.; Zimmermann, W.; Thiele, J.; Forster, S., Anisotropic Particles Align Perpendicular to the Flow Direction in Narrow Microchannels. *Proceedings of the National Academy of Sciences of the United States of America* **2013,** *110* (17), 6706-6711.

117. Choi, J. R.; Hu, J.; Feng, S. S.; Abas, W. A. W.; Pingguan-Murphy, B.; Xu, F., Sensitive Biomolecule Detection in Lateral Flow Assay with A Portable Temperature-Humidity Control Device. *Biosensors & Bioelectronics* **2016,** *79*, 98-107.

118. Tang, R.; Yang, H.; Choi, J. R.; Gong, Y.; Hu, J.; Feng, S.; Pingguan-Murphy, B.; Mei, Q.; Xu, F., Improved Sensitivity of Lateral Flow Assay Using Paper-Based Sample Concentration Technique. *Talanta* **2016,** *152*, 269-276.

119. Paterson, A. S.; Raja, B.; Garvey, G.; Kolhatkar, A.; Hagstroem, A. E. V.; Kourentzi, K.; Lee, T. R.; Willson, R. C., Persistent Luminescence Strontium Aluminate Nanoparticles as Reporters in Lateral Flow Assays. *Analytical Chemistry* **2014,** *86* (19), 9481-9488.

120. Bruno, J. G., Application of DNA Aptamers and Quantum Dots to Lateral Flow Test Strips for Detection of Foodborne Pathogens with Improved Sensitivity versus Colloidal Gold. *Pathogens (Basel, Switzerland)* **2014,** *3* (2), 341-55.

121. Barnett, J. M.; Wraith, P.; Kiely, J.; Persad, R.; Hurley, K.; Hawkins, P.; Luxton, R., An Inexpensive, Fast And Sensitive Quantitative Lateral Flow Magneto-Immunoassay for Total Prostate Specific Antigen. *Biosensors* **2014,** *4* (3), 204-20.

122. Rohrman, B. A.; Leautaud, V.; Molyneux, E.; Richards-Kortum, R. R., A Lateral Flow Assay for Quantitative Detection of Amplified HIV-1 RNA. *Plos One* **2012,** *7* (9).

123. Liu, B. H.; Tsao, Z. J.; Wang, J. J.; Yu, F. Y., Development of A Monoclonal Antibody against Ochratoxin A and its Application in Enzyme-Linked Immunosorbent Assay and Gold Nanoparticle Immunochromatographic Strip. *Analytical Chemistry* **2008,** *80* (18), 7029-7035.

124. Kim, J.; Adhikari, M.; Dhamane, S.; Hagstroem, A. E. V.; Kourentzi, K.; Strych, U.; Willson, R. C.; Conrad, J. C., Detection of Viruses By Counting Single Fluorescent Genetically Biotinylated Reporter Immunophage Using a Lateral Flow Assay. *Acs Applied Materials & Interfaces* **2015,** *7* (4), 2891-2898.

125. Willert, C. E.; Gharib, M., Digital Particle Image Velocimetry. *Experiments in Fluids* **1991,** *10* (4), 181-193.

126. JPIV. http://www.jpiv.vennemann-online.de/ (accessed July 11th 2016).

127. Kalnciema, I.; Balke, I.; Skrastina, D.; Ose, V.; Zeltins, A., Potato Virus M-Like Nanoparticles: Construction and Characterization. *Molecular Biotechnology* **2015,** *57* (11-12), 982-992.

128. Stopar, D.; Spruijt, R. B.; Wolfs, C.; Hemminga, M. A., Protein-lipid Interactions of Bacteriophage M13 Major Coat Protein. *Biochimica Et Biophysica Acta-Biomembranes* **2003,** *1611* (1-2), 5-15.

129. Thiriot, D. S.; Nevzorov, A. A.; Opella, S. J., STRUCTURAL Basis of the Temperature Transition of Pf1 Bacteriophage. *Protein Science* **2005,** *14* (4), 1064-1070.

130. Branston, S. D.; Stanley, E. C.; Ward, J. M.; Keshavarz-Moore, E., Determination of the Survival of Bacteriophage M13 from Chemical and Physical Challenges to Assist in its Sustainable Bioprocessing. *Biotechnology and Bioprocess Engineering* **2013,** *18* (3), 560-566.

131. Gouy, M.; Guindon, S.; Gascuel, O., SeaView Version 4: A Multiplatform Graphical User Interface for Sequence Alignment and Phylogenetic Tree Building. *Molecular Biology and Evolution* **2010,** *27* (2), 221-224.

132. Vieira, J.; Messing, J., Production of Single-Stranded Plasmid Dna. *Methods in Enzymology* **1987,** *153*, 3-11.

133. Higashitani, A.; Greenstein, D.; Horiuchi, K., a Single Amino-acid Substitution Reduces the Superhelicity Requirement of a Replication Initiator Protein. *Nucleic Acids Research* **1992,** *20* (11), 2685-2691.

134. Griffith, J.; Kornberg, A., Mini M13 Bacteriophage - Circular Fragments of M13 Dna are Replicated and Packaged during Normal Infections. *Virology* **1974,** *59* (1), 139-152.

135. Sattarl, S.; Bennettl, N. J.; Wen, W. X.; Guthrie, J. M.; Blackwell, L. F.; Conway, J. F.; Rakonjac, J., ff-nano, Short Functionalized Nanorods Derived From ff (f1, fd, or M13) Filamentous Bacteriophage. *Frontiers in Microbiology* **2015,** *6*.

136. Endemann, H.; Model, P., Location of Filamentous Phage Minor Coat Proteins in Phage and in Infected-cells. *Journal of Molecular Biology* **1995,** *250* (4), 496-506.

137. St-Louis, P., Status of Point-of-Care Testing: Promise, Realities, and Possibilities. *Clinical Biochemistry* **2000,** *33* (6), 427-440.

138. Forbes, J. M.; Cooper, M. E., Mechanisms of Diabetic Complications. *Physiological Reviews* **2013,** *93* (1), 137-188.

139. National diabetes statistics report, 2014. Centers for Disease Control and Prevention website. http://www.cdc.gov/diabetes/data/statistics/2014statisticsreport.html (accessed June 16, 2014).

140. Mook-Kanamori, D. O.; Selim, M. M. E.-D.; Takiddin, A. H.; Al-Homsi, H.; Al-Mahmoud, K. A. S.; Al-Obaidli, A.; Zirie, M. A.; Rowe, J.; Yousri, N. A.; Karoly, E. D.; Kocher, T.; Gherbi, W. S.; Chidiac, O. M.; Mook-Kanamori, M. J.; Kader, S. A.; Al Muftah, W. A.; McKeon, C.; Suhre, K., 1,5-Anhydroglucitol in Saliva is a Noninvasive Marker of Short-term Glycemic Control. *Journal of Clinical Endocrinology & Metabolism* **2014,** *99* (3), E479-E483.

141. Dungan, K. M., 1,5-anhydroglucitol (GlycoMark (TM)) as a Marker of Short-term Glycemic Control and Glycemic Excursions. *Expert Review of Molecular Diagnostics* **2008,** *8* (1), 9-19.

142. Moses, A. C.; Raskin, P.; Khutoryansky, N., Does Serum 1,5-anhydroglucitol Establish a Relationship between Improvements in hba(1c) and Postprandial Glucose Excursions? Supportive Evidence Utilizing the Differential Effects between Biphasic Insulin aspart 30 and Insulin Glargine. *Diabetic Medicine* **2008,** *25* (2), 200-205.

143. Fukumura, Y.; Tajima, S.; Oshitani, S.; Ushijima, Y.; Kobayashi, I.; Hara, F.; Yamamoto, S.; Yabuuchi, M., Fully Enzymatic Method for Determining 1,5-Anhydro-D-Glucitol in Serum. *Clinical Chemistry* **1994,** *40* (11), 2013-2016.

144. Onorato, J. M.; Langish, R. A.; Shipkova, P. A.; Sanders, M.; Wang, J.; Kwagh, J.; Dutta, S., A Novel Method for the Determination of 1,5-Anhydroglucitol, a Glycemic Marker, in Human Urine Utilizing Hydrophilic Interaction Liquid Chromatography/Ms3. *Journal of Chromatography B-Analytical Technologies in the Biomedical and Life Sciences* **2008,** *873* (2), 144-150.

145. Xu, M.; Bunes, B. R.; Zang, L., Paper-Based Vapor Detection of Hydrogen Peroxide: Colorimetric Sensing with Tunable Interface. *Acs Applied Materials & Interfaces* **2011,** *3* (3), 642-647.

146. Evans, S. A. G.; Elliott, J. M.; Andrews, L. M.; Bartlett, P. N.; Doyle, P. J.; Denuault, G., Detection of Hydrogen Peroxide at Mesoporous Platinum Microelectrodes. *Analytical Chemistry* **2002,** *74* (6), 1322-1326.

147. Lu, S.; Song, J.; Campbell-Palmer, L., A Modified Chemiluminescence Method for Hydrogen Peroxide Determination in Apple Fruit Tissues. *Scientia Horticulturae* **2009,** *120* (3), 336-341.

148. Halama, A.; Kulinski, M.; Kader, S. A.; Satheesh, N. J.; Abou-Samra, A. B.; Suhre, K.; Mohammad, R. M., Measurement of 1,5-Anhydroglucitol in Blood and Saliva: from Non-Targeted Metabolomics to Biochemical Assay. *Journal of Translational Medicine* **2016,** *14*.